IOWA STATE UNIVERSITY
Digital Repository

2015

Understanding the reactivity of molecular precursors to colloidal nanocrystals

Samuel Ralph Alvarado
Iowa State University

Follow this and additional works at: https://lib.dr.iastate.edu/etd

Part of the Inorganic Chemistry Commons, and the Nanoscience and Nanotechnology Commons

Understanding the reactivity of molecular precursors to colloidal nanocrystals

by

Samuel R. Alvarado

A dissertation submitted to the graduate faculty

in partial fulfillment of the requirements for the degree of

DOCTOR OF PHILOSOPHY

Major: Inorganic Chemistry

Program of Study Committee:
Javier Vela, Major Professor
James Evans
Gordon Miller
Arthur Winter
Keith Woo

Iowa State University

Ames, Iowa

2015

DEDICATION

To the memory of my distant cousin, Clifford E. Berry, PhD, Iowa State College, 1948 (1918 – 1963). Digital computers were central to the completion of this work. If only he could see how mass spectrometers and computers are interfaced today.

TABLE OF CONTENTS

ACKNOWLEDGMENTS

I could not tell over the multitude of them nor name them,

not if I had ten tongues and ten mouths, not if I had

a voice never to be broken and a heart of bronze within me…

-Homer's *Iliad*, Book II. Translation by Richmond Lattimore.

As Homer listed the ships, the captains, and the multitudes who took part in the Trojan War he called upon the Muses to aid his memory with the hope that no one be left out. So, too, I list those who helped me with science, composition of this thesis, and my education.

My earliest inclinations to attend graduate school occurred while pursuing a chemistry degree at Augustana College in Rock Island, Illinois – a seven mile journey that crossed the Mississippi River in a rusty 1989 Toyota Camry from my home in Davenport, Iowa. While each member of the faculty there had a hand in "getting me into this mess," I credit several of them specifically here: Dave DeWitt, my first inorganic professor who also gave me a very early research opportunity to look at some cobalt ethylenediamine complexes by NMR for inclusion in a teaching lab; Kurt Christoffel's physical chemistry lab course presented my first window into computational chemistry – my finest hour engaged in such activity was spent running a Fortran 77 program that calculated the electronic energy of the He atom, all the while eating a Subway sandwich one spring evening; and Pamela Trotter, who showed me the unusual ways that chemists combine their passions by bringing me as an assistant to her renaissance fair alchemy demos because my long hair "looked the part." Most

culpable of all is Greg Domski, who started as a professor in the summer of 2008. No doubt our first meeting was a startling affair as I accosted this new stranger that very summer in his office while he unpacked his books. As he had the freshest perspective on graduate research at the time, I sought his advice on all things surrounding my next step beyond Augustana. This was also the beginning of my formal research training in synthesis, where I worked on phosphine-functionalized n-heterocyclic carbene binuclear ruthenium complexes.

My education then continued at Iowa State University, where the number of influential people I met increased, as did their impacts on my scientific career. Javier Vela was a one-of-a-kind adviser who gave me the opportunity to supplement this young group's growing body of synthetic work with computational data. I am grateful for him providing opportunities, feedback, and keeping a "scientific roof" over my head. It was under his guidance that I developed a curiosity for all things nanosized and saw that this emerging discipline was a rigorous and interdisciplinary pursuit, valuable not only as a pure science but also for its immediate applications.

All the members of the Vela group also provided an environment of constant fun, support, and cultural enrichment. While the foods that I sampled, the music that I heard, and the discussions that we had exposed small differences, they better illustrated common characteristics held by all humans. I thank them all for the opportunity to learn, even if their customs originated from the far-reaches of Minnesota and Wisconsin.

I also thank my thesis committee for their guidance, input and even hard questions over the years. This group initially consisted of Gordon Miller, Arthur Winter, Keith Woo and Andreja Bakac. Following Andreja Bakac's retirement, Jim Evans officially took her

place, and I thank him for being willing to enter the fray so late in the proceedings. I also apologize to the entire committee for holding my defense at 8 am.

A number of people at Iowa State University provided me with considerable technical guidance in my research. I thank them here, in no particular order: Sarah Cady, who was always willing to help with unusual NMR techniques; Mark Gordon, who started my formal education in computational chemistry; Jakoah Brgoch of the Miller group, who provided much of my informal education in computational and solid state chemistry; Mike Schmidt, who administered the computational cluster at ISU; and Theresa Windus, who lent additional opinions on computational matters and who went above and beyond as my Preparing Future Faculty mentor.

High school and undergraduate researches who assisted me include Jasmin Cisneros, Alex McGarity, Chad Carman, Joseph Stein, and Stephen Todey. Their curiosity, creativity and determination often helped me see chemistry in a different light. I hope they all learned something they can take with them on their journeys beyond ISU, and I wish them all the best wherever they land.

Hua-Jun Fan at Prairie View A&M University was an outstanding collaborator throughout my time at ISU. I learned much from him during his visit in the summer of 2011, when we spent many mornings trying to get computations in VASP and GAMESS to run properly. He was also nearly always available to answer questions from Texas by email or phone.

I also feel the need to acknowledge Anthony Stender, who called me out in his acknowledgments section (yes, I actually read it), so I should return the favor. Over the years since his graduation, we managed to stay in regular contact despite living in different

locations. I benefitted much from his experience and insight into all manner of problems, both chemical and not.

The total support of my family cannot be understated. They have all been at the receiving end of harangues about chemistry, even during my years as an undergraduate, and kindly smiled and nodded at the details that they heard. My parents, especially, held no grudges over my late night arrivals as a commuter from Augustana, fresh from another physical chemistry study session or orchestra rehearsal.

Finally, I thank you, dear reader, for what is an author without an audience? Do not fret if your name does not appear on these pages, for your deeds are beyond the scope of such a technical document, and your names are not meant to be sullied by its content. The muses recount your actions in a different medium that is altogether bigger than ink on paper or packets of electrons in circuits.

ABSTRACT

Colloidal semiconductor nanocrystals are materials with intriguing properties that make them useful for a diverse array of applications such as photocatalysts, light-absorbing materials in solar cells, light emitting diodes and luminescent biological tags, to name only a few. Performance of nanomaterials in these applications is directly related to the size, shape and stoichiometry of the nanocrystals. Strategies exist to control these characteristics during colloidal synthesis, but they tend to rely on certain surfactants, additives, or multi-step procedures to achieve desirable properties. This thesis describes new directions in the synthesis of colloidal nanomaterials that use computational chemistry as a guide. Using new and efficient methods in density functional theory (DFT) to reliably calculate bond dissociation energies (BDEs) of organodichalcogenide (sulfide or selenide) precursors enables the rational synthesis of dot, rod and tetrapod morphology cadmium chalcogenide nanocrystals. Precursors with weaker C-E (E = S, Se) bonds and stronger E-E bonds yielded dot-shaped nanocrystals, while precursors with stronger C-E and weaker E-E bonds afforded rod or tetrapod shapes. This methodology readily extends to the BDE calculation of tertiary phosphine chalcogenides with substituted phenyl, alkyl, perfluoroalkyl moieties or Verkade-type cage structures. In these systems the BDE of a series of P—S or P—Se bonds increases with slightly increasing bond distance, although the BDE of P—Se bonds is significantly lower than P—S bonds.

Another promising method in colloidal nanocrystal synthesis is photochemical decomposition of precursors to access unusual phases or shapes. This thesis also describes

the photochemical synthesis of cobalt(III) oxyhydroxide, Co(O)OH, nanocrystals from chloropentaamminecobalt(III) salts in aqueous solution. Compared to the thermal decomposition of the starting material in the absence of light, the photochemically-synthesized material exhibits a smaller size with a lower-temperature phase transition to cobalt(II,III) oxide, Co_3O_4.

CHAPTER 1

GENERAL INTRODUCTION

Quantum dots are defined as small particles of a semiconducting material between 1-10 nm in size.[1] While the parent bulk materials are semiconductors, the electronic properties of quantum dots are distinct from particle sizes above the nanosize regime. At these larger sizes, the band gap of the semiconductor is independent of particle size. In the solid phase, semiconductor band theory describes the electronic structure as tightly overlapped molecular orbitals creating a continuum of allowed energy levels in the valence band, as well as forbidden energy levels with no electron density. The band gap is then the amount of energy required to promote an electron from the occupied valence band into the conduction band. As particles shrink below the Bohr exciton radius a phenomenon called quantum confinement governs the now size-dependent band gap. As the total number of molecular orbitals is reduced, discrete bands appear in the electronic structure, and the band gap widens. In general, smaller particles of the same stoichiometry exhibit wider band gaps.

The size, shape and composition of quantum dots all play a role in determining their optoelectronic properties.[2] In lieu of an exhaustive list of all possible compositions and shapes, the focus here is on recent efforts to control these properties in II-VI semiconductors, especially in the cadmium chalcogenides. Within this class of materials, dot (spherical), rod and tetrapod morphologies are most common, shown in Figure 1.[3] Colloidal synthesis methods that yield one morphology over another typically require a employing a mixture of surfactants or, especially in the case of tetrapods, use a two-step seeded growth procedure.[4–6] Tuning the particle size requires understanding the conversion kinetics of the precursors, but a remaining challenge is linking the precursor reactivity to the final size.[7] Adjusting the composition of the materials by

alloying two related materials in the same particle (e.g. CdS-CdSe) further tunes the resulting band gap.[8–12]
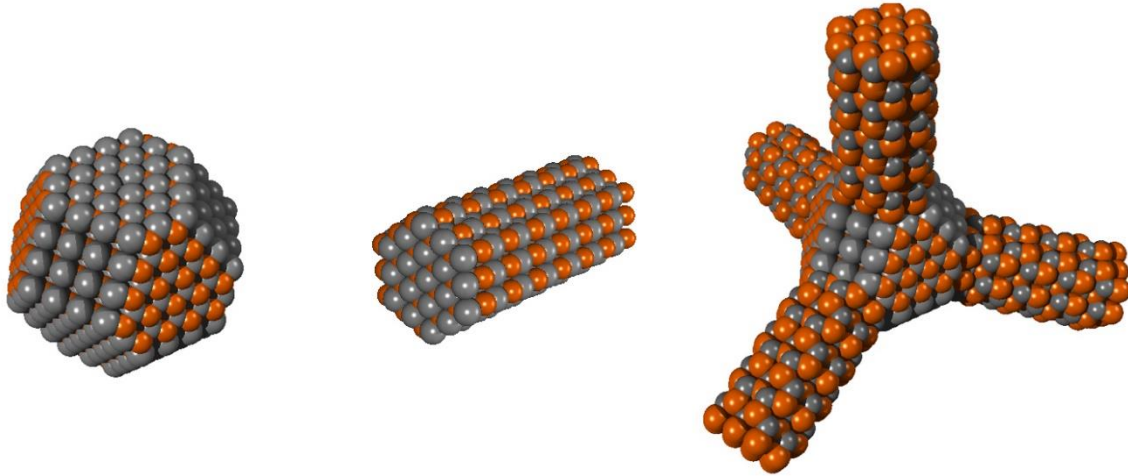
Figure 1. Models of cadmium chalcogenide dot, rod and tetrapod morphology nanocrystals. The dot shape is constructed from zinc blende cadmium sulfide, the rod is wurtzite cadmium sulfide, and the tetrapod shape is a zinc blende core with wurtzite arms.

The effective use of these nanomaterials in practical devices requires precisely tuning the particle size and shape, as these properties change the absorbance and photoluminescence wavelengths. A simple means of adjusting luminescence wavelength, which derives from the quantum confinement description of the electronic structure, is by tuning the size of the particles.[13] At the smallest end of the quantum dot scale, so-called magic size clusters exhibit broad spectrum, white-colored luminescence.[14] Aside from size, particle shape also plays a role in determining luminescence wavelength. This is most interesting in the case of tetrapod-shaped particles, which simultaneous emit light of two colors.[15, 16] Particles with chiral ligands stabilizing the surface can emit circularly polarized light.[17] The bright and tunable luminescence from quantum dots makes them an interesting material for light emitting diodes (LEDs).[18, 19] As of the time of writing, some of the first quantum dot-containing display technologies are being

demonstrated at electronics shows and coming to market, though it remains to be seen if such displays supplant the current LCD mainstream.[20]

Quantum dot-based solar cell performance is also subject to the size and shape of the particles in the absorbing layer.[21–23] The fact that quantum dots are produced and handled in solution makes them attractive for their ease of use in industrial processes. One advance in this direction for solar cells is the development of a quantum dot-infused paint which was applied to device backings.[24]

The self-assembly of nanocrystals into larger arrays with unique properties also depends on particle size and shape – special attention must also be paid to the size dispersion of the nanocrystals.[25] Apart from packed arrangements of spherical particles, assemblies of branched structures are also known.[26, 27] The future of self-assembled materials may come in the form of layers of different nanocrystalline arrays.[28]

Shape-controlled nanomaterials are also gaining notoriety as excellent photocatalysts for organic transformations[29] and water splitting.[30, 31] Such catalysts are often rod-shaped with noble metal particles selectively deposited on the ends. This type of selective deposition and accompanying electron transfer[32] is an inherent advantage to rods compared to other nanocrystal shapes for catalytic applications.

Controlling nanocrystalline morphology – from surfactants to molecular reactivity. Optimizing the performance of devices containing nanomaterials requires the use of particles with specific and well-defined sizes, shapes and compositions. A major challenge in bottom-up nanomaterial synthesis is precisely and predictably controlling these properties. An early example of controlled tetrapod synthesis relied n-octadecylphsphonic acid (ODPA) as a ligand which bound to the arms of the tetrapods during growth.[33] The observation that ODPA stabilized

the wurtzite arms of the tetrapod structures was consistent with previous work that showed ODPA favoring the growth of wurtzite nanorods.[34] Since the initial work on colloidal tetrapod synthesis, numerous additional methods have been reported.[35–37] In all, possible mechanisms that produce branched structures include the aforementioned seeded growth as well as twinning, crystal splitting and oriented attachment.[38]

Photochemical synthesis methods may also allow for the isolation of unusual shapes or metastable phases not found during thermolysis. The synthesis of gold nanoparticles by photolysis is known and can afford rod[39] or spherical morphologies.[40, 41] Such methods are intriguing avenues of research in the synthesis of semiconductor-metal heterostructures.[42, 43] Other materials synthesized in this manner include CeO_2,[44] $BiSe$,[45] $Co(O)OH$,[46] manganese and cobalt oxides,[47] and a variety of main group elements and compounds.[48]

Alternatively, the kinetics of precursor conversion can influence the rate of nucleation and resulting shape of colloidal nanocrystals. Slow precursor conversion is associated with slow nucleation to yield nanorods, while fast precursor conversion leads to fast nucleation and affords quantum dots.[49] When using phosphine chalcogenide precursors to synthesize cadmium chalcogenide nanocrystals, compounds with weak P—E bonds formed nanorods of shorter length than strong P—E bonds.[50] In the synthesis of $CuInSe_2$, organic diselenide precursors produced the metastable wurtzite phase of the material rather than the thermodynamically more stable chalcopyrite phase.[51] Since these observations, investigations of precursor conversion kinetics and mechanistic insight into nanocrystal synthesis have become more numerous as the field matures.[52, 53]

Screening precursors for nanocrystal synthesis. The aforementioned mechanistic work leads to a deeper fundamental question in the field of nanocrystal synthesis: Beyond

retrospectively understanding synthesis mechanisms, is it possible to predict the outcome of a nanocrystal synthesis before carrying it out in the laboratory? It appears that the earliest events in the approximate timeline of nanocrystal synthesis – the conversion of precursors to form reactive monomers and crystal nuclei – have considerable influence on the final outcome. Hammond's postulate[54] would infer that the transition state of the reaction would look more like the molecular precursors than the much larger nanocrystals, whose formation is eventually driven by nucleation theory and lattice enthalpy.[55]

When using organochalcogen molecules to synthesize nanomaterials, essentially all bonds to the sulfur or selenium must be broken to give metal-chalcogen nuclei. A possible way to predict the ease of this event and the rate of nanocrystal nucleation and growth is to consider the bond dissociation energies (BDEs or bond enthalpies) of the molecular precursors. As chemists intuitively understand this concept, it makes a simple starting point for gaining insight into precursor conversion.

Bond dissociation enthalpy (BDE) is defined as the enthalpy change in the process of homolytically breaking a covalent bond, shown in Figure 2. The importance of these values is central to all chemical processes that involve making and breaking bonds, although determining BDEs is not straightforward.[56] Typical experimental measurement methods include calorimetry, spectroscopy, chemical equilibrium, chemical kinetics, and mass spectrometry.[57] Values for bonds in many compounds are tabulated in reference books.[58] If no entry is available for a desired molecule, Benson group additivity methods are a convenient way to estimate a BDE.[59] These methods estimate the enthalpy of formation of a molecule by adding together enthalpies of formation of its constituent functional groups. This strategy has been successful for a wide variety of organic molecules including aliphatic and aromatic hydrocarbons, compounds of

heteroatoms and free radicals.[60] BDEs are tabulated and measured for gas phase molecules – values in solution are different from gas phase due to solvation effects on the reaction.[61]
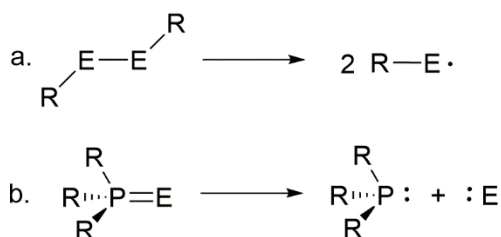
Figure 2. Examples of bond hemolysis reactions in (a) organodichalcogenide and (b) organophosphine chalcogenide.

Experimental measurements have not kept pace with the growing number of described compounds in the literature. Chemists have since begun turning to computational methods to quickly and accurately assess bond strengths. For calculations of thermodynamic properties starting from quantum mechanics, Gaussian-2 and the more modern Gaussian-3 (G2 and G3, respectively) theory are quite possibly the most accurate among all quantum mechanical methods. G2 is a composite method that uses large (6-311G(d,p)) basis sets and treats electron correlation with Moller-Plesset (MP) perturbation theory and quadratic configuration interaction.[62] This high level of theory grants accuracy over other methods, but comes with the penalty of requiring longer computation time and greater computer resources. More commonly applied is density functional theory (DFT), which computes electron density around atoms rather than the wavefunction. Functionals used within this theory contain how the electron density varies with position and how to treat electron exchange and correlation.[63] Compared to the best possible theories, accuracy is somewhat decreased, and the user must choose the appropriate functional for the system under investigation – e.g. some functionals perform better on transition metals than main group compounds.[64] On the other hand, the demand on computational resources is significantly reduced, and chemical systems larger than a handful of atoms become

feasible to study. Functionals fall into general classes depending on their level of theoretical sophistication;[65] some of the simpler and commonly used apply the local density approximation (LDA, based on the exact exchange energy of a uniform electron gas), the generalized gradient approximation (GGA, adds a spin dependence to the gradient) and meta-GGA (adds a dependence on spin kinetic energy density).[66]

These aforementioned weaknesses have not precluded the use of DFT in calculating BDEs. In fact, DFT is broadly applicable to many systems and can predict periodic trends in chemical bonding.[67] It also successfully describes bonding energetics in compounds that are useful as chalcogen sources in nanocrystal synthesis, including disulfides,[68, 69] diselenides[70, 71] and phosphine chalcogenides.[72] An added advantage to performing DFT calculations is that they provide a wealth of information about the molecule in addition to the property of immediate interest, including bond angles, bond distances and electronic structure. Comparing these results with QSAR procedures[73] such as Hammett constants[74] verifies accuracy as well as lends additional insight into how molecular structure influences bond strengths. In all, these data provide a more complete picture of the molecule in question and shows how its constituent functional groups influence its bond strengths and reactivity.

The purpose of this thesis is to explore the molecular chemistry involved in synthesizing nanomaterials. Computationally studying the bond dissociation energies of organic disulfides and diselenides proves to be a reliable method for rationalizing the outcome of the synthesis of cadmium sulfide and cadmium selenide nanoparticles. This same method also predicts the reactivity of phosphine sulfide and selenide molecules, and further shows that bond length is not necessarily correlated with bond strength.[75] The results of this work also have impacts in areas outside of nanomaterial synthesis, such as atom transfer reactions.[76] This thesis also describes the

use of photochemical decomposition of a cobalt coordination complex to produce reliably small cobalt oxyhydroxide nanocrystals. This demonstrates an intriguing alternative method to nanoparticle synthesis and results more generally fit into the fields of photochemical kinetics and coordination chemistry.

Thesis organization

Chapter 2 describes the synthesis, characterization and formation mechanism of spherical cobalt oxyhydroxide (Co(O)OH) nanocrystals. The formation of these nanocrystals proceeds through the aquation of $[Co(NH_3)_5Cl]^{2+}$ to give $[Co(NH_3)_5(H_2O)]^{3+}$ before slow, photoinduced release of NH_3 from the aqua complex. The absorbance spectrum of these particles showed an onset consistent with semiconducting behavior; this was further verified by electronic structure calculation in the Vienna Ab-initio Simulation Package. Cobalt oxyhydroxide exhibits a phase transition to cobalt(II,III) oxide (Co_3O_4) at 251 °C for large size particles. Small particles prepared by photolysis exhibit this shape-conserved phase transition at 206 °C according to thermogravimetric analysis. Other members of the Vela group, Yijun Guo and Purnima Ruberu, carried out the transmission electron microscopy (TEM) characterization.

Chapter 3 discusses computational screening of disulfides and diselenides as precursors for the synthesis of cadmium sulfide or selenide nanocrystals. Based on bond dissociation energies, disulfides with strong C-S and weak S-S bonds produce tetrapod-shaped nanocrystals, while disulfides with weaker C-S bonds produce spherical nanocrystals. Further weakening of precursor C-S bonds leads to particles that grow faster with little shape control. Diphenyl disulfide possesses strong C-S bonds and does not yield any CdS under the experimental conditions; that said, mixing it with other disulfide precursors affords nanocrystals of tetrapod

morphology. This implies that the S-S bond of diphenyl disulfide might break during synthesis and stabilize nanoparticle growth in specific directions. In close collaboration, Yijun Guo, a member of the Vela group, carried out the experimental work for this chapter of the thesis.

Chapter 4 extends the concept of computational screening by calculating bond dissociation energies to tertiary phosphine sulfide and phosphine selenide molecules. Creating molecules with varying degrees of electron density on the P—S or P—Se unit causes significant differences in the bond strength. Furthermore, the length of this bond increases with increasing bond strength, which is counter to the notion that shorter bonds are stronger. We rationalize this by showing that stronger bonds have greater negative charge about the S or Se, which leads to a longer bond with more ionic character. Prof. Hua-Jun Fan and Ian Shortt at Prairie View A&M University in Prairie View, Texas provided vibrational frequency analysis and discussion for this manuscript.

References

[1] Kim, J. Y.; Voznyy, O.; Zhitomirsky, D.; Sargent, E. H. *Adv. Mater.* **2013**, *25*, 4986–5010.

[2] Burda, C.; Chen, X.; Narayanan, R.; El-Sayed, M. A. *Chem. Rev.* **2005**, *105*, 1025–1102.

[3] Kumar, S.; Nann, T. *Small* **2006**, *2*, 316–329.

[4] Manna, L.; Milliron, D. J.; Meisel, A.; Scher, E. C.; Alivisatos, A. P. *Nature Mater.* **2003**, *2*, 382–385.

[5] Talapin, D. V.; Nelson, J. H.; Shevchenko, E. V.; Aloni, S.; Sadtler, B.; Alivisatos, A. P. *Nano Lett.* **2007**, *7*, 2951–2959.

[6] Fiore, A.; Mastria, R.; Lupo, M. G.; Lanzani, G.; Giannini, Carlino, E.; Morello, G.; De Giorgi, M.; Li, Y.; Cingolani, R.; Manna, L. *J. Am. Chem. Soc.* **2009**, *131*, 2274–2282.

[7] Hens, Z.; Čapek, R. K. *Coord. Chem. Rev.* **2014**, *263*, 217–228.

[8] Bailey, R. E.; Nie, S. *J. Am. Chem. Soc.* **2003**, *125*, 7100–7106.

[9] Swafford, L. A.; Weigand, L. A.; Bowers, M. J.; McBride, J. R.; Rapaport, J. L.; Watt, T. L.; Dixit, S. K.; Feldman, L. C.; Rosenthal, S. J. *J. Am. Chem. Soc.* **2006**, *128*, 12299–12306.

[10] Smith, D. K.; Luther, J. M.; Semonin, O. E.; Nozik, A. J.; Beard, M. C. *ACS Nano* **2011**, *5*, 183–190.

[11] Aubert, T.; Cirillo, M.; Flamee, S.; Van Deun, R.; Lange, H.; Thomsen, C.; Hens, Z. *Chem. Mater.* **2013**, *25*, 2388–2390.

[12] Ruberu, T. P. A.; Vela, J. *ACS Nano* **2011**, *5*, 5775–5784.

[13] Yu, W. W.; Qu, L.; Guo, W.; Peng, X. *Chem. Mater.* **2003**, *15*, 2854–2860; **2004**, *16*, 560.

[14] Bowers, M. J. II; McBride, J. R.; Rosenthal, S. J. *J. Am. Chem. Soc.* **2005**, *127*, 15378–15379.

[15] Lutich, A. A.; Mauser, C.; Da Como, E.; Huang, J.; Vaneski, A.; Talapin, D. V.; Rogach, A. L.; Feldmann, J. *Nano Lett.*, **2010**, *10*, 4646–4650.

[16] Choi, C. L.; Li, H.; Olson, A. C. K.; Jain, P. K.; Sivasankar, S.; Alivisatos, A. P. *Nano Lett.*, **2011**, *11*, 2358–2362.

[17] Govan, J. E.; Jan, E.; Qurejeta, A.; Kotov, N. A.; Gun'ko, Y. K. *Chem. Commun.*, **2010**, *46*, 6072–6074.

[18] Anikeeva, P. O.; Halpert, J. E.; Bawendi, M. G.; Bulović, V. *Nano Lett.* **2009**, *9*, 2532–2536.

[19] Shirasaki, Y.; Supran, G. J.; Bawendi, M. G.; Bulović, V. *Nature Photon.* **2013**, *7*, 13–23.

[20] Poor, A. IEEE Spectrum 2014, 51, 26–27.

[21] Martínez-Ferrero, E.; Albero, J.; Palomares, E. *J. Phys. Chem. Lett.* **2010**, *1*, 3039–3045.

[22] Lan, X.; Masala, S.; Sargent, E. H. *Nature Mater.* **2014**, *13*, 233–240.

[23] Kim, M. R.; Ma, D. *J. Phys. Chem. Lett.* **2015**, *6*, 85–99.

[24] Genovese, M. P.; Lightcap, I. V.; Kamat, P. V. *ACS Nano* **2012**, *6*, 865–872.

[25] Zhang, S.-Y.; Regulacio, M. D.; Han, M.-Y. *Chem. Soc. Rev.* **2014**, *43*, 2301–2323.

[26] Arciniegas, M. P.; Kim, M. R.; De Graaf, J.; Brescia, R.; Marras, S.; Miszta, K.; Dijkstra, M.; van Roij, R.; Manna, L. *Nano Lett.* **2014**, *14*, 1056–1063.

[27] Rupich, S. M.; Talapin, D. V. *Nature Mater.* **2011**, *10*, 815–816.

[28] Talapin, D. V. *ACS Nano* **2008**, *2*, 1097–1100.

[29] Ruberu, T. P. A.; Nelson, N. C.; Slowing, I. I.; Vela, J. *J. Phys. Chem. Lett.* **2012**, *3*, 2798–2802.

[30] Chen, X.; Shen, S.; Guo, L., Mao, S. S. *Chem. Rev.* **2010**, *110*, 6503–6570.

[31] Kubacka, A.; Fernández-García, M.; Colón, G. *Chem. Rev.* **2012**, *112*, 1555–1614.

[32] Ha, J. W.; Ruberu, T. P. A.; Han, R.; Dong, B.; Vela, J.; Fang, N. *J. Am. Chem. Soc.* **2014**, *136*, 1398–1408.

[33] Manna, L.; Milliron, D. J.; Meisel, A.; Scher, E. C.; Alivisatos, A. P. *Nature Mater.* **2003**, *2*, 382–385.

[34] Bandaranayake, R. J.; Wen, G. W.; Lin, J. Y.; Jiang,H. X.; Sorensen, C. M. *Appl. Phys. Lett.* **1995**, *67*, 831–833.

[35] Sugunan, A.; Jafri, H. M.; Qin, J.; Blom, T.; Toprak, M. S.; Leifer, K.; Muhammed, M. *J. Mater. Chem.*, **2010**, *20*, 1208–1214.

[36] Zhang, W.; Jin, C.; Yang, Y.; Zhong, X. *Inorg. Chem.* **2012**, *51*, 531–535.

[37] Lim, J.; Bae, W. K.; Park, K. U.; zur Borg, L.; Zentel, R.; Lee, S.; Char, K. *Chem. Mater.* **2013**, *25*, 1443–1449.

[38] Li, H.; Kanaras, A. G.; Manna, L. *Acc. Chem. Res.* **2013**, *46*, 1387–1396.

[39] Kim, F.; Song, J. H.; Yang, P. *J. Am. Chem. Soc.* **2002**, *124*, 14316–14317.

[40] McGilvray, K. L.; Decan, M. R.; Wang, D.; Scaiano, J. C. *J. Am. Chem. Soc.* **2006**, *128*, 15980–15981.

[41] Sakamoto, M.; Fujistuka, M.; Majima, T. *J. Photochem. Photobiol. C* **2009**, *10*, 33–56.

[42] Alemseghed, M. G.; Ruberu, T. P. A.; Vela, J. *Chem. Mater.* **2011**, *23*, 3571–3579.

[43] Dilsaver, P. S.; Reichert, M. D.; Hallmark, B. L.; Thompson, M. J.; Vela, J. *J. Phys. Chem. C* **2014**, *36*, 21226–21234.

[44] Kamada, K.; Horiguchi, K.; Hyodo, T.; Shimizu, Y. *Cryst. Growth Des*. **2011**, *11*, 1202–1207.

[45] Webber, D. H.; Brutchey, R. L. *Inorg. Chem.* **2011**, *50*, 723–725.

[46] Alvarado, S. R.; Guo, Y.; Ruberu, T. P. A.; Bakac, A.; Vela, J. *J. Phys. Chem. C*, **2012**, *116*, 10382–10389.

47 King'ondu, C. K.; Iyer, A.; Njagi, E. C.; Opembe, N.; Genuino, H.; Huang, H.; Ristau, R. A.; Suib, S. L. *J. Am. Chem. Soc.* **2011**, *133*, 4186–4189.

48 Luz, A.; Malek-Luz, A.; Feldmann, C. *Chem. Mater.* **2013**, *25*, 202–209.

49 Wang, F.; Buhro, W. E. *J. Am. Chem. Soc.* **2012**, *134*, 5369–5380.

50 Ruberu, T. P. A.; Albright, H. R.; Callis, B.; Ward, B.; Cisneros, J.; Fan, H.-J.; Vela, J. *ACS Nano* **2012**, *6*, 5348–5359.

51 Norako, M. E.; Greaney, M. J.; Brutchey, R. L. *J. Am. Chem. Soc.* **2012**, *134*, 23–26.

52 Sowers, K. L.; Swartz, B.; Krauss, T. D. *Chem. Mater.* **2013**, *25*, 1351–1362.

53 García-Rodríguez, R.; Hendricks, M. P.; Cossairt, B. M.; Liu, H.; Owen, J. S. *Chem. Mater.* **2013**, *25*, 1233–1249.

54 Hammond, G. S. *J. Am. Chem. Soc.* **1955**, *77*, 334–338.

55 Alvarado, S. R.; Guo, Y.; Ruberu, T. P. A.; Tavasoli, E.; Vela, J. *Coord. Chem. Rev.* **2014**, *263*, 182–196.

56 Blanksby, S. J.; Ellison, G. B. *Acc. Chem. Res.* **2003**, *36*, 255–263.

57 Berkowitz, J.; Ellison, G. B.; Gutman, D. *J. Phys. Chem.* **1994**, *98*, 2744–2756.

58 Luo, Y. R. Comprehensive Handbook of Chemical Bond Energies, CRC Press, Boca Raton, FL, 2007.

59 Benson, S. W.; Buss, J. H. *J. Chem. Phys.* **1958**, *29*, 546–572.

60 Cohen, N.; Benson, S. W. *Chem. Rev.* **1993**, *93*, 2419–2438.

61 Borges dos Santos, R. M.; Costa Cabral, B. J.; Martinho Simões, J. A. *Pure Appl. Chem.* **2007**, *79*, 1369–1382.

62 Curtiss, L. A.; Raghavachari, K.; Redfern, P. C.; Pople, J. A. *J. Chem. Phys.* **1997**, *103*, 1063–1079.

63 Perdew, J. P.; Ruzsinszky, A.; Constantin, L. A.; Sun, J.; Csonka, G. I. *J. Chem. Theory Comput.* **2009**, *5*, 902–908.

64 Schultz, N. E.; Zhao, Y.; Truhlar, D. G. *J. Phys. Chem. A* **2005**, *109*, 11127–11143.

65 Perdew, J. P.; Schmidt, K. *AIP Conf. Proc.* **2001**, *577*, 1–20.

[66] Cramer, C. J.; Truhlar, D. G. *Phys. Chem. Chem. Phys.* **2009**, *11*, 10757–10816.

[67] Ziegler, T. Periodic Trends in Bond Energies: A Density Functional Study. In *Computational Thermochemistry: Prediction and Estimation of Molecular Thermodynamics*; Irikura, K. K.; Frurip, D. J., Eds.; ACS Symposium Series 677; American Chemical Society, Washington, DC, 1998; pp 369–382.

[68] Denk, M. K. *Eur. J. Inorg. Chem.* **2009**, 1358–1368.

[69] Zou, L.-F.; Shen, K.; Fu, Y.; Guo, Q.-X. *J. Phys. Org. Chem.* **2007**, *20*, 754–763.

[70] Gámez, J. A.; Yáñez, M. *J. Chem. Theory Comput.* **2010**, *6*, 3102–3112.

[71] Heverly-Coulson, G. S.; Boyd, R. J. *J. Phys. Chem. A*, **2011**, *115*, 4827–4831.

[72] Sandblom, N.; Ziegler, T.; Chivers, T. *Can. J. Chem.* **1996**, *74*, 2363–2371.

[73] Karelson, M.; Lobanov, V. S.; Katritzky, A. R. *Chem. Rev.* **1996**, *96*, 1027–1043.

[74] Hansch, C.; Leo, A.; Taft, R. W. *Chem. Rev.* **1991**, *91*, 165–195.

[75] Kaupp, M.; Metz, B.; Stoll, H. *Angew. Chem. Int. Ed.* **2000**, *39*, 4607–4609.

[76] Donahue, J. P. *Chem. Rev.* **2006**, *106*, 4747–4783.

CHAPTER 2

PHOTOCHEMICAL VS. THERMAL SYNTHESIS OF COBALT OXYHYDROXIDE NANOCRYSTALS

Samuel R. Alvarado, Yijun Guo, T. Purnima A. Ruberu, Andreja Bakac, Javier Vela

Abstract

Photochemical methods facilitate the generation, isolation and study of metastable nanomaterials having unusual size, composition, and morphology. These harder-to-isolate and highly reactive phases, inaccessible using conventional high-temperature pyrolysis, are likely to possess enhanced and unprecedented chemical, electro-magnetic and catalytic properties. We report a fast, low temperature and scalable photochemical route to synthesize very small (~3 nm) monodisperse cobalt oxyhydroxide (Co(O)OH) nanocrystals. This method uses readily and commercially available pentaamminechlorocobalt(III) chloride, $[Co(NH_3)_5Cl]Cl_2$ under acidic or neutral pH and proceeds under either near-UV (350 nm) or Vis (575 nm) illumination. Control experiments showed that the reaction proceeds at competent rates only in the presence of light, does not involve a free radical mechanism, is insensitive to O_2, and proceeds in two steps: (1) Aquation of $[Co(NH_3)_5Cl]^{2+}$ to yield $[Co(NH_3)_5(H_2O)]^{2+}$, followed by (2) slow photoinduced release of NH_3 from the aqua complex. This reaction is slow enough for Co(O)OH to form, but fast enough so that nanocrystals are small (ca. 3 nm). The alternative dark thermal reaction proceeds much more slowly and produces much larger (~250 nm) polydisperse Co(O)OH aggregates. UV-Vis absorption measurements and ab-initio calculations yield a Co(O)OH band

gap of 1.7 eV. Fast thermal annealing of Co(O)OH nanocrystals leads to Co_3O_4 nanocrystals with overall retention of nanoparticle size and morphology. Thermogravimetric analysis shows that the oxyhydride to mixed-oxide phase transition occurs at significantly lower temperatures (up to $\Delta T = 64°$ C) for small nanocrystals compared to bulk.

Introduction

Nanotechnology is rapidly evolving toward the fabrication of ever more complex hetero-structured nanomaterials with precise morphology, composition and properties.[1-3] Traditional nanomaterial syntheses rely heavily on thermal decomposition or "pyrolysis" of precursors in high-boiling solvents at high temperature, often in excess of 250-300°C. Under such conditions, isolating highly reactive and/or unstable nanocrystal phases can be challenging. An example is doped nanocrystals, where the dopants or chemical "defects" sit within just a few lattice parameters from the nanocrystal surface and get easily thermally extruded, diffusing away in favor of a more stable homogeneous lattice under typical synthesis temperatures.[4,5] These limitations severely narrow the range of metastable nanocrystalline phases that can be built through traditional high temperature pyrolysis. This problem is of particular timeliness and relevance because it is harder-to-isolate the more reactive metastable phases that are most likely to possess enhanced magnetic, chemical and catalytic properties, and perhaps also unprecedented optoelectronic properties.

Photochemistry is regularly employed by molecular chemists to generate highly reactive species. Similarly, light may be an ideal tool for building metastable nanomaterials.[6] Light-induced reactions usually proceed through alternate pathways at low temperature. Chalcogenide-based nanomaterials such as bismuth selenide nanocrystals[7] and tellurium nanorods,[8] which

previously could not be prepared thermally (by simple heating), were recently prepared photochemically. Surface-bound platinum and palladium nanoparticles were selectively photo-deposited along site-specific segments of axially graded semiconductor nanorods by carefully selecting the irradiation wavelength.[9,10] Soluble gold nanoparticles[11] and gold nanorods,[12] and oxides such as ceria nanocrystals,[13] were also prepared with the aid of light.

Cobalt oxyhydroxide (Co(O)OH), also referred to by its mineral name of "heterogenite", is an example of a metastable phase that can be difficult to isolate at the nanoscale using conventional preparative methods. Co(O)OH is an active component in gas (CO) sensing and detection, oxygen evolution catalysts, and alkaline (Li) batteries.[14] Isolating Co(O)OH requires stabilizing Co(III) against Co(II) under basic conditions while preventing formation of Co_3O_4, a common byproduct,[15-17] or precipitation of cobalt hydroxides.[18,19] Typical preparations involve treating $Co(OH)_2$ or other Co(II) source with an oxidant such as hydrogen peroxide (H_2O_2) or sodium hypochlorite (NaClO) at pH~14.[20-23] These thermal reactions are usually slow, taking up to 18 h at 45 °C or 6 h at 120 °C.[14,20] They tend to produce large ca. 500nm aggregates of clustered 20nm×20nm hexagonal nanocrystals, although certain conditions yield isolated 120nm×120nm hexagonal nanocrystals.[14,20] Chelate(EDTA)- and sonication-assisted syntheses produce even larger Co(O)OH aggregates.[23,24] To control particle size, spatially constrained or "caged" syntheses have been performed using Ferritin as a template.[25-27]

Here, we describe a room temperature (RT) photochemical synthesis of small ca. 3 nm Co(O)OH colloidal nanocrystals in as little as 2-4 hours under either ultraviolet (UV) or visible (Vis) light irradiation. This method uses readily available precursors such as pentaamminechlorocobalt(III) chloride, $[Co(NH_3)_5Cl]Cl_2$, and whole-flask illumination with widely available fluorescent lamps. In contrast, we show that similar thermal reactions, run by

heating the sample to 80°C overnight, lead to larger 100-300 nm Co(O)OH aggregates. We present complete optical, structural, and computational characterization and modeling for Co(O)OH, and use the photochemically and thermally produced nanocrystals as precursors for the synthesis of differently-sized Co_3O_4 nanocrystals via thermal annealing.

Experimental

Materials. Cobalt(II) nitrate hexahydrate ($Co(NO_3)_2 \cdot 6H_2O$, 99.999%), pentaamminechlorocobalt(III) chloride ($[Co(NH_3)_5Cl]Cl_2$, 98%), concentrated ammonium hydroxide (NH_4OH, ACS Reagent), and (2,2,6,6-tetramethylpiperidin-1-yl)oxyl (TEMPO, 98%) were purchased from Aldrich. Hexaamminecobalt(III) chloride ($[Co(NH_3)_6]Cl_3$, 99.999%) was purchased from Strem. Sodium bicarbonate ($NaHCO_3$, ACS), concentrated nitric acid (HNO_3, ACSPlus), concentrated hydrochloric acid (HCl, ACSPlus) and hydrogen peroxide (H_2O_2, 30%) were purchased from Fisher. Pentaamminechlorocobalt(III) perchlorate, $[Co(NH_3)Cl](ClO_4)_2$ was synthesized as reported previously.[28] All chemicals were used as received unless specified otherwise.

Synthesis. *Co(O)OH nanocrystals. Photochemical Synthesis.* Pentaamminechlorocobalt(III) perchlorate, $[Co(NH_3)Cl](ClO_4)_2$ (30.8 mg, 81.4 μmol) or pentaamminechlorocobalt(III) chloride, $[Co(NH_3)_5Cl]Cl_2$ (41.5 mg, 166 μmol) was dissolved in 15 mL of either deionized water or 0.01 M aqueous HCl. The solution was placed inside a Rayonet photoreactor and irradiated at 350 nm for 2 h or at 575 nm for 7 h. [9] A dark brown colloidal suspension with a pH of ca. 8-9 formed. Photochemically-produced Co(O)OH nanocrystals were separated by centrifugation (4000 rpm × 5 min), and were re-suspended in methanol.

Thermal synthesis. In the dark, $[Co(NH_3)_5Cl]Cl_2$ (837 mg, 332 µmol) was dissolved in 30 mL deionized water in a resealable Schlenk bomb, wrapped in aluminum foil, and heated in a pre-equilibrated oil bath to 80 °C for 24 h. The reaction mixture was cooled to R.T. and thermally-produced Co(O)OH nanocrystals separated by centrifugation (4000 rpm × 5 min).

Co_3O_4 nanocrystals. Dry Co(O)OH nanocrystals prepared either photochemically or thermally (420 mg, 4.57 mmol) were weighed in a scintillation vial and heated for 30 min in a muffle furnace at 250 °C or 280 °C, respectively.

Control Experiments. *Thermal controls*. In the dark, $[Co(NH_3)_5Cl]Cl_2$ (84.9 mg, 339 µmol) was dissolved in 30 mL of either deionized water or 0.01 M aqueous HCl in a resealable Schlenk bomb, wrapped in aluminum foil, and either kept at RT or heated in a pre-equilibrated oil bath to 80° C. Reaction progress was monitored by UV-Vis for 24-96 h.

Precursor screening. Hexaaquacobalt(II). Cobalt(II) nitrate hexahydrate, $Co(NO_3)_2 \cdot 6H_2O$ (47.1 mg, 162 µmol) was dissolved in 14 mL deionized water, and 0.1 M ammonia was added dropwise until pH = 7.4.[29] This pink solution, containing $[Co(H_2O)_6]^{2+}$ ions, was irradiated at 350 nm for 2 h.

Hexaaquacobalt(III). A solution of sodium bicarbonate (3.41 g, 40.6 mmol), 30% hydrogen peroxide, H_2O_2 (0.1 mL), and deionized water (10 mL) was added slowly to a solution of $Co(NO_3)_2 \cdot 6H_2O$ (0.5561 g, 1.910 mmol), 30% H_2O_2 (0.1 mL) and deionized water (10 mL). The resulting deep green solution was added slowly to 4 M HNO_3 (80 mL) to yield a deep blue solution containing $[Co(H_2O)_6]^{3+}$ ions.[29] The solution was irradiated at 350 nm for 1 h, giving a light pink solution characteristic of hexaaquacobalt(II), $[Co(H_2O)_6]^{2+}$ ions.

Hexaamminecobalt(III). Hexaamminecobalt(III) chloride, $[Co(NH_3)_6]Cl_3$ (395.1 mg, 1.477 mmol) was dissolved in 150 mL deionized water. This solution was irradiated at 350 nm

for 18 h. The reaction mixture was centrifuged (4000 rpm × 5 min) to give dark brown Co(O)OH powder.

Anaerobic synthesis: Probing the effect of O₂. [Co(NH₃)₅Cl]Cl₂ (40.1 mg, 1.60 mmol) was dissolved in 15 mL deionized water. The solution was sparged with Ar for 15 min, sealed, and evacuated under dynamic vacuum for 3 min, then refilled with Ar and the process repeated 3 times. This solution was irradiated at 350 nm for 2 h.

Radical trap effect. [Co(NH₃)₅Cl]Cl₂ (39.3 mg, 1.57 mmol) was dissolved in 15 mL deionized water. 2,2,6,6-tetramethylpiperidine 1-oxyl, TEMPO (55.3 mg, 3.54 mmol) was then added. The homogeneous solution was irradiated at 350 nm for 2 h. The reaction mixture was centrifuged (4000 rpm × 5 min) to give dark brown Co(O)OH powder and an orange supernatant (soluble TEMPO).

Photolysis and Characterization. Photolyses utilized either a fan-cooled Rayonet® photoreactor with 16 side-on 350 nm lamps (35 nm fwhm, intensity = 136 W/m²)[9] or 575 nm lamps (75 nm fwhm, intensity = 47.2 W/m²).

Absorption spectroscopy. Ultraviolet-Visible-Near-Infrared (UV-Vis-NIR) absorption spectra were recorded with a photodiode array Agilent 8453 spectrophotometer. Solvent absorption was subtracted from all spectra. We estimated the absorption coefficient of ca. 3 nm Co(O)OH nanocrystals to be $\varepsilon = 8.0 \times 10^4 \ M^{-1} \cdot cm^{-1}$ at 680 nm (1.82 eV) and $\varepsilon = 1.6 \times 10^6 \ M^{-1} \cdot cm^{-1}$ at 360 nm (3.44 eV).

X-Ray diffraction. Powder X-ray diffraction (XRD) data were measured using a Scintag XDS-2000 diffractometer equipped with a theta-theta goniometer, a sealed-tube solid-state generator providing Cu-Kα radiation, and an air-cooled Kevex Psi Peltier silicon detector.

Transition Electron Microscopy (TEM). TEM was conducted on carbon-coated copper

grids using a FEI Technai G2 F20 Field Emission scanning transition electron microscope (STEM) at 200 kV. Elemental composition was characterized by energy dispersive spectroscopy (EDS) in STEM mode.

Thermo-Gravimetric Analysis (TGA). TGA was conducted on a TA Instruments 2950 TGA at ISU's Materials Analysis Research Laboratory. The sample was heated in N_2 at 20 °C/min to 520 °C at a resolution of 5.0 °C.

Computational details. Computations were completed on the CRUNCH system supported by the Computation Advisory Committee of Iowa State University. Band gaps were determined by calculating the density of states diagram and band structure using the Vienna Ab-initio Simulation Package (VASP). Projector-augmented wave (PAW) pseudopotentials[30] and the Perdew-Burke-Ernzerhoff (PBE) generalized gradient approximation (GGA)[31] were used. A Monkhorst-Pack *k*-points grid of 12×12×4 was used to sample the first Brillouin zone for reciprocal space integration. We utilized the GGA+U method to better describe the experimentally observed band gap. We determined a value of U = 3.2 eV gave the best agreement with experiment.

Results and discussion

Photochemical decomposition of [Co(NH₃)₅Cl]X₂ (X = Cl, ClO₄). As part of our studies of energy transfer between photoactive nanocrystals and transition metal complexes, we observed that irradiating aqueous solutions containing pentaamminechlorocobalt(III) ions with 350 nm light at 21-24 °C (RT) and pH 2 (acidified with 0.01 M HCl or $HClO_4$) for 3 h results in formation of cobalt oxyhydroxide (Co(O)OH) nanocrystals.

Pentaamminechlorocobalt(III), $[Co(NH_3)_5Cl]^{2+}$ is a purple-colored water-soluble complex ion characterized by two absorption maxima (λ_{max}) at 355 nm and 525 nm (Figure 1). After 350 nm irradiation for 35 min, aqueous solutions of $[Co(NH_3)_5Cl]^{2+}$ become brown, with two new, very intense bands appearing at 360 nm (λ_{max}) and 650 nm (shoulder). After 350 nm irradiation for 70 min, the initial absorption peaks from $[Co(NH_3)_5Cl]^{2+}$ are no longer visible. Centrifugation of this solution results in separation of a brown powder that can be re-suspended in methanol. The pH of the supernatant is 8.8. We later observed that the brown powder, which consists of nanocrystalline Co(O)OH (see below), also forms when 575 nm light is used, and even when the reaction is run in the absence of acid, in which case the initial solution pH is 6.5 while the supernatant pH is 8.8.
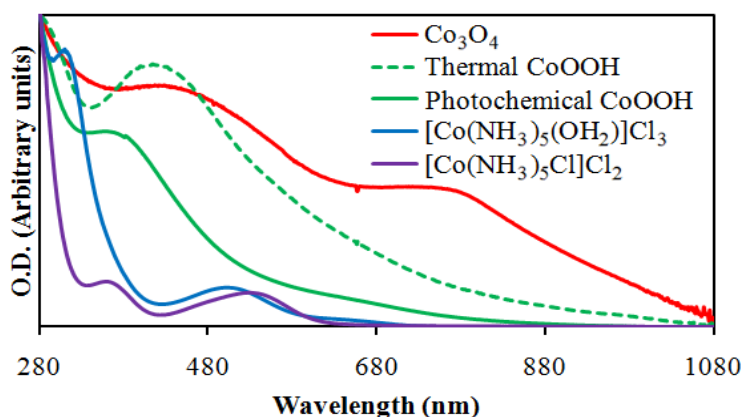

Figure 1. UV-Vis absorption spectra of thermal and photochemical Co(O)OH in methanol, and of $[Co(NH_3)_5Cl]Cl_2$, $[Co(NH_3)_5(OH_2)]Cl_3$ and Co_3O_4 in water.

Powder X-ray diffraction (XRD) shows that the brown precipitate consists of crystalline cobalt oxyhydroxide, Co(O)OH (Figure 2). Cobalt oxyhydroxide crystallizes in a hexagonal unit cell with lattice parameters a = 2.855 Å and c = 8.805 Å. The structure consists of anionic $[Co(O)O]^-$ layers of Co^{3+} ions,[32,33] each octahedrally-coordinated by triply bridging oxide ligands (μ^3-O^{2-}); $[Co(O)O]^-$ layers are held together by hydrogen bonds, with each H^+ ion bridging together two oxides from adjacent layers (Figure 3). Transmission electron microscopy (TEM)

shows that photochemically-produced Co(O)OH consists of relatively monodisperse, small 3.3 nm ± 0.9 nm nanocrystals (Table 1, Figure 4). This morphology agrees well with the crystalline domain (grain size) of ca. 3.2 nm obtained from XRD peak widths (Table 1).[34] High-resolution (HR) TEM shows lattice fringes in all nanocrystals, and selected area diffraction (SAD) patterns show d-spacings of 0.45 nm (003), 0.24 nm, 0.22 nm (102) and 0.21 nm (006), each of which is in close agreement with the d-spacings observed in the powder XRD pattern (Figure 1). Energy dispersive X-ray diffraction (EDS) area scans confirm the presence of both cobalt and oxygen.
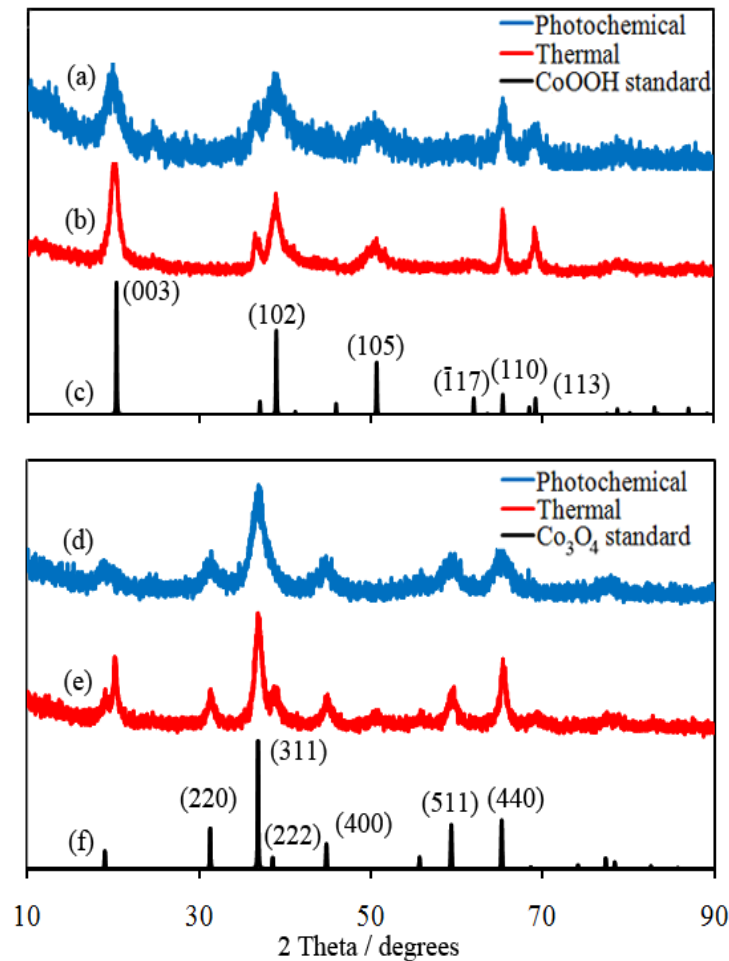
Figure 2. XRD data for: Photochemically prepared Co(O)OH (a), thermally prepared Co(O)OH (b), bulk Co(O)OH (c), Co_3O_4 made by thermal annealing of photochemically-prepared Co(O)OH (d), Co_3O_4 made by thermal annealing of thermally-prepared Co(O)OH (e), and bulk Co_3O_4 (f).
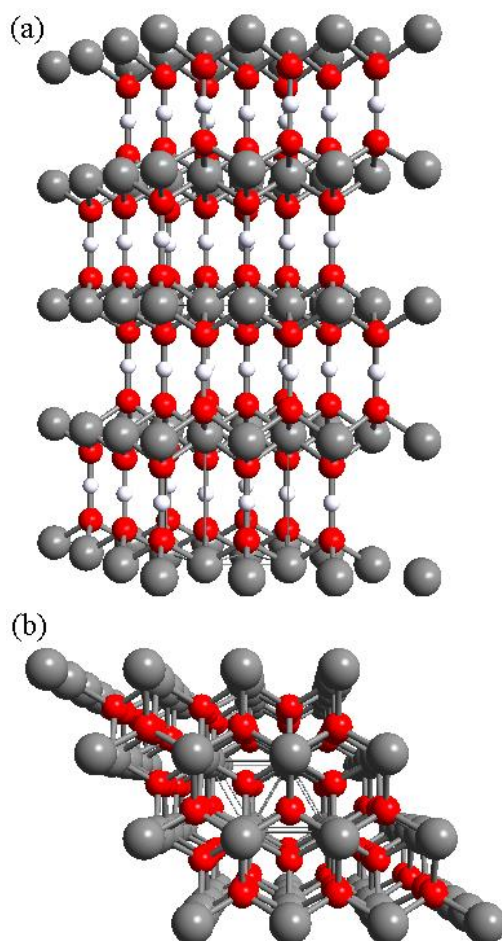
**Figure 3.** Crystalline structure of Co(O)OH viewed down the y-axis (a) and z-axis (b). (Gray = Co; Red = O; White = H).

Thermal decomposition of $[Co(NH_3)_5Cl]X_2$ (X = Cl, ClO_4). To probe the role of light in the formation of cobalt oxyhydroxide, we carried out several thermal syntheses and mechanistic control experiments (see below). Aqueous solutions containing pentaamminechlorocobalt(III), $[Co(NH_3)_5Cl]^{2+}$, kept in the dark at 21-24 °C (RT), show no appreciable particle formation for over 4 days (>96 h). Similarly, heating aqueous solutions containing $[Co(NH_3)_5Cl]^{2+}$ to 80 °C at pH 2 (acidified with HCl) in the dark for 24 h does not form cobalt oxyhydroxide, Co(O)OH, but likely the aquation product, pentaammineaquacobalt(III), $[Co(NH_3)_5(OH_2)]^{3+}$. UV-Vis spectra show a blue-shift of λ_{max} values from 355 nm and 525 nm to 305 nm and 509 nm, respectively (Figure 1, see below). However, heating aqueous solutions containing

pentaamminechlorocobalt(III), $[Co(NH_3)_5Cl]^{2+}$ ions at 80 °C and pH 6.5 (near-neutral pH without acid or base added) in the dark for 24 h results in formation of brown-colored Co(O)OH, as determined from XRD (Figure 2). The UV-Vis absorption spectrum of this thermally prepared Co(O)OH shows two intense bands at 410 nm (λ_{max}) and 710 nm (shoulder), which are red-shifted compared to the photochemically prepared Co(O)OH (Figure 1). After separation of the brown precipitate by centrifugation, the colorless supernatant has a pH of 9.1 and is completely transparent in the 300-1100 nm spectral region. However, in contrast to the small and highly crystalline nature of the photochemically-produced Co(O)OH, TEM micrographs show the thermally-prepared Co(O)OH consists of large aggregates of 70 nm × 10 nm crystalline rods embedded within larger ca. 250 nm amorphous flake-like regions (Table 1, Figure 5).[14] The crystalline domain (grain size) obtained from XRD peak widths is ca. 17nm (Table 1).[34] High-resolution (HR) TEM micrographs show lattice fringes only on the rod-like structures (Figure 5).

Table 1. Synthesis of Co(O)OH and Co_3O_4 nanocrystals under different conditions.

#	Precursor	Conditions	Product	TEM Particle Size/nm	XRD Particle Size/nm
1	$[Co(NH_3)_5Cl]X_2$ (X = Cl, ClO$_4$)	Photochemical (350nm or 575nm), 2<pH<6.5 (aqueous)[a]	Co(O)OH (1.9 eV)[c]	3.3 ± 0.9	3.2
2	$[Co(NH_3)_5Cl]X_2$ (X = Cl, ClO$_4$)	Thermal (80 °C), in the dark, pH=6.5 (aqueous)[a]	Co(O)OH (1.7 eV)[c]	ca. 250 (aggregates)	17
3	Co(O)OH (Photo 3.3 nm)	Annealing at 250 °C, 30 min (dry)	Co_3O_4	5.0±1.0	3.8
4	Co(O)OH (Thermal 250 nm)	Annealing at 280 °C, 40 min (dry)	Co_3O_4	ca. 125 (aggregates)	39

[a]$[Co]_{total}$ = 0.01 M. [b]Calculated from XRD peak widths using Scherrer equation. [c]Observed absorption onset.
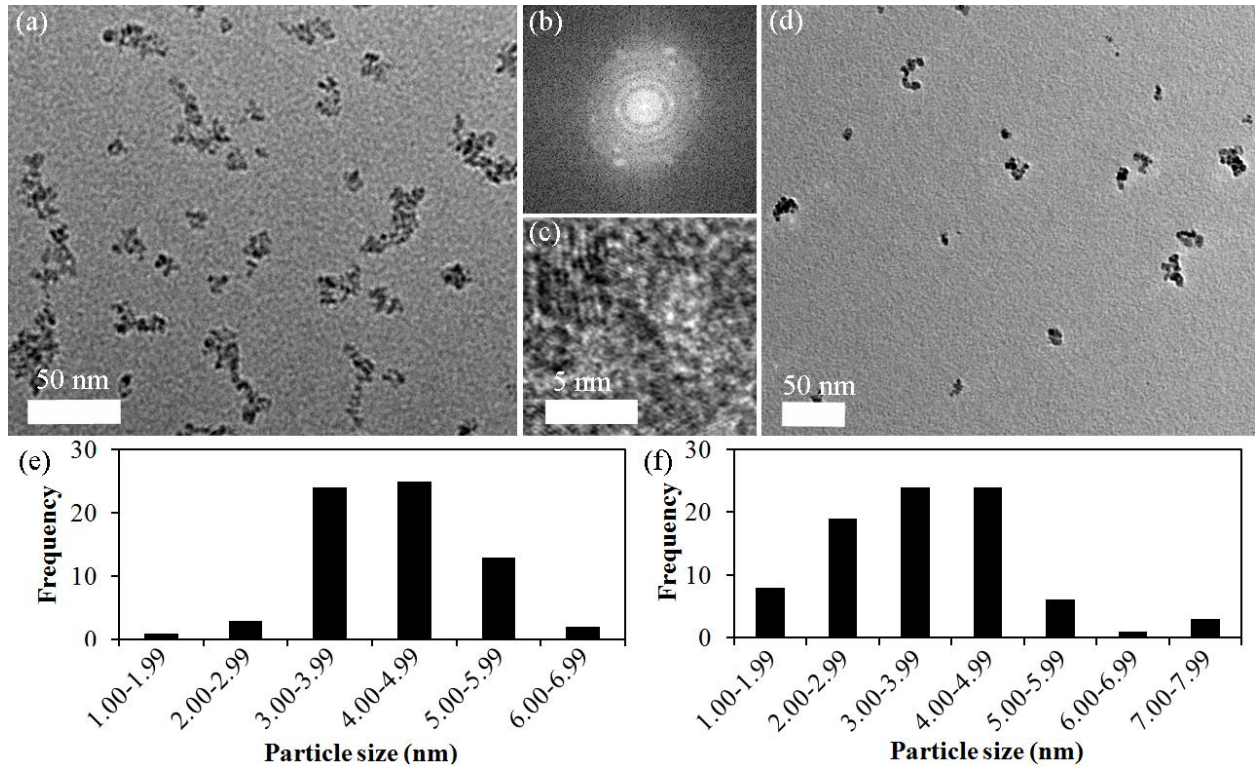
Figure 4. Representative TEM (a), selected area diffraction (SAD) (b), and high-resolution (HR) TEM (c) of photochemically-prepared Co(O)OH nanocrystals. Representative TEM (d) of Co_3O_4 prepared by thermal-annealing of photochemically-prepared Co(O)OH. Particle size histograms of photochemically-prepared Co(O)OH (e), and Co_3O_4 prepared by thermal-annealing of photochemically-prepared Co(O)OH (f).
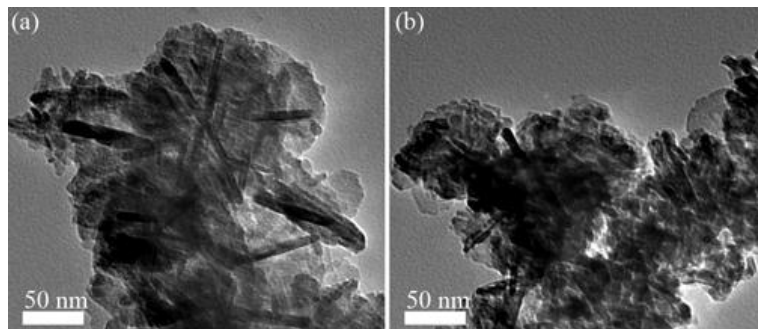
Figure 5. TEM of thermally-prepared Co(O)OH nanocrystals (approximate size of the rod-like structures is 70 nm × 10 nm) (a), and Co_3O_4 nanocrystals prepared by thermal-annealing of thermally-prepared Co(O)OH (approximate size of rod-like structures is 30 nm × 3 nm) (b).

Mechanistic and control experiments. To gain a better understanding on the formation mechanism of Co(O)OH nanocrystals, we subjected several starting materials to different reaction conditions. Because cobalt oxyhydroxide (Co(O)OH) features Co^{3+} ions in an all-oxygen coordination environment, we considered the possibility that its formation could involve

a cobalt-hexaaqua, $[Co(OH_2)_6]^{n+}$, complex intermediate. We irradiated hexaaquacobalt(III), $[Co(OH_2)_6]^{3+}$ solutions at 350 nm under acidic pH (1<pH<2). Irradiation of the deep blue $[Co(OH_2)_6]^{3+}$, with λ_{max} at 400 nm and 605 nm, leads in 1 h to formation of the light pink hexaaquacobalt(II), $[Co(OH_2)_6]^{2+}$, with λ_{max} at 510 nm,[28,35,36] but no Co(O)OH (entry 1 in Table 2, Figure 6). Repeating this experiment at higher pH results in spontaneous, thermal generation of $[Co(OH_2)_6]^{2+}$. This is consistent with the known reactivity of Co^{n+} ions in aqueous solutions: The Pourbaix speciation diagram for aqueous cobalt clearly shows that Co(III) is stable only within a very narrow pH and E region characterized by very acidic and oxidizing conditions.[37,38] In turn, irradiation of $[Co(OH_2)_6]^{2+}$ with 350 nm light for 2 h in near-neutral solution (pH = 6.5) leads to no appreciable formation of Co(O)OH (entry 2 in Table 2, Figure 6). This implies that neither hexaaquacobalt(III) nor hexaaquacobalt(II) are competent intermediates in forming Co(O)OH.

Table 2. Screening of potential intermediates during photochemical Co(O)OH nanocrystal synthesis.[a]

#	Screened Co precursor	pH	Observed Co product
1	$[Co(OH_2)_6]^{3+}$ (aq)	1	$[Co(OH_2)_6]^{2+}$ (aq)
2	$[Co(OH_2)_6]^{2+}$ (aq)	6.5	(no reaction)
3	$[Co(NH_3)_6]^{3+}$ (aq)	2 to 6.5	Co(O)OH (slow, 18 h)
4	$[Co(NH_3)_5Cl]^{2+}$ (aq)	2 to 6.5	$[Co(NH_3)_5(OH_2)]^{3+}$ (aq)
5	$[Co(NH_3)_5(OH_2)]^{3+}$ (aq)	2 to 6.5	Co(O)OH (fast, 3h)

[a]$[Co]_{total}$ = 0.01 M, R.T., 350 nm irradiation.

Given the relative instability of Co(III) in aqueous solutions in the absence of strong field ligands, we then considered the possibility that a redox process could be involved during the formation of cobalt oxyhydroxide (Co(O)OH). Specifically, we tested whether molecular

oxygen, O_2, from air[21,22] was necessary as an oxidant by repeating the photochemical synthesis of Co(O)OH in degassed water solvent starting with pentaamminechlorocobalt(III) chloride, $[Co(NH_3)_5Cl]Cl_2$. Upon irradiation, the UV-Vis absorption spectrum unambiguously showed the formation of Co(O)OH particles under such anaerobic conditions, just as in the original aerobic experiments. Therefore, O_2 is not necessary for the reaction to proceed. We also probed whether the reaction involved free radical species by repeating the photochemical synthesis of Co(O)OH starting with $[Co(NH_3)_5Cl]Cl_2$, in the presence of TEMPO as a radical trapping agent. After 2 h, a brown precipitate formed, and the final supernatant's pH was 8.6. UV-Vis confirmed presence of Co(O)OH in the reaction mixture. Therefore, the reaction does not appear to proceed through a free radical mechanism. To test if a reactive Co-Cl bond is necessary for nanocrystal formation,[39-41] we irradiated solutions of hexaamminecobalt(III), $[Co(NH_3)_6]^{3+}$. This leads to formation of cobalt oxyhydroxide, however at a much slower rate, requiring ca. 18 h to produce significant amounts of Co(O)OH precipitate after centrifugation (entry 3 in Table 2, Figure 6). Therefore, a labile Co-halide(Cl) bond in the $[Co(NH_3)_5Cl]^{2+}$ precursor is important for fast Co(O)OH formation. Photochemical aquation of $[Co(NH_3)_5Cl]^{2+}$ is well known to yield $[Co(NH_3)_5(H_2O)]^{3+}$,[28,35,36] which appears to be the actual active species. As shown in entries 4-5 in Table 2, the irradiation of freshly generated $[Co(NH_3)_5(H_2O)]^{3+}$ yields Co(O)OH rapidly. All of the data suggest that the size of the nanocrystals is determined by the rate of photoinduced release of NH_3 from $[Co(NH_3)_5(H_2O)]^{3+}$. The rate is low enough for Co(O)OH to form, but high enough so that nanocrystals are small (ca. 3 nm) and do not aggregate as they do in the slower thermal reaction. Interestingly, a recent paper reported the photochemical preparation of porous nanocrystals of different metal oxides and Co(O)OH under UV-illumination. Co(O)OH nanoflowers were made from cobalt(II) sulfate heptahydrate ($CoSO_4 \cdot 7H_2O$) and potassium

persulfate ($K_2S_2O_8$) in water.[43] However, the reported particle sizes were much larger, attesting to the importance of using $[Co(NH_3)_5Cl]^{2+}$ salts as precursors to obtain small Co(O)OH nanocrystals.
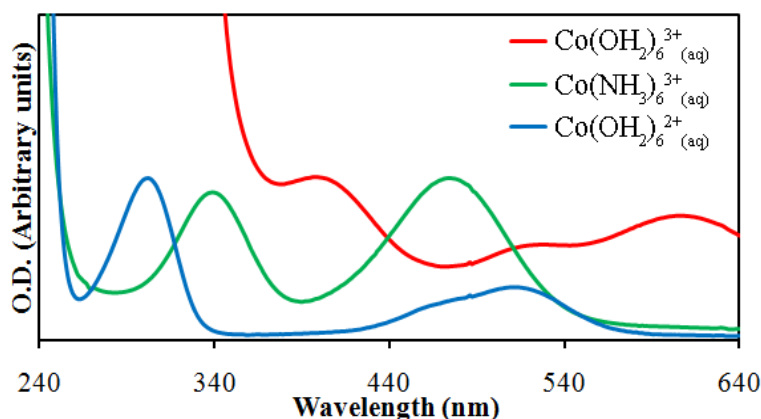
Figure 6. UV-Vis spectra of aqueous $[Co(H_2O)_6](NO_3)_3$ under acidic pH (1-2), and aqueous $[Co(NH_3)_6]Cl_3$ and $[Co(H_2O)_6]Cl_2$ under near-neutral pH (6-7).

Finally, we also sought to obtain a better understanding of the intermediate(s) involved in the reaction and its overall kinetics. For this we irradiated a solution of pentaamminechlorocobalt(III) chloride, $[Co(NH_3)_5Cl]Cl_2$, starting at pH 6.5. Every 4 h, the reaction mixture was centrifuged, the Co(O)OH precipitate removed, and the absorption of the supernatant recorded. The supernatant was then irradiated again for 4 h. This procedure was repeated four times, for a total irradiation time of 16 h. The resulting series of spectra obtained for the supernatant solution show that the initial $[Co(NH_3)_5Cl]^{2+}$ ion is first transformed to the aquation product, $[Co(NH_3)_5(OH_2)]^{3+}$ in under 4 h, as evidenced by a blue-shift in λ_{max} from 525 nm to 509 nm, respectively (Figures 1 and 7). The estimated apparent rate of reaction under these conditions is $\approx$ 0.4 mM/h with a 1st half-life of approximately 9 hours.
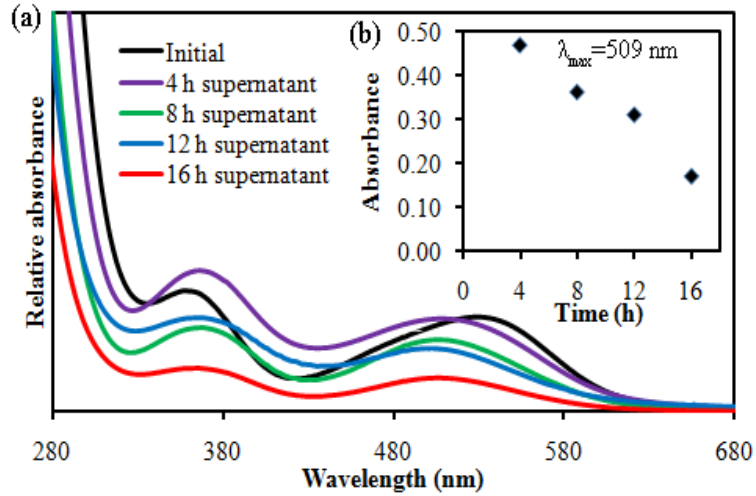
Figure 7. UV-Vis spectra of optically clear supernatant solutions during photochemical Co(O)OH synthesis (a). Inset (b) shows absorbance at λ_{max} = 509 nm vs. time.
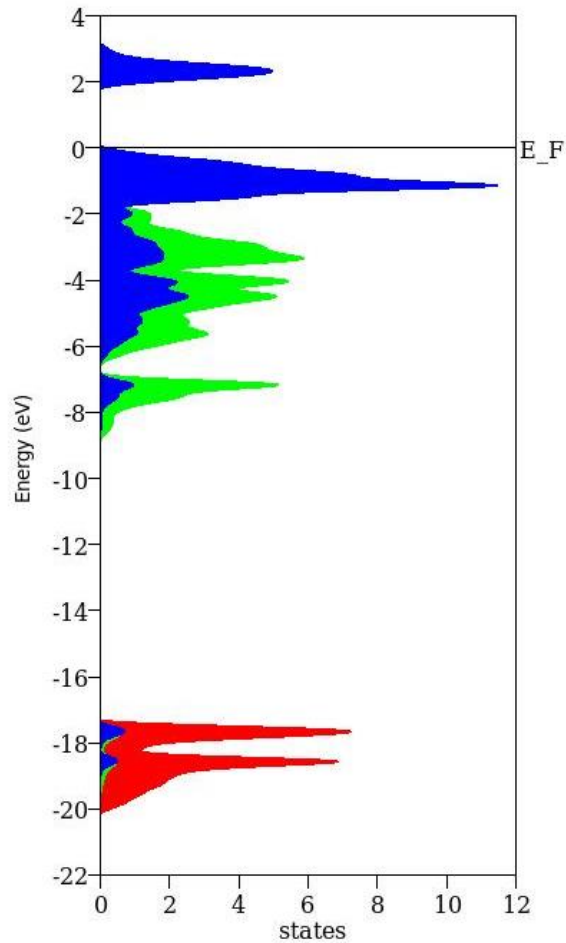
Figure 8. Density of states (DOS) diagram for Co(O)OH calculated using the GGA+U method. Red, green and blue represent states of *s*, *p* and *d* character, respectively.

*Computational modeling.* We used the Vienna Ab-initio Simulation Package, VASP v. 4.6, and the GGA+U method with PBE pseudopotentials to model and estimate the bulk bandgap of cobalt oxyhydroxide, Co(O)OH. We implemented a Hubbard U parameter[42] to better describe the localization of the electrons around the Co^{3+} ions and thus provide a realistic band gap. The GGA+U method provided an accurate description of the band gap in Co_3O_4.[43] Previous quantum chemical modeling yielded a Co(O)OH band gap of 1 eV.[44] A density of states (DOS) diagram computed using a U = 3.2 eV shows a band gap of about 1.7 eV (Figure 8). This is a close fit with our experimental absorption data for thermally prepared Co(O)OH nanocrystals, which show a first absorption peak (shoulder) at approximately 710 nm (1.7 eV) (Figure 1). In contrast, photochemically prepared Co(O)OH nanocrystals show a significantly bluer first absorption peak (shoulder) at approximately 650 nm (1.9 eV). Because the average single crystal domain (grain) size obtained from XRD for thermally prepared Co(O)OH (ca. 17 nm, Table 1) is significantly larger than for photochemically prepared Co(O)OH (ca. 3 nm, Table 1), we conclude that there is some degree of quantum confinement in the latter. Using only GGA-PBE yielded a band gap of 0.6 eV (2,067 nm). Adding U = 1.0 eV gave a band gap of ca. 1.0 eV (1,240 nm), while a value of U = 4.0 eV gave an unrealistically large band gap of 2.0 eV (620 nm). The partial density of states diagram shows that the *d*-orbital splitting in Co^{3+} is the source of this band gap (Figure 8).
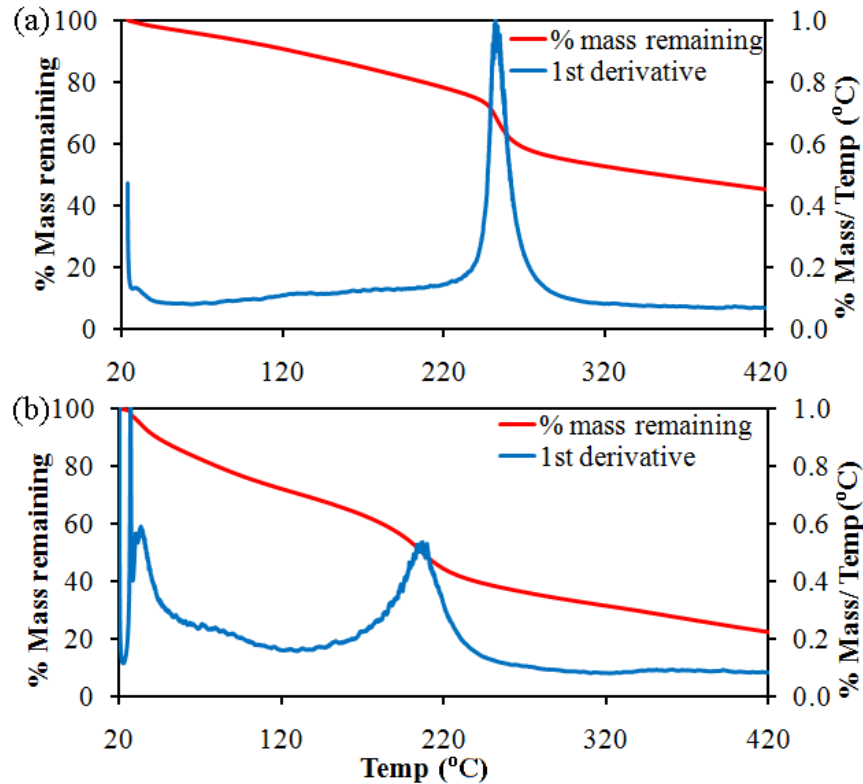
Figure 9. TGA of thermally-(a) and photochemically-prepared (b) Co(O)OH nanocrystals.

Thermal analysis. We used thermogravimetric analysis (TGA) to probe the temperature-induced mass loss of photochemically- and thermally-prepared Co(O)OH (Figure 9). In both cases, plots of mass loss versus temperature show a major change corresponding to the phase transition from cobalt oxyhydroxide to mixed-cobalt(II,III) oxide: $12Co(O)OH \rightarrow 4Co_3O_4 + 6H_2O + O_2$.[14] Interestingly, this transition occurs at significantly lower temperature for photochemically-prepared Co(O)OH, 206 °C, than for thermally-prepared Co(O)OH, 251°C. In the bulk, the reported transition temperature is even higher, 258-270 °C. We attribute this significant drop in phase transition temperature to a sharp decrease in the amount of heat needed to phase transform very small ca. 3 nm (photochemical) Co(O)OH nanocrystallites to Co_3O_4 compared to larger ca. 250 nm (thermal) nanocrystallites or bulk Co(O)OH (Table 1, Figure 9).[45-50]

Preparative transformation of Co(O)OH into Co₃O₄ nanocrystals. Based on our TGA analysis, we explored the synthetic utility of Co(O)OH in making Co$_3$O$_4$ nanocrystals.[14,20,51-53] Heating the photochemically-prepared Co(O)OH to 250 °C for 30 min or the thermally-prepared Co(O)OH to 280 °C for 30 min leads to the formation of cobalt(II,III) oxide, Co$_3$O$_4$, as confirmed by UV-Vis and XRD. In both cases, the UV-Vis spectrum of the annealed product is significantly red shifted compared to the starting material, with new λ_{max} appearing at 400 nm (3.1 eV) and 750 nm (1.7 eV) (Figure 1). The reddest peak (band offset) is not far from the literature band gap of 1.5 eV (827 nm),[54] and is visually manifested by a color change from brown for Co(O)OH to very dark/off-gray for Co$_3$O$_4$. The powder XRD pattern of the annealed samples shows disappearance of the major Co(O)OH peak at $2\theta = 20°$ and appearance of a smaller Co$_3$O$_4$ peak at $2\theta = 18°$ (Figure 2). Co$_3$O$_4$ has a spinel structure (lattice parameter $a =$ 8.08 Å) made of cubic close-packed O^{2-} ions with Co^{2+} and Co^{3+} ions in tetrahedral and Co^{3+} octahedral holes, respectively. Interestingly, TEM micrographs of Co$_3$O$_4$ nanocrystals reveal a similar size, morphology and level of aggregation compared to the Co(O)OH starting materials.[14,20] Co$_3$O$_4$ nanocrystals obtained from annealing the photochemically-prepared Co(O)OH nanocrystals are very small, 5.0 nm ± 1.0 nm (Table 1, Figure 5). To the best of our knowledge, this is one of the smallest Co$_3$O$_4$ nanocrystallite sizes reported in the literature.[55] In contrast, TEM micrographs of Co$_3$O$_4$ nanocrystals obtained from annealing the thermally-prepared Co(O)OH nanocrystals show presence of 30 nm × 3 nm crystalline rods embedded within larger ca. 150 nm aggregates (Figure 5 and Table 1). The morphologies observed by TEM correlate with the relative crystalline domains (grain sizes) of ca. 3.8 nm (photochemical Co(O)OH precursor) and ca. 39 nm (thermal Co(O)OH precursor) for Co$_3$O$_4$ nanocrystals obtained from XRD peak widths (Table 1).[34] Therefore, the size and morphology of Co(O)OH

starting material controls to a significant extent the size and morphology of the Co_3O_4 product.[56-59] Similar transformations starting from $Co(O)OH$ may be useful in the fabrication of lithium storage materials such as lithium cobalt oxide, $LiCoO_2$.

Conclusions

In summary, we found a fast, low temperature and scalable photochemical route to synthesize very small (~3 nm) monodisperse cobalt oxyhydroxide $Co(O)OH$ nanocrystals. This method uses readily and commercially available $[Co(NH_3)_5Cl]Cl_2$ under acidic or neutral pH and proceeds under either near-UV (350 nm) or Vis (575 nm) illumination. Control experiments showed that the reaction proceeds at competent rates only in the presence of light, does not involve a free radical mechanism, is insensitive to O_2, and proceeds via two steps: (1) Aquation of $[Co(NH_3)_5Cl]^{2+}$ to yield $[Co(NH_3)_5(H_2O)]^{3+}$, followed by (2) slow, photochemical release of NH_3 from this complex. This reaction is slow enough for $Co(O)OH$ to form, but fast enough so that nanocrystals are small (ca. 3 nm). The alternative dark thermal reaction proceeds much more slowly and produces much larger (~250 nm) polydisperse $Co(O)OH$ aggregates. UV-Vis absorption measurements and ab-initio calculations yielded a $Co(O)OH$ band gap of 1.7 eV. Fast thermal annealing of $Co(O)OH$ nanocrystals leads to Co_3O_4 nanocrystals with overall retention of nanoparticle size and morphology. Thermogravimetric analysis showed that the oxyhydroxide to mixed-oxide phase transition occurs at significantly lower temperatures (up to $\Delta T = 64°C$) for small nanocrystals compared to the bulk material. We expect that the use of similar photochemical methods will permit the generation, isolation and study of other metastable nanomaterials of unusual size, composition, and morphology. These harder-to-isolate and highly

reactive phases, inaccessible using conventional high-temperature pyrolysis, are likely to possess enhanced and unprecedented chemical, electro-magnetic and catalytic properties.

Acknowledgments

References

[1] Talapin, D. V.; Lee, J.-S.; Kovalenko, M. V.; Shevchenko, E. V. *Chem. Rev.* **2010**, *110*, 389–458.

[2] Park, J.; Joo, J.; Kwon, S. G.; Jang, Y.; Hyeon, T. *Angew. Chem. Int. Ed.* **2007**, *46*, 2–33.

[3] Pinna, N.; Niederberger, M. *Angew. Chem. Int. Ed.* **2008**, *47*, 5292–5304.

[4] Norris, D. J.; Efros, A. L.; Erwin, S. C. *Science* **2008**, *319*, 1776–1779.

[5] Bryan, J. D.; Gamelin, D. R. *Prog. Inorg. Chem.* **2005**, *54*, 47–126.

[6] Sakamoto, M.; Fujistuka, M.; Majima, T. *J. Photochem. Photobio. C* **2009**, *10*, 33–56.

[7] Webber, D. H.; Brutchey, R. L. *Inorg. Chem.* **2011**, *50*, 723–725.

[8] Webber, D. H.; Brutchey, R. L. *Chem. Commun.* **2009**, 5701–5703.

[9] Alemseghed, M. G.; Ruberu, T. P. A.; Vela, J. *Chem. Mater.* **2011**, *23*, 3571–3579.

[10] Ruberu, T. P. A.; Vela, J. *ACS Nano* **2011**, *5*, 5775–5784.

[11] McGilvray, K. L.; Decan, M. R.; Wang, D.; Scaiano, J. C. *J. Am. Chem. Soc.* **2006**, *128*, 15980–15981.

[12] Kim, F.; Song, J. H.; Yang, P. *J. Am. Chem. Soc.* **2002**, *124*, 14316–14317.

[13] Kamada, K.; Horiguchi, K.; Hyodo, T.; Shimizu, Y. *Cryst. Growth Des*. **2011**, *11*, 1202–1207.

[14] Yang, J.; Liu, H.; Martens, W. N.; Frost, R. L. *J. Phys. Chem. C* **2010**, *114*, 111–119.

[15] Stone, A. T.; Ulrich, H.-J. *J. Colloid Interface Sci.* **1989**, *132*, 509–522.

[16] Myers, J. C.; Penn, R. L. *J. Phys. Chem. C* **2007**, *111*, 10597–10602.

[17] Myers, J. C.; Penn, R. L. *Langmuir* **2011**, *27*, 158–165.

[18] Powell, D.; Cortez, J.; Mellon, E. K. *J. Chem. Ed.* **1987**, *64*, 165–167.

[19] Schäffer, S. C.; Schäffer, C. E. *J. Chem. Ed.* **1996**, *73*, 180–181.

[20] Geng, B.; Zhan, F.; Fang, C.; Yu, N. *J. Mater. Chem.* **2008**, *18*, 4977–4984.

[21] Pralong, V.; Delahaye-Vidal, A.; Beaudoin, B.; Gérand, B.; Tarascon, J.-M. *J. Mater. Chem.* **1999**, *9*, 955–960.

[22] Bardé, F.; Palacin, M.-R.; Beaudoin, B.; Delahaye-Vidal, A., and Tarascon, J.-M. *Chem. Mater.* **2004**, *16*, 299–306.

[23] Yang, J.; Sasaki, T. *Chem. Mater.* **2008**, *20*, 2049–2056.

[24] Oaki, A.; Imai, H. *Chem. Eur. J.* **2007**, *13*, 8564–8571.

[25] Zhu, Y.; Li, H.; Koltypin, Y.; Gedanken, A. *J. Mat. Chem.* **2002**, *12*, 729–733.

[26] Zhang, B.; Harb, J. N.; Davis, R. C.; Kim, J.-W.; Chu, S.-H., Choi, S.; Miller, T.; Watt, G. D. *Inorg. Chem.* **2005**, *44*, 3738–3745.

[27] Douglas, T.; Stark, V. T. *Inorg. Chem.* **2000**, *39*, 1828–1830.

[28] Allen, M.; Willits, D.; Young, M.; Douglas, T. *Inorg. Chem.* **2003**, *42*, 6300–6305.

[29] Haim, A.; Taube, H. *J. Am. Chem. Soc.* **1963**, *85*, 495-500.

[30] Riordan, A. R.; Jansma, A.; Fleischman, S.; Green, D. B.; Mulford, D. R. *Chem. Educator* **2005**, *10*, 115–119.

[31] Blochl, P. E. *Phys. Rev. B* **1994**, *50*, 17953–17979.

[32] Perdew, J. P.; Burke, K.; Ernzerhof, M. *Phys. Rev. Lett.* **1996**, *77*, 3865–3868.

[33] Biesinger, M. C.; Payne, B. P.; Grosvenor, A. P.; Lau, L. W. M, Gerson, A. R.; Smart, R. S. *Appl. Surf. Sci.* **2011**, *257*, 2717–2730.

[34] McIntyre, N. S.; Cook, M. G. *Anal. Chem.* **1975**, *47*, 2208–2213.

[35] Holzwarth, U.; Gibson, N. *Nature Nanotech.* **2011**, *6*, 534.

[36] Adamson, A. W.; Waltz, W. L.; Zinato, E.; Watts, D. W.; Fleischauer, P. D.; Lindholm, R. D. *Chem. Rev.* **1968**, *68*, 541–585.

[37] Pribush, P. A.; Poon, C. K.; Bruce, C. M.; Adamson, A. W. *J. Am. Chem. Soc.* **1974**, *96*, 3027–3032.

[38] Powell, D.; Cortez, J.; Mellon, E. K. *J. Chem. Ed.* **1987**, *64*, 165–167.

[39] Chivot, J.; Mendoza, L.; Mansour, C.; Pauporté, T.; Cassir, M. *Corrosion Sci.* **2008**, *50*, 62–69.

[40] Adamson, A. W. *Dis. Faraday Soc.* **1960**, *29*, 163–168.

[41] Endicott, J. F.; Hoffman, M. Z. *J. Am. Chem. Soc.* **1965**, *87*, 3348–3357.

[42] Adamson, A. W.; Sporer, A. H. *J. Am. Chem. Soc.* **1958**, *80*, 3865–3870.

[43] King'ondu, C. K.; Iyer, A.; Njagi, E. C.; Opembe, N.; Genuino, H.; Huang, H.; Ristau, R. A.; Suib, S. L. *J. Amer. Chem. Soc.* **2011**, *133*, 4186–4189.

[44] Albers, R.C.; Christensen, N.E.; Svane, A. *J. Phys.: Condens. Matter* **2009**, *21*, 343201.

[45] Chen, J.; Wu, X.; Selloni, A. *Phys. Rev. B* **2011**, *83*, 245204.

[46] Wass, J. R.; Panas, I.; Ásbjörnsson, J.; Ahlberg, E. *J. Electroanal. Chem.* **2007**, *599*, 295–312.

[47] Chen, C.-C.; Herhold, A. B.; Johnson, C. S.; Alivisatos, A. P. *Science* **1997**, *276*, 398–401.

[48] Tolbert, S. H.; Alivisatos, A. P. *Science* **1994**, *265*, 373–376.

[49] Clark, S. M.; Prilliman, S. G.; Erdonmez, C. K.; Alivisatos, A. P. *Nanotechnology* **2005**, 2813–2818.

[50] Baldinozzi, G.; Simeone, D.; Gosset, D.; Dutheil, M. *Phys. Rev. Lett.* **2003**, *90*, 216103.

[51] Alivisatos, A. P. *J. Phys. Chem.* **1996**, *100*, 13226–13239.

[52] Burda, C.; Chen, X.; Narayanan, R.; El-Sayed, M. A. *Chem. Rev.* **2005**, *105*, 1025–1102.

[53] Chen, C. H.; Abbas, S. F.; Morey, A.; Sithambaram, S.; Xu, L. P.; Garces, H. F.; Hines, W. A.; Suib, S. L. *Adv. Mater.* **2008**, *20*, 1205–1209.

[54] O'Brien, P.; Patel, U. *J. Chem. Soc. Dalton Trans.* **1982**, 1407–1409.

[55] Xu, Z. P.; Zeng, H. C. *J. Mater. Chem.* **1998**, *8*, 2499–2506.

[56] Pauporté, T.; Mendoza, L.; Cassir, M.; Bernard, M. C.; Chivot, J. *J. Electrochem. Soc.* **2005**, *152*, C49–C53.

[57] Ichiyanagi, Y.; Yamada, S. *Polyhedron* **2005**, *24*, 2813–2816.

[58] Leonard, B. M.; Anderson, M. E.; Oyler, K. D.; Phan, T.-H.; Schaak, R. E. *ACS Nano* **2009**, *3*, 940–948.

[59] Schaefer, Z. L.; Vaughn, D. D.; Schaak, R. E. *J. Alloys Compd.* **2010**, *490*, 98–102.

[60] Son, D. H.; Hughes, S. M.; Yin, Y.; Alivisatos, A. P. *Science* **2004**, *306*, 1009–1012.

[61] Li, H.; Zanella, M.; Genovese, A.; Povia, M.; Falqui, A.; Giannini, C.; Manna, L. *Nano Lett.* **2011**, *11*, 4964–4970.

[62] Jensen, K. M. Ø.; Christensen, M.; Tyrsted, C.; Bremholm, M.; Iversen, B. B. *Cryst. Growth Des.* **2011**, *11*, 753–758.

Appendix of supporting information
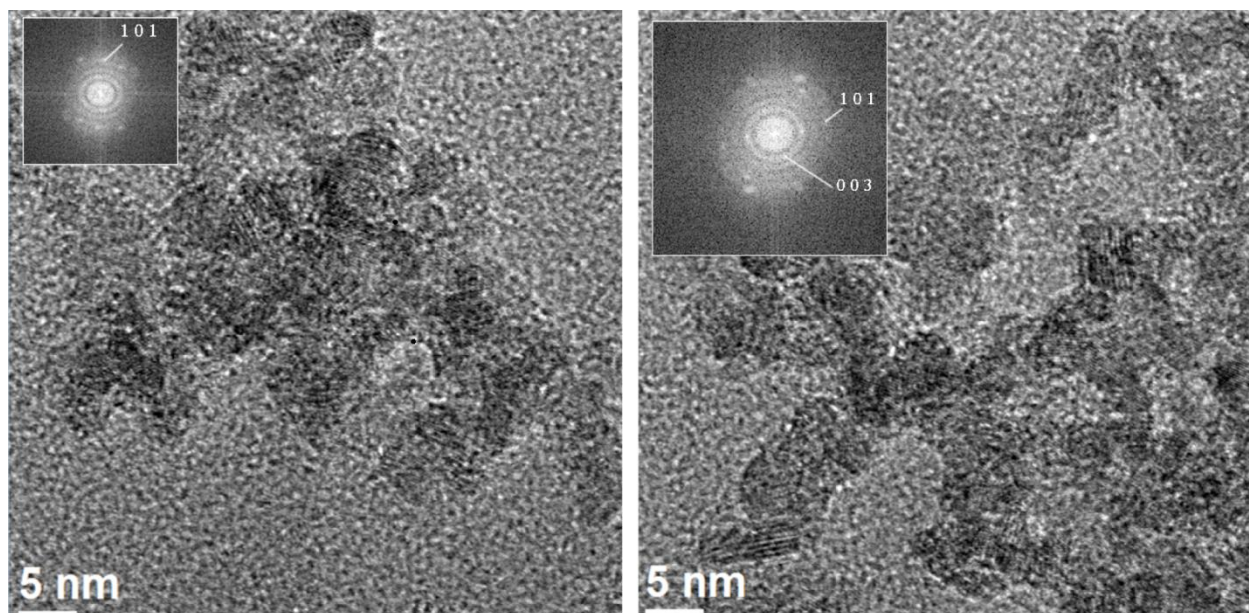
Figure S1. High-resolution (HR) TEM and indexed selected area diffraction (SAD) (insets) of photochemically-prepared Co(O)OH nanocrystals.

CHAPTER 3

SHAPE-PROGRAMMED NANOFABRICATION: UNDERSTANDING THE REACTIVITY OF DICHALCOGENIDE PRECURSORS

Samuel R. Alvarado, Yijun Guo, Joshua D. Barclay, Javier Vela

Abstract

Dialkyl and diaryl dichalcogenides are highly versatile and modular precursors for the synthesis of colloidal chalcogenide nanocrystals. We have used a series of commercially available dichalcogenide precursors to synthesize II-VI semiconductor nanocrystals with a wide variety of shapes and sizes. Specific dichalcogenide precursors used are diallyl-, dibenzyl-, ditertbutyl-, diisopropyl-, diethyl-, dimethyl- and diphenyl-disulfide and diselenide. We find that the presence of two distinctively reactive C-E and E-E bonds makes the chemistry of these precursors much richer and more interesting than that of other precursors such as the more common phosphine chalcogenides. Computational studies (DFT) reveal that the dissociation energy of carbon-chalcogen (C-E) bonds in dichalcogenide precursors (R-E-E-R, E = S or Se) increases in the order (R): Diallyl < dibenzyl < ditertbutyl < diisopropyl < diethyl < dimethyl < diphenyl. The dissociation energy of chalcogen-chalcogen (E-E) bonds remains relatively constant across the series. The only exceptions are diphenyl dichalcogenides, which have much lower E-E bond dissociation energies. A decrease in C-E dissociation energy and with it R-E-E-R precursor reactivity leads to progressively slower nucleation and higher selectivity for anisotropic growth, all the way from dots to pods to tetrapods. Under identical experimental

conditions, we obtain CdS and CdSe nanocrystals with spherical, elongated or tetrapodal morphology by simply varying the identity and reactivity of the dichalcogenide precursor. Interestingly, we find that precursors with strong C-E and weak E-E bond dissociation energies such as Ph-S-S-Ph serve as a ready source of thiol radicals that stabilize small CdE nuclei, facilitating anisotropic growth. These CdS and CdSe nanocrystals have been characterized using structural and spectroscopic methods. An intimate understanding of how molecular structure affects the chemical reactivity of molecular precursors enables highly predictable and reproducible synthesis of colloidal nanocrystals with specific sizes, shapes and optoelectronic properties for customized applications.

Introduction

Dialkyl dichalcogenides (R-E-E-R; where R = alkyl or aryl, E = S, Se or Te) recently re-emerged as highly versatile molecular precursors for the solution-phase synthesis of colloidal nanocrystals. Intriguingly, these dichalcogenides enable the isolation of metastable nanocrystalline phases with unusual composition and morphology. tBu-E-E-tBu (E = S or Se) precursors allow the isolation of $CuInE_2$ and Cu_2SnE_3 nanocrystals with metastable wurtzite phases.[1,2] A change in reaction solvent from oleylamine to squalene leads to $CuInE_2$ nanocrystals with the more stable chalcopyrite phase.[2,3] tBu-S-S-tBu serves as precursor to In_2S_3 nanorods,[4] $Sn_xGe_{1-x}Se$ nanocrystals,[5] and $Cu_{2-x}S$ nanocrystals with a wide range of morphologies (from dots to dodecahedrons).[6] tBu-Se-Se-tBu serves as precursor to SnSe[7] and hexagonal BiSe[8] nanocrystals. Photolysis of tBu-Te-Te-tBu in aqueous micellar conditions yields Te^0 nanorods.[9] Aqueous reaction of Me-Se-Se-Me with $SnCl_2$ in an autoclave yields SnSe nanosheets.[10] Ph-Se-Se-Ph allows the isolation of hexagonal and cubic nanocrystals of $CuInSe_2$ and $Cu_{2-x}S_ySe_{1-y}$.[11,12]

Ph-Se-Se-Ph and Ph-Te-Te-Ph are useful alternatives to elemental chalcogenide precursors (Se or Te) in the synthesis of star-shaped SnTe and SnSe nanoparticles.[13] In spite of their very rich chemistry, it remains unclear what factors play a determinant role in the outcome of specific nanocrystal preparations.

Using the far more common phosphine-chalcogenide precursors, we recently found that a single injection of premixed trioctylphosphine-sulfide (Oct$_3$PS) and selenide (Oct$_3$PSe) to a bis-octadecylphosphonate-cadmium complex (Cd(ODPA)$_2$) at 320 °C produces axially anisotropic CdS$_{1-x}$Se$_x$ nanorods characterized by having a thick, CdSe-rich "head" and a thin, CdS-rich "tail."[14,15] Using a combined experimental and computational approach, we showed that the mechanism of formation mechanism and the S-to-Se content of these compositionally graded CdS$_{1-x}$Se$_x$ nanorods are direct consequences of relative phosphine-chalcogenide precursor reactivity. Further, by tuning the sterics and electronics of a family of closely related R$_3$P=E precursors (R = amide, alkyl, aryl or aryloxy; E = S or Se), we reproducibly and predictably synthesized CdE nanorods with controllable aspect (length-to-diameter) ratios between 10-100.[16] These observations open new avenues for achieving "bottom-up," molecular-level control of composition, morphology and properties at the nanoscale.

Unlike phosphine-chalcogenides (R$_3$P=E), which contain only one type of reactive bond (P=E), dichalcogenide precursors (R-E-E-R) contain two different types of reactive bonds (C-E and E-E). We were intrigued by the inherent modularity of these molecular precursors, and wondered how varying the substituents (R = alkyl, aryl) around the reactive -E-E- unit could affect dichalcogenide precursor reactivity and, ultimately, the outcome of nanocrystal preparations. Experimentally, we observe that differently substituted dichalcogenides lead to completely different nanocrystal morphologies, some lead to dots, others to rods or tetrapods.

The selectivity for such anisotropic structures is obviously affected by reaction parameters such as reaction time[17] and temperature,[18,19] precursor concentration,[20] medium acidity,[21] ligand type (amines,[22-24] halides,[52] phosphonic acids[25,26]) and chain length.[27,28] Commonly used methods to obtain II−VI and IV-VI rods and tetrapods include seeded growth,[29-32] continuous precursor injection,[33,34] and noninjection routes.[35] Dichalcogenides offer a unique system where the selectivity for anisotropic structures under identical experimental conditions can be directly traced back to the molecular structure and chemical reactivity of the molecular precursor used. Here we present the results of a combined experimental and computational study aimed at addressing this question.

Experimental

Materials. Cadmium oxide (CdO, 99.998%) and oleic acid (90%) were purchased from Alfa Aesar; diallyl disulfide (Allyl-S-S-Allyl, 80%), dibenzyl disulfide (Bn-S-S-Bn, 98%), ditertiarybutyl disulfide (tBu-S-S-tBu, 97%), diisopropyl disulfide (iPr-S-S-iPr, 96%), diethyl disulfide (Et-S-S-Et, 99%), dimethyl disulfide (Me-S-S-Me, 99%), and dimethyl diselenide (Me-Se-Se-Me, 96%) from Sigma-Aldrich; diphenyl disulfide (Ph-S-S-Ph, 99%), 1-octadecene (ODE, 90%), and oleylamine (80-90%) from Acros; diethyl diselenide (Et-Se-Se-Et) and diphenyl diselenide (Ph-Se-Se-Ph, 98%) from Strem.

Synthesis. *Dichalcogenide addition solution.* Inside a glove box filled with dry N$_2$, the dichalcogenide precursor (0.42 mmol) (61.0 mg Allyl-S-S-Allyl, 104 mg Bn-S-S-Bn, 75.0 mg tBu-S-S-tBu, 63.1 mg iPr-S-S-iPr, 51.0 mg Et-S-S-Et, 39.6 mg Me-S-S-Me, 91.0 mg Et-Se-Se-Et, 79.0 mg Me-Se-Se-Me, or 131 mg Ph-Se-Se-Ph) was thoroughly dissolved in ODE (1.00 g, 1.27 mL) to afford a homogeneous mixture. *Cadmium chalcogenide particles.* Inside a three-

neck-flask, CdO (51.2 mg, 0.40 mmol), oleic acid (2.24 g, 8.00 mmol), oleylamine (2.14 g, 8.00 mmol) and ODE (2.62 g, 3.32 mL) were degassed under vacuum at 80 °C for 30 min, refilled with Ar, and heated to 180 °C for 10 min until the mixture became a homogeneous, optically clear solution. The solution was cooled to 80 °C, degassed under vacuum at 80 °C for 30 min, refilled with Ar, and heated to 250 °C. After 5 min, the dichalcogenide addition solution (above) was quickly injected. Aliquots (0.10 mL) were taken at different times, added to the same amount of toluene (3 mL) every time, and analyzed by UV-Vis absorption and PL. After 40 min (disulfides) or 5-40 min (diselenides, see below), the mixture was allowed to cool to room temperature (RT). Nanocrystals were isolated and purified twice by washing with a 1:2 v/v acetone-methanol mixture and centrifugation at 4900 rpm for 5 min.

Optical Characterization. Absorption spectra were measured with a photodiode array Agilent 8453 UV-Vis spectrophotometer. Steady-state PL spectra were measured with a Horiba-Jobin Yvon Nanolog scanning spectrofluorometer equipped with a photomultiplier detector.

Structural Characterization. *Powder X-ray diffraction* (XRD) was measured using Cu Kα radiation on a Scintag XDS-2000 diffractometer. *Transmission Electron Microscopy* (TEM) was conducted on carbon-coated copper grids using a FEI Technai G2 F20 field emission scanning transmission electron microscope (STEM) at 200 kV (point-to-point resolution <0.25 nm, line-to-line resolution <0.10 nm). *Particle dimensions* were measured manually and/or with ImageJ for >50-100 particles. Averages are reported ± one standard deviation.

Computational methods. Bond dissociation energies (BDEs) were calculated using GAMESS[36,37] at the DFT[38] level of theory with the BMK (Boese-Martin Kinetics) functional,[39] which has been shown to provide accuracy near that of high-precision complete basis set (CBS) methods.[40,41] Geometries were optimized using the 6-31G(d) basis set[42] followed by single point

calculations with the 6-311G(d,p) basis set[43] to determine BDEs.[44] Frequency calculations were performed to obtain zero point energies and enthalpies at 273 K and to ensure that the Hessian matrices of the optimized geometries contained no negative eigenvalues.[45]

Results and discussion

Seeking a deeper understanding of how molecular structure affects chemical precursor reactivity, we subjected different disubstituted dichalcogenides to a consistent set of nanocrystal forming conditions (Scheme 1). Briefly, we injected individual dichalcogenide precursors (1.1 equiv.) to a freshly generated solution of Cd(oleate)$_2$ (0.40 mol), oleic acid (20 equiv.) and oleylamine (20 equiv.) in 1-octadecene (ODE) (4.6 mL) at 250 °C. At regular intervals, we took small equal aliquots from the reaction mixture and monitored nanocrystal evolution (nucleation, growth, and ripening) by optical spectroscopy. After 40 min at 250 °C, we isolated and fully characterized the nanocrystalline products. We repeated this procedure for several different commercially available dichalcogenides having different alkyl and aryl substituents.

Cd(oleate)$_2$ + R-E-E-R $\xrightarrow[\text{250°C / ODE, 40 min}]{\substack{\text{oleylNH}_2 \text{ (20 equiv.)} \\ \text{oleic acid (20 equiv.)}}}$ [CdE]$_n$ (nanocrystals) (E = S or Se)
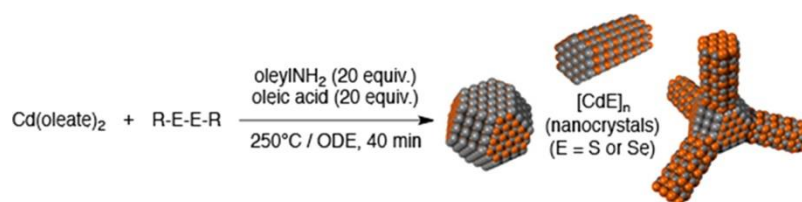
Scheme 1 Reaction to form CdE nanocrystals

Dichalcogenide precursor chemistry: A springboard to nanocrystal shape diversity. Our experimental observations show that, in general, dichalcogenide precursors that reacted quickly produced spherical nanocrystals, while those that reacted more slowly produced nanocrystals of non-spherical morphology (often tetrapods). Figure 1 shows the time evolution of UV-Vis absorption spectra as well as final (after 40 min) TEM images of CdS nanocrystals obtained with

different dialkyl disulfides (R-S-S-R). UV-Vis spectroscopy shows the appearance of the first absorption (1*S*) peak characteristic of CdS nanocrystals within a few minutes for most precursors. Transmission electron microscopy (TEM) images show that some dichalcogenide precursors lead to the formation of CdS nanocrystals with a spherical morphology, while others lead to the formation of CdS nanocrystals with a tetrapod morphology.[46-48] The majority of spherical CdS nanocrystals (dots) have a zinc blende (cubic) structure, while the CdS tetrapods are comprised of wurtzite (hexagonal) arms extending from the {111} facets of zinc blende (cubic) cores (seeds).[49-51] Based on these results, it is clear that the structure of the molecular precursor has considerable influence on the rate of growth, size and morphology of the resulting nanocrystals.
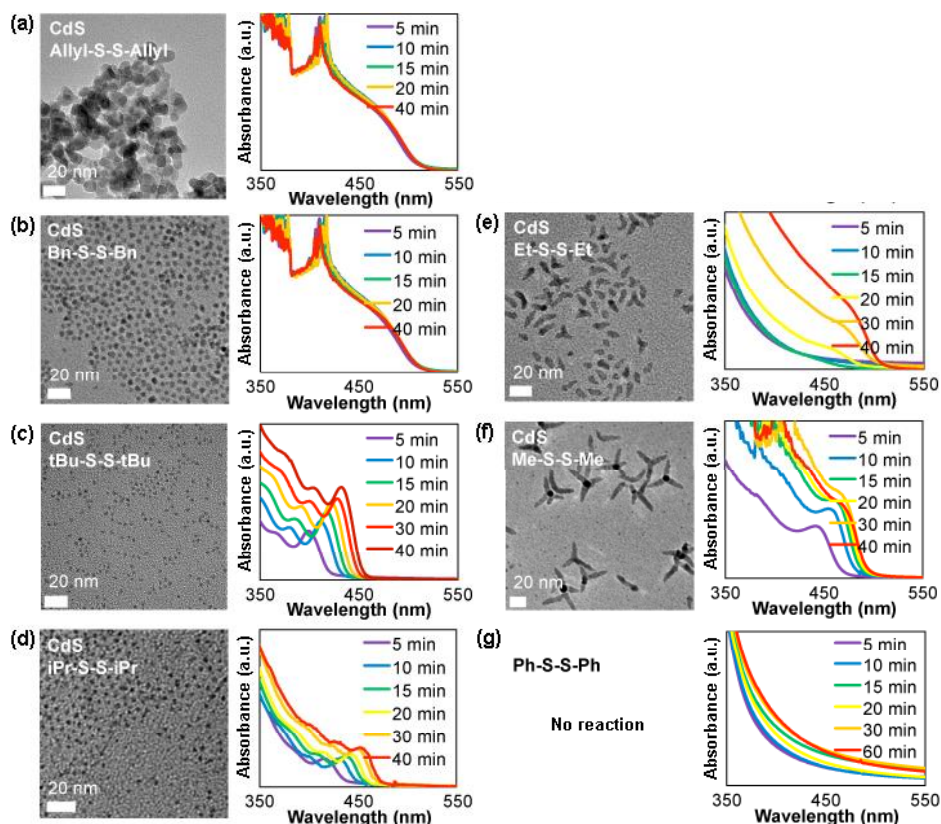
Figure 1. Representative TEM images after 40 min (left panel) and time evolution of UV-Vis absorption spectra (right panel) of CdS nanocrystals obtained with (a) diallyl-, (b) dibenzyl-, (c) ditertbutyl-, (d) diisopropyl-, (e) diethyl- and (f) dimethyl-disulfide precursors. (g) Diphenyl-disulfide was unreactive

under identical conditions (0.40 mol Cd(oleate)$_2$, 1.1 equiv. R-S-S-R, 20 equiv. oleic acid, 20 equiv. oleylamine, 4.6 mL ODE, 250 °C).

Assessing the strength of C-E and E-E bonds from computations. To better understand these observations, we computationally studied the different dichalcogenide precursors using the GAMESS software. We computed their carbon-chalcogen (C-E) and chalcogen-chalcogen (E-E) bond dissociation energies (BDEs, Scheme 2) using density functional theory (DFT) with the Boese-Martin Kinetics (BMK) functional, which has been shown to be a viable method to calculate thermodynamic properties such as BDEs at a lower computational cost than high-precision methods such as G3. Table 1 and Figure 2 show the computed BDEs of all precursors we investigated. Full computational results, including bond distances and dihedral angles are available in the Appendix.
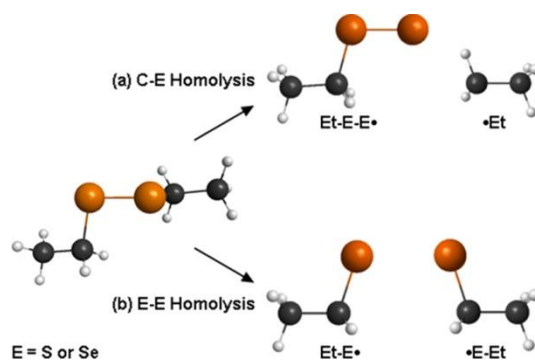
Scheme 2

Table 1. Calculated bond dissociation (homolysis) energies (BDEs) for dialkyl dichalcogenide precursors (R-E-E-R, E = S or Se) and experimentally observed products from their reaction with Cd(oleate)$_2$.[a]

Precursor(s) R-E-E-R (E = S or Se)	C-E BDE kcal/mol	E-E BDE kcal/mol	(C-E)-(E-E) kcal/mol	40 min Product morphology (1S peak)	Size[b] / nm
Allyl-S-S-Allyl	45.71	61.33	-15.62	Nanocrystals[c] (480 nm)	9.4 ± 1.3
Bn-S-S-Bn	48.50	62.45	-13.94	Nanocrystals[c] (480 nm)	4.2 ± 0.6

Table 1 continued

tBu-S-S-tBu	52.81	59.39	-6.59	Quantum dots[c] (430 nm)	2.2 ± 0.2
iPr-S-S-iPr	55.45	59.69	-4.24	Quantum dots[c] (450 nm)	1.8 ± 0.3
Et-S-S-Et	58.13	59.48	-1.35	Pods/Multipods (470 nm)	Pod length: 10.3 ± 2.8 Pod width: 5.1 ± 0.6
Me-S-S-Me	59.03	58.04	+0.99	Tetrapods (465 nm)	Pod length: 19.5 ± 2.9 Pod width: 5.5 ± 0.5
Ph-S-S-Ph	69.75	45.65	+24.11	No reaction (n.a.)	-
Bn-S-S-Bn + Ph-S-S-Ph (1:1)	-[d]	-[d]	-[d]	Rods (470 nm)	Rod length: 11.5 ± 1.5 Rod width: 4.4 ± 0.5
tBu-S-S-tBu + Ph-S-S-Ph (1:1)	-[d]	-[d]	-[d]	Tetrapods (455 nm)	Pod length: 24.1 ± 4.7 Pod width: 3.5 ± 0.4
iPr-S-S-iPr + Ph-S-S-Ph (1:1)	-[d]	-[d]	-[d]	Tetrapods (455 nm)	Pod length: 21.3 ± 4.5 Pod width: 2.3 ± 0.3
Et-Se-Se-Et[e]	52.01	56.41	-4.40	Nanocrystals[c] (670 nm)	6.6 ± 0.6
Me-Se-Se-Me[f]	53.76	51.94	+1.82	Multipod clusters (685 nm)	65.7 ± 13.1
Ph-Se-Se-Ph	64.44	43.63	+20.80	Quantum dots[c] (550 nm)	3.5 ± 0.5

[a]Conditions: 0.40 mol Cd(oleate)$_2$, 1.1 equiv. R-E-E-R, 20 equiv. oleic acid, 20 equiv. oleylamine, 4.6 mL ODE, 250 °C, 40 min (except [e]Et-Se-Se-Et, 10 min, [f]Me-Se-Se-Me, 5 min). [b]Average sizes (50-100 particles) ± one standard deviation. [c]Quantum dots have average diameters smaller than the Bohr radius reported for CdS (2.5-3.0 nm) or CdSe (5.4 nm).[64-66] [d]Not applicable (used a mixture of two precursors, see first column).

C-E and E-E BDEs: Comparison to prior experimental and computational data. In terms of absolute value, our computational results appear to underestimate the experimentally measured values reported previously for disubstituted dichalcogenides, particularly in the case of E-E BDEs. For example, laser photofragmentation time-of-flight mass spectrometric studies of Me-S-S-Me, •S-S-Me, and •S-Me yielded at 0 K a C-S BDE of 55.0 kcal/mol and a S-S BDE of 72.4 kcal/mol at 0 K,[52] compared to our calculated values of 59.03 kcal/mol and 58.04 kcal/mol,

respectively (Table 1). This discrepancy could be due to either computational or experimental error. In terms of the trends observed, our computational results are in agreement with those observed experimentally. E-E BDEs measured experimentally are generally quoted in the range 51-72 kcal/mol;[53] those derived from calorimetry are 66.1 kcal/mol for Et-S-S-Et, 65.2 kcal/mol for Me-S-S-Me, and 51.2 kcal/mol for Ph-S-S-Ph,[54-58] compared to our calculated values of 59.48 kcal/mol, 58.04 kcal/mol, and 45.65 kcal/mol, respectively (Table 1). Our computational results compare well with previous calculations reported for disubstituted dichalcogenide compounds. Early computational references on C-S and S-S BDEs used a complete basis set approach instead of DFT.[59] High-level *ab initio* approaches using G3, G3B3, CBS-Q, CBS-4M, CCSD(T), and ROMP2 were applied to S-S BDEs.[60] A limited DFT study showed the BMK functional provided accuracy close to composite methods, with S-S BDEs of 64.5 kcal/mol for tBu-S-S-tBu, 63.9 kcal/mol for iPr-S-S-iPr, 63.8 kcal/mol for Et-S-S-Et, 62.9 kcal/mol for Me-S-S-Me, and 48.3 kcal/mol for Ph-S-S-Ph.[61] These values and trends roughly agree (within 2-5 kcal/mol) with our computational results of 59.39 kcal/mol, 59.69 kcal/mol, 59.48 kcal/mol, 58.04 kcal/mol, and 45.65 kcal/mol, respectively. Further, all previous computations also find the S-S bond in Ph-S-S-Ph to be significantly weaker than its C-S bond and the S-S bonds of other disulfides. DFT with different functionals other than BMK gave a Se-Se BDE of 51.8 kcal/mol for Me-Se-Se-Me, which compares well with our value of 51.94 kcal/mol.[62,63]

Assessing dichalcogenide precursor reactivity from C-S BDEs. As shown in Table 1 and Figure 2, C-S bond energies progressively increase across the following series: Allyl-S-S-Allyl < Bn-S-S-Bn < tBu-S-S-tBu < iPr-S-S-iPr < Et-S-S-Et < Me-S-S-Me < Ph-S-S-Ph. In contrast, S-S bond energies remain roughly similar along most of the same series from Allyl-S-S-Allyl through Me-S-S-Me, but significantly drop (by about one third) for Ph-S-S-Ph. These trends

greatly help understand our experimental observations. Both of the C-S bonds as well as the S-S bond must break in order to form nanocrystalline CdS. Because the strength of the S-S bond remains fairly constant among most disulfides, *the key factor that mainly determines the overall chemical reactivity of disulfide precursors is the strength of the C-S bond* (Figure 2, Chart 1).
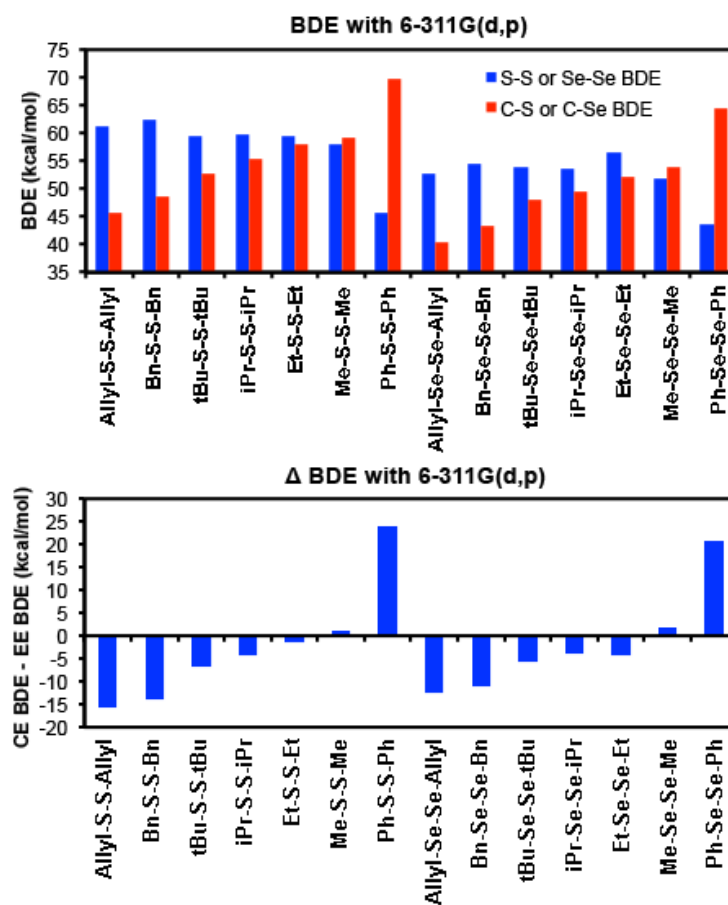
Figure 2. Bond dissociation (homolysis) energies (BDEs) calculated using density functional theory (DFT) with the Boese-Martin Kinetics (BMK) functional in GAMESS. Full computational results, including bond distances and dihedral angles are available in the Appendix.
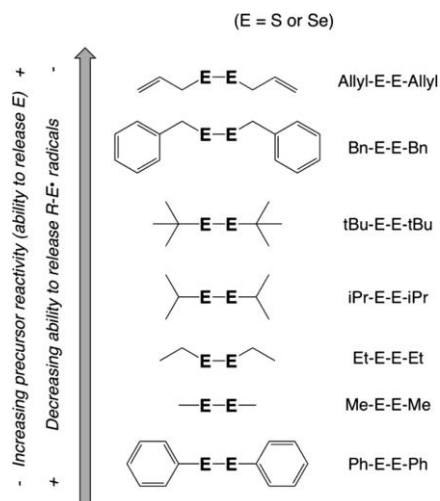
Chart 1

To illustrate, Allyl-S-S-Allyl and Bn-S-S-Bn have the *weakest C-S bonds* (45.71 kcal/mol and 48.50 kcal/mol, respectively) and are therefore the *most reactive precursors* in the series (Chart 1); they quickly (< 5 min) react with Cd(oleate)$_2$ to form large, non-quantum confined spherical CdS nanocrystals (Figure 1a, b). After 40 min, Allyl-S-S-Allyl and Bn-S-S-Bn lead to CdS particle sizes of 9.4 nm ± 1.3 nm and 4.2 nm ± 0.6 nm respectively. In comparison, tBu-S-S-tBu and iPr-S-S-iPr have intermediate C-S bond strengths (52.81 kcal/mol and 55.45 kcal/mol, respectively) and are more mildly reactive; they react less quickly (5-40 min) with Cd(oleate)$_2$ to form small, quantum confined spherical CdS nanocrystals (Figure 1c, d). After 40 min, tBu-S-S-tBu and iPr-S-S-iPr lead to CdS particle sizes of 2.2 nm ± 0.2 nm and 1.8 nm ± 0.3 nm, respectively. For reference, the Bohr radius reported for CdS is between 2.5-3.0 nm.[64-66]

Further decreasing the C-S bond strength and with it, chemical precursor reactivity, results in slower reaction and the selective formation of anisotropic structures. Et-S-S-Et and Me-S-S-Me have strong C-S bonds (58.13 kcal/mol and 59.03 kcal/mol, respectively) and are only weakly reactive; they react very slowly (20-40 min) and selectively with Cd(oleate)$_2$ to grow multipod and tetrapod structures (Figure 1e, f). After 40 min, Et-S-S-Et and Me-S-S-Me

lead to CdS pods and tetrapods, respectively. For Et-S-S-Et, the average pod length and diameter are 10.3 ± 2.8 nm and 5.1 ± 0.6 nm, respectively. For Me-S-S-Me, the average pod length and diameter are 19.5 ± 2.9 nm and 5.5 ± 0.5 nm, respectively. At the end of the series and in stark contrast to all other dichalcogenides we tested, Ph-S-S-Ph has the *strongest C-S bond* (69.75 kcal/mol) and is *unreactive* (Chart 1); Ph-S-S-Ph alone (by itself) does not react with Cd(oleate)$_2$ under identical conditions to those used above for the other precursors (Figure 1).

Compared to the rest of the dichalcogenide precursors we used, Ph-S-S-Ph is different not only because it contains the strongest C-S bond (69.75 kcal/mol), but also because it contains the weakest S-S bond (45.65 kcal/mol). On the contrary, for most of the other dichalcogenides in the series, the calculated S-S bond is either stronger than or as strong as the calculated C-S bonds (Table 1, Figure 2). Examination of the highest occupied (HOMO) and lowest unoccupied (LUMO) molecular orbital diagrams of diphenyl disulfide (Ph-S-S-Ph) reveals a strong overlap between the π orbital on the chalcogen atoms and the π orbital of the adjacent phenyl carbon (Figure 3). This π-π overlap lends partial double bond character to the C-S bond, increasing the C-S bond strength (making it harder to break), and decreasing the C-S bond length (C-S 1.8085 Å for Ph-S-S-Ph *vs.* C-S 1.8494-1.8721 Å for other disulfides, see the Appendix). Other dialkyl dichalcogenides, such as diethyl disulfide (Et-S-S-Et) do not possess such overlap (Figure 3). Based on these differences, we hypothesized that the formation of anisotropic particles may arise from the relative ease (and rate) of C-S *vs.* S-S bond breaking.

Figure 3. Lowest unoccupied (LUMO, top) and highest occupied (HOMO, bottom) molecular orbitals for Et-S-S-Et (a, b) and Ph-S-S-Ph (c, d) plotted with a contour value of 0.02. Calculated using density functional theory (DFT) with the Boese-Martin Kinetics (BMK) functional in GAMESS. Full computational results, including bond distances and dihedral angles are available in the Appendix.
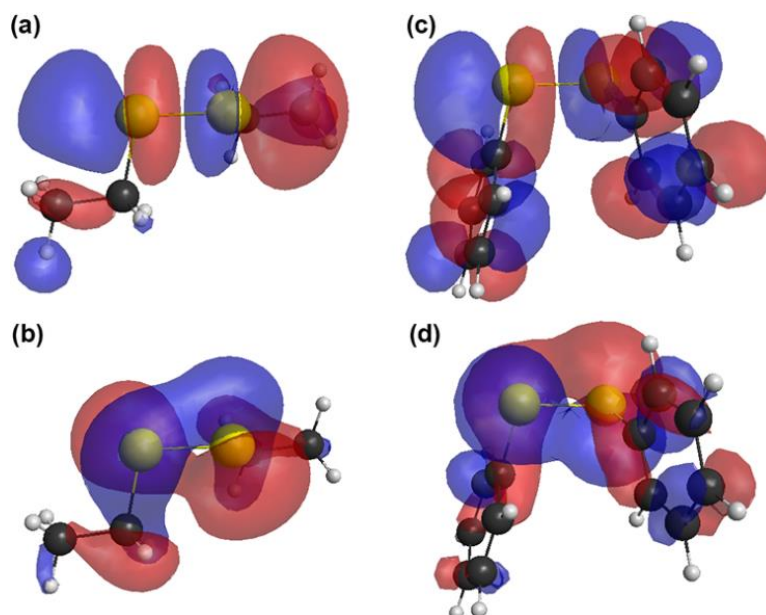
Understanding the formation of anisotropic structures: Molecular origin of nanoscale anisotropy. For Allyl-S-S-Allyl, Bn-S-S-Bn, tBu-S-S-tBu and iPr-S-S-iPr, the C-S bonds are weaker than the S-S bond by at least 5 kcal/mol or more (Table 1, Figure 2); therefore, by the time the C-S bond breaks in these precursors, the S-S bond has already broken, resulting in the release of S equivalents that can proceed to react with Cd(oleate)$_2$ to form spheroidal (0D) nanocrystals. In contrast, for Et-S-S-Et and Me-S-S-Me the C-S and S-S bonds are very similar in energy (only *ca.* 1.35-0.99 kcal/mol apart) (Table 1, Figure 2); therefore, the C-S and S-S bonds break with similar ease and at roughly similar or comparable rates, resulting in the concomitant release of both S, and R-S• radicals (Scheme 2). We expect thiol radicals of the form R-S• to act as excellent ligands due to their high affinity for soft cations and metal surfaces, for example by binding at so called "dangling bonds" or "surface traps".[67] The formation of radicals in these reactions is feasible given the high temperature (250 °C), long time (40 min)

and non-polar medium (octadecene and long chain surfactants) used here. Such harsh conditions are normally conducive to bond homolysis and radical chemistry. *In situ* generated R-S• radicals can act as capping ligands on the CdS surface, passivating the nanocrystals against further growth. Stabilizing and increasing the solution-phase lifetime of small, high-energy surface CdS nuclei could lead slower and more selective nanocrystal growth, resulting in the formation of anisotropic structures such as the pods and tetrapods observed with Et-S-S-Et and Me-S-S-Me (Figure 1e, f). In fact, in the presence of excess O_2, a naturally occurring diradical, $Cd(oleate)_2$ and NaHSe react very slowly and selectively to produce anisotropic CdSe structures (nanowires).[68]

The above situation reverses for the Ph-S-S-Ph precursor, where the calculated C-S bond is much stronger than the calculated S-S bond by 24.11 kcal/mol (Table 1, Figure 2b). This explains the apparent lack of reactivity of Ph-S-S-Ph: The S-S bond breaks very easily but the C-S bond does not, resulting in the facile release of R-S• radicals but not of S (Scheme 2). In fact, even though by itself it does not appear to react with $Cd(oleate)_2$, we reasoned that Ph-S-S-Ph should be extremely efficient at generating R-S• radicals. Because such thiol radicals can serve as surface-passivating ligands, we hypothesized that repeating CdS forming reactions using a mixture of the apparently 'unreactive' Ph-S-S-Ph with a reactive dichalcogenide such as tBu-S-S-tBu or iPr-S-S-iPr should induce the formation of anisotropic structures. As noted above, reacting $Cd(oleate)_2$ with tBu-S-S-tBu or iPr-S-S-iPr normally results in CdS dots (Figure 1b, c). However, mixing any of these two precursors with Ph-S-S-Ph could mimic the situation where a very slowly reacting (and selective) precursor such as Et-S-S-Et or Me-S-S-Me is used; more specifically, tBu-S-S-tBu or iPr-S-S-iPr would serve as a source of S, while Ph-S-S-Ph would serve as a source of surface-stabilizing R-S• radicals.

Inducing anisotropy: Testing the role of in situ generated thiol radicals. Figure 4 shows representative data confirming this prediction: While Ph-S-S-Ph alone is unreactive against Cd(oleate)$_2$, and Bn-S-S-Bn alone leads to quick formation of CdS nanocrystals (Figure 4a, b), a 1:1 mixture of Bn-S-S-Bn and Ph-S-S-Ph leads to the sole, highly-selective formation of CdS rods (Figure 4c). In turn, while tBu-S-S-tBu alone leads to quick CdS dot formation (Figure 4d), a 1:1 mixture of tBu-S-S-tBu and Ph-S-S-Ph leads to highly selective formation of CdS tetrapods (Figure 4e). Similarly, while iPr-S-S-iPr alone leads to quick CdS dot formation (Figure 4f), a 1:1 mixture of iPr-S-S-iPr and Ph-S-S-Ph leads to highly selective formation of CdS tetrapods. These reactions cleanly and reproducibly produce anisotropic CdS structures (only rods or tetrapods), without the need for any of the widespread and commonly used size- and/or shape-selective purification protocols. In addition, pod branching depends on the ratio of precursors used.
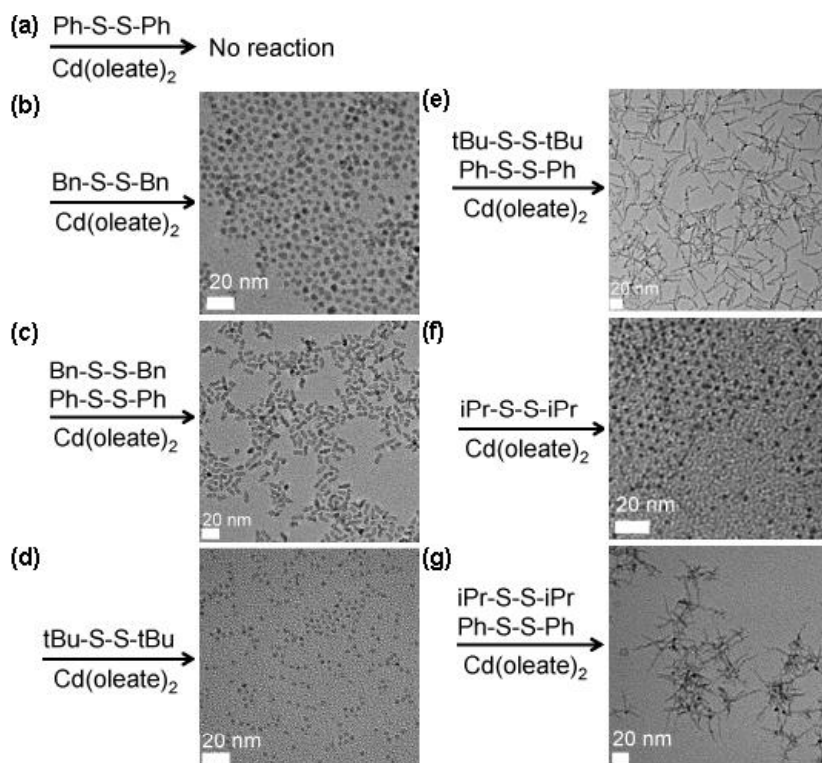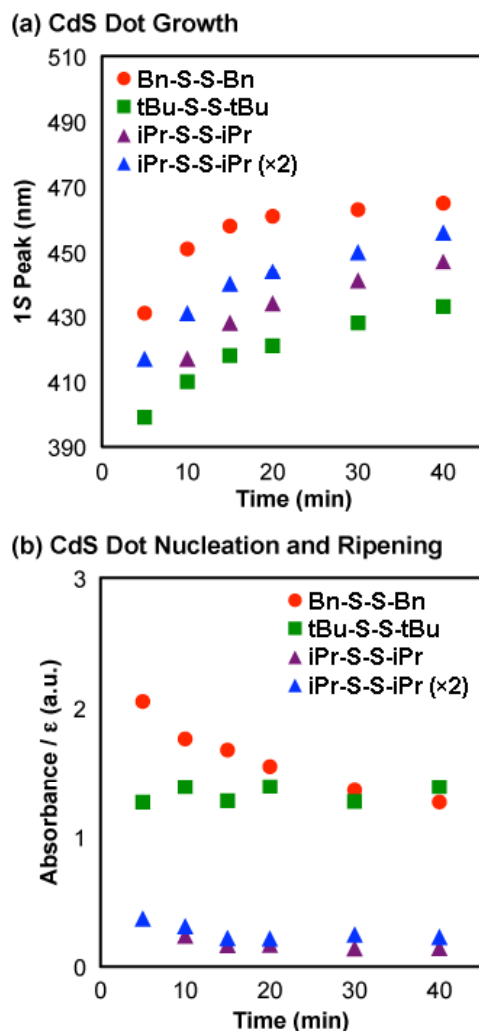

Figure 4. Under identical conditions (0.40 mol Cd(oleate)$_2$, 1.1 equiv. R-S-S-R, 20 equiv. oleic acid, 20

equiv. oleylamine, 4.6 mL ODE, 250 °C): Ph-S-S-Ph is unreactive (a); Bn-S-S-Bn produces CdS dots while a 1:1 mixture of Bn-S-S-Bn and Ph-S-S-Ph produces CdS rods (c); tBu-S-S-tBu produces CdS dots (d) while a 1:1 mixture of tBu-S-S-tBu and Ph-S-S-Ph produces CdS tetrapods (e); iPr-S-S-iPr produces CdS dots (f) while a 1:1 mixture of iPr-S-S-iPr and Ph-S-S-Ph produces CdS tetrapods (g).

These results strongly support, and are consistent with our hypothesis above that *in situ* generated thiol radicals (R-S• radicals) serve as efficient surface-passivating ligands, increasing the lifetime of small CdS nuclei long enough to allow for slow (and selective) heterogeneous (epitaxial) growth of new CdS (pods). Dichalcogenide precursors with intermediate S-S and C-S bond strengths such as Et-S-S-Et and Me-S-S-Me are good at generating R-S• radicals, and they are also mild (slowly releasing) sources of S; therefore, these precursors are ideal for selective anisotropic growth (Figure 1e, f). With a much weaker S-S bond, the ability to generate R-S• radicals is even higher for Ph-S-S-Ph, but this precursor has a prohibitively strong C-S bond and is unable to serve as a source of S (Figure 1g and 4a). However, when mixed with other precursors that are good S sources such as Bn-S-S-Bn, tBu-S-S-tBu or iPr-S-S-iPr, Ph-S-S-Ph allows the generation of anisotropic structures such as rods and tetrapods where usually only dots would form (Figure 4c, e, g). In these mixed precursor experiments, the degree of anisotropy is a direct result of an exquisite interplay between the ability of Ph-S-S-Ph to give off surface-stabilizing R-S• radicals, and the chemical reactivity of a second precursor (namely, the latter's ability to give off S as measured by its relative C-S BDE).

Other effects of dichalcogenide reactivity: Understanding nucleation, growth and ripening. Our calculations and experimental observations also help understand the relative rates of nucleation, growth and ripening of CdS nanocrystals made with different dichalcogenides (Figure 5). As judged from the position of the first *1S* absorption peak (Figure 5a),[69-72] Bn-S-S-Bn (C-S BDE 48.50 kcal/mol) reacts with $Cd(oleate)_2$ to form larger CdS nanocrystals than tBu-S-S-tBu (C-S BDE 52.81 kcal/mol) or iPr-S-S-iPr (C-S BDE 55.45 kcal/mol). Interestingly,

increasing the initial dichalcogenide concentration also results in an increase in the size of the CdS nanocrystals (iPr-S-S-iPr (×2) *vs.* iPr-S-S-iPr in Figure 5a). These observations suggest that *the rate of nanocrystal growth* (heterogeneous nucleation of new CdS material epitaxially on existing CdS particles)[73] *is directly dependent on dichalcogenide reactivity and concentration.* Dividing the CdS particle size (derived from the position of the *1S* peak) by its size-specific absorption coefficient or "cross section" (ε) is proportional to the number of CdS particles present in the reaction at any given time (Figure 5b).[68-71] Interestingly, reaction of Cd(oleate)$_2$ with Bn-S-S-Bn (C-S BDE 48.50 kcal/mol) initially forms *ca.* twice as many initial nuclei as tBu-S-S-tBu (C-S BDE 52.81 kcal/mol) and *ca.* seven times as many nuclei as iPr-S-S-iPr (C-S BDE 55.45 kcal/mol) (short reaction times ≤ 5 min, Figure 5b). However, increasing the initial dichalcogenide concentration does not affect the number of initially formed CdS nuclei (iPr-S-S-iPr (×2) *vs.* iPr-S-S-iPr in Figure 5b). Therefore, *the rate of nanocrystal nucleation* (homogeneous nucleation of new CdS nuclei) *is extremely sensitive to, and directly dependent on, the reactivity of the dichalcogenide precursor used, but not its concentration.* Once the initial nucleation event has occurred, the change in the number of CdS particles over time (*i.e.*, *ripening*) does not appear to be directly affected by precursor reactivity, but rather appears to be a simple consequence of the initial CdS particle size (Figure 5b).

Figure 5. Time evolution of particle size (growth, a) and number of nuclei and ripening (b) of CdS nanocrystals produced with different dialkyl dichalcogenide precursors under similar reaction conditions (0.40 mol Cd(oleate)$_2$, 1.1 equiv. R-S-S-R, 20 equiv. oleic acid, 20 equiv. oleylamine, 4.6 mL ODE, 250 °C).

Comparing diselenide with disulfide precursors. The diselenide precursors reacted more quickly than the analogous disulfide precursors. We previously observed similar behavior in trialkylphosphine-chalcogenide precursors (R$_3$P=E, E = Se vs. S),[14-16] and we attribute this difference to the fact that Se forms weaker and longer (C-E and E-E) bonds compared to S (see the Appendix). Et-Se-Se-Et has weak C-Se bonds (52.01 kcal/mol) and reacts quickly with Cd(oleate)$_2$ to form CdSe quantum dots in < 2 min; these become non-quantum confined CdSe nanocrystals with a particle size of 6.6 nm $\pm$ 0.6 nm after 10 min (Figure 6a). For reference, the

Bohr radius reported for CdSe is *ca.* 5.4 nm.[42] Me-Se-Se-Me has stronger C-Se bonds (53.76 kcal/mol) and reacts more slowly and selectively with Cd(oleate)$_2$ to form CdSe multipods; these show significant clustering after 5 min (Figure 6b). Ph-Se-Se-Ph has even stronger C-Se bonds (64.44 kcal/mol) and barely reacts with Cd(oleate)$_2$ to form very small CdSe quantum dots (Figure 6c). We attribute the difference between Ph-S-S-Ph (unreactive) and Ph-Se-Se-Ph (marginally reactive) to the difference in C-E bond dissociation energies between these two precursors (C-S BDE 69.75 kcal/mol in Ph-S-S-Ph *vs.* C-Se BDE 64.44 kcal/mol in Ph-Se-Se-Ph) (Table 1). Thus, although more reactive, the diselenide (R-Se-Se-R) precursors show similar reactivity patterns as those observed for the disulfide (R-S-S-R) precursors above.
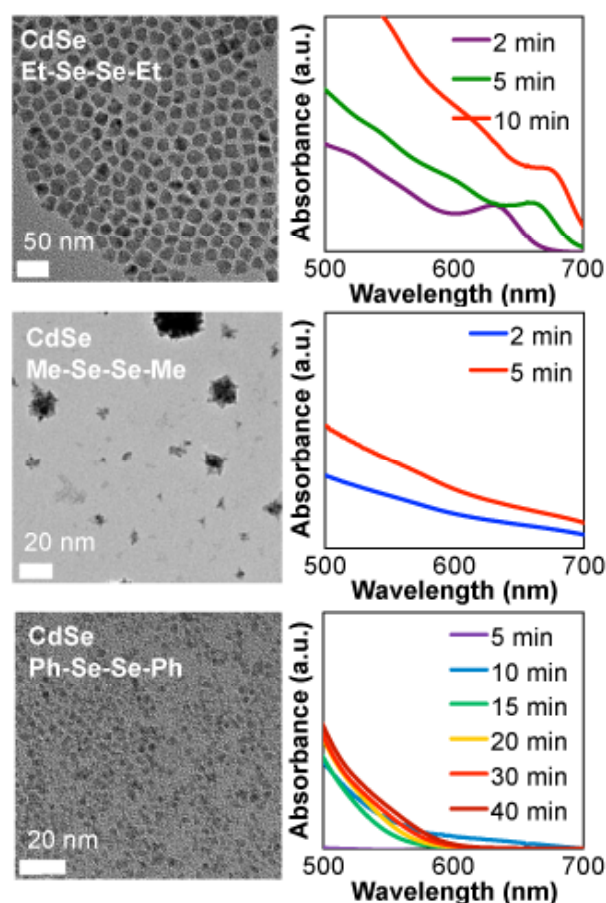
Figure 6. Representative TEM images (left panel) and time evolution of UV-Vis absorption spectra (right panel) of CdS nanocrystals obtained with (a) diethyl (10 min), (b) dimethyl (5 min), and (c) diphenyl

disulfide (40 min) precursors under identical conditions (0.40 mol Cd(oleate)$_2$, 1.1 equiv. R-Se-Se-R, 20 equiv. oleic acid, 20 equiv. oleylamine, 4.6 mL ODE, 250 °C).

Conclusions

By studying a variety of commercially available dichalcogenides and the outcome of their solution-phase reaction with a cadmium-oleate complex under identical conditions, we have demonstrated that the formation and degree of anisotropy for different nanocrystalline products can be traced back to the precise molecular structure, bonding energetics, and chemical reactivity of the different dichalcogenides used. Using DFT, we showed that the main factor that determines overall dichalcogenide precursor reactivity is the carbon-chalcogen (C-S or C-Se) bond dissociation energy, while the chalcogen-chalcogen (S-S or Se-Se) bond dissociation energy remains more or less constant across most of dichalcogenides (disulfides or diselenides). The only exception to this trend are diphenyl dichalcogenides, which exhibit the weakest chalcogen-chalcogen bonds and the strongest carbon-chalcogen bonds due to strong π orbital interactions between the first carbon atom in the phenyl ring and the adjacent chalcogen atom. The presence of this strong C-S bonding interaction causes Ph-S-S-Ph to appear unreactive when used alone. Conversely, Allyl-S-S-Allyl has the weakest C-S bond, and reacts quickly to produce large aggregated CdS nanocrystals. Similar trends in bond dissociation energies and reactivity hold for the diselenide precursors, although their longer and weaker bonds lead to faster reactivity and more aggregated particles compared to disulfide precursors.

To understand the formation of anisotropic structures from disulfides containing roughly equal C-S and S-S bond strengths (Et-S-S-Et or Me-S-S-Me), we carried out reactions employing 1:1 mixtures of a thiol radical source (Ph-S-S-Ph) and a sulfur monomer source (Bn-S-S-Bn, tBu-S-S-tBu, or iPr-S-S-iPr). Ph-S-S-Ph by itself yielded no nanocrystalline products and the sulfur sources alone yielded only spherical nanocrystals. However the mixed precursor

experiments resulted in the exclusive formation of anisotropic structures (rods or tetrapods). Our present hypothesis is that the disulfide bond of Ph-S-S-Ph homolyzes to produce PhS• radicals which passivate and stabilize small zinc blende CdS nuclei. The cadmium and the second sulfur (Bn-S-S-Bn, tBu-S-S-tBu, or iPr-S-S-iPr) precursors then slowly react to selectively grow wurtzite arms on the {111} facets of the zinc blende cores. Our computations shed light on the relative rates of nucleation, growth and ripening of CdS nanocrystals observed experimentally. The rates of CdS nanocrystal nucleation and growth are directly dependent on dichalcogenide chemical reactivity, or inversely proportional to C-S bond strength. Increasing the initial dichalcogenide concentration increases CdS nanocrystal size, but does not affect the number of CdS particles already present after the initial nucleation stage. This implies that the observed sizes and morphology are not a function of precursor concentration, but only its characteristic reactivity. By applying our understanding the chemistry of precursors, we may begin to rationalize and predict desirable nanocrystalline properties such as morphology, composition and optoelectronic properties. This "bottom-up" approach to controllable and predictable nanocrystal synthesis allows for the preparation of a diverse array of morphologies based on fundamental, tangible and measurable molecular properties such as bond energies. We believe this and similar efforts will lead to the reliable syntheses of colloidal nanomaterials for customized applications.

Acknowledgments

References

[1] Norako, M. E.; Franzman, M. A.; Brutchey, R. L. *Chem. Mater.* **2009**, *21*, 4299–4304.

[2] Norako, M. E.; Brutchey, R. L. *Chem. Mater.* **2010**, *22*, 1613–1615.

[3] Norako, M. E.; Greaney, M. J.; Brutchey, R. L. *J. Am. Chem. Soc.* **2012**, *134*, 23–26.

[4] Franzman, M. A.; Brutchey, R. L. *Chem. Mater.* **2009**, *21*, 1790–1792.

[5] Buckley, J. J.; Rabuffetti, F. A.; Hinton, H. L.; Brutchey, R. L. *Chem. Mater.* **2012**, *24*, 3514−3516.

[6] Li, W.; Shavel, A.; Guzman, R.; Rubio-Garcia, J.; Flox, C.; Fan, J.; Cadavid, D.; Ibáñez, M.; Arbiol, J.; Morante, J. R.; Cabot, A. *Chem. Commun.* **2011**, *47*, 10332–10334.

[7] Franzman, M. A.; Schlenker, C. W.; Thompson, M. E.; Brutchey, R. L. *J. Am. Chem. Soc.* **2010**, *132*, 4060–4061.

[8] Webber, D. H.; Brutchey, R. L. *Inorg. Chem.* **2011**, *50*, 723–725.

[9] Webber, D. H.; Brutchey, R. L. *Chem. Commun.* **2009**, 5701–5703.

[10] Kang, S.-K.; Jia, L.; Li, X.; Yin, Y.; Li, L.; Guo, Y.-G.; Mu, J. *Colloids Surf. A: Phys. Eng. Aspects* **2012**, *406*, 1–5.

[11] Wang, J.-J.; Xue, D.-J.; Guo, Y.-G.; Hu, J.-S.; Wan, L.-J. *J. Am. Chem. Soc.* **2011**, *133*, 18558–18561.

[12] Wang, J.-J.; Wang, Y.-Q.; Cao, F.-F.; Guo, G.-Y.; Wan, L.-J. *J. Am. Chem. Soc.* **2010**, *132*, 12218–12221.

[13] Schlecht, S.; Budde, M.; Kienle, L. *Inorg. Chem.* **2002**, *41*, 6001−6005.

[14] Ruberu, T. P. A.; Vela, J. *ACS Nano* **2011**, *5*, 5775–5784.

[15] Alemseghed, M. G.; Ruberu, T. P. A.; Vela, J. *Chem. Mater.* **2011**, *23*, 3571–3579.

[16] Ruberu, T. P. A.; Albright, H. R.; Callis, B.; Ward, B.; Cisneros, J.; Fan, H.-J.; Vela, J. *ACS Nano* **2012**, *6*, 5348–5359.

[17] Ko, W. Y. L.; Bagaria, H. G.; Asokan, S.; Lina, K. J.; Wong, M. S. *J. Mater. Chem.* **2010**, *20*, 2474–2478.

[18] Wang, W.; Geng, Y.; Qian, Y.; Ji, M.; Liu, X. *Adv. Mater.* **1998**, *10*, 1479–1481.

[19] Xi, L.; Chua, K. H.; Zhao, Y.; Zhang, J.; Xiong, Q.; Lam, Y. M. *RSC Adv.* **2012**, *2*, 5243–5253.

[20] Shen, H.; Wang, H.; Chen, X.;Niu, J. Z.; Xu, W.; Li, X. M.; Jiang, X.-D.; Du, Z.; Li, L. S. *Chem. Mater.* **2010**, *22*, 4756–4761.

[21] Pang, Q.; Zhao, L.; Cai, Y.; Nguyen, D. P.; Regnault, N.; Wang, N.; Yang, S.; Ge, W.; Ferreira, R.; Bastard, G.; Wang, J. *Chem. Mater.* **2005**, *17*, 5263–5267.

[22] Yang, J.; Xue, C.; Yu,S. H.; Zeng, J. H.; Qian, Y. T. *Angew. Chem. Int. Ed.* **2002**, *41*, 4697–4700.

[23] Govan, J. E.; Jan, E.; Qurejeta, A.; Kotov, N. A.; Gun'ko, Y. K. *Chem. Commun.* **2010**, *46*, 6072–6074.

[24] Asokan, S.; Krueger, K. M.; Colvin, V. L.; Wong, M. S. *Small* **2007**, *3*, 1164−1169.

[25] Manna, L.; Scher, E. C.; Alivisatos, A. P. *J. Am. Chem. Soc.* **2000**, *122*, 12700−12706.

[26] Wang, F.; Buhro, W. E. *J. Am. Chem. Soc.* **2012**, *134*, 5369−5380.

[27] Liu, H.; Tao, H.; Yang, T.; Kong, L.; Qin, D.; Chen, J. *Nanotechnology* **2011**, *22*, 045604.

[28] Huang, J.; Kovalenko, M. V.; Talapin, D. V. *J. Am. Chem. Soc.* **2010**, *132*, 15866–15868.

[29] Fiore, A.; Mastria, R.; Lupo, M. G.; Lanzani, G.; Giannini, C.; Carlino, E.; Morello, G.; De Giorgi, M.; Li, Y.; Cingolani, R.; Manna, L. *J. Am. Chem. Soc.* **2009**, *131*, 2274−2282.

[30] Talapin, D. V.; Nelson, J. H.; Shevchenko, E. V.; Aloni, S.; Sadtler, B.; Alivisatos, A. P. *Nano Lett*. **2007**, *7*, 2951–2959.

[31] Peng, X.; Manna, L.; Yang, W.; Wickham, J.; Scher, E.; Kadavanich, A.; Alivisatos, A. P. *Nature* **2000**, *404*, 59–61.

[32] Peng, Z. A.; Peng, X. *J. Am. Chem. Soc.* **2002**, *124*, 3343−3353.

[33] Xie, R.; Kolb, U.; Basche, T. *Small* **2006**, *2*, 1454−1457.

[34] Lim, J.; Bae, W. K.; Park, K. U.; Zur Borg, L.; Zentel, R.; Lee, S.; Char, K. *Chem. Mater.* **2013**, *25*, 1443–1449.
[35] Zhang, W.; Jin, C.; Yang, Y.; Zhong, X. *Inorg. Chem.* **2012**, *51*, 531−535.

[36] Schmidt, M. W.; Baldridge, K. K.; Boatz, J. A.; Elbert, S. T.; Gordon, M. S.; Jensen, J. S.; Koseki, S.; Matsunaga, N.; Nguyen, K. A.; Su, S.; Windus, T. L.; Dupuis, M.; Montgomery, J. A. *J. Comput. Chem.* **1993**, *14*, 1347−1363.

[37] Gordon, M. S.; Schmidt, M. W. Advances in Electronic Structure Theory: GAMESS a Decade Later. In *Theory and Applications of Computational Chemistry: The First Forty Years*; Dykstra, C. E., Frenking, G., Kim, K. S., Scuseria, G. E., Eds.; Elsevier Science: Amsterdam, 2005; p 1167.

[38] Hehre, W. J.; Ditchfield, R.; Pople, J. A. *J. Chem. Phys.* **1972**, *56*, 2257–2261.

[39] Boese, A.D.; Martin, J.M.L. *J. Chem. Phys.* **2004**, *121*, 3405–3416.

[40] Denk, M. K. *Eur. J. Inorg. Chem.* **2009**, 1358–1368.

[41] Bode, B. M.; Gordon, M. S. *J. Mol. Graphics Model.* **1998**, *16*, 133.

[42] Ditchfield, R.; Hehre, W. J.; Pople, J. A. *J. Chem. Phys.* **1971**, *54*, 724–728.

[43] Krishnan, R.; Binkley, J. S.; Seeger, R.; Pople, J. A. *J. Chem. Phys.* **1980**, *72*, 650–654.

[44] Mitin, A. V.; Baker, J.; Pulay, P. *J. Chem. Phys.* **2003**, *118*, 7775–7782.

[45] Roothaan, C. C. J. *Rev. Mod. Phys.* **1951**, *23*, 69–89.

[46] Lutich, A. A.; Mauser, C.; Da Como, E.; Huang, J.; Vaneski, A.; Talapin, D. V.; Rogach, A. L.; Feldmann, J. *Nano Lett.* **2010**, *10*, 4646–4650.

[47] Choi, C. L.; Li, H.; Olson, A. C. K.; Jain, P. K.; Sivasankar, S.; Alivisatos, A. P. *Nano Lett.* **2011**, *11*, 2358–2362.

[48] Lee, D. C.; Robel, I.; Pietryga, J. M.; Klimov, V. I. *J. Am. Chem. Soc.* **2010**, *132*, 9960–9962.

[49] Bealing, C. R.; Baumgardner, W. J.; Choi, J. J.; Hanrath, T.; Hennig, R. G. *ACS Nano* **2012**, *6*, 2118–2127.

[50] Kumar, S.; Nann, T. *Small* **2006**, *2*, 316–329.

[51] Manna, L.; Milliron, D. J.; Meisel, A.; Scher, E. C.; Alivisatos, A. P. *Nature Mater.* **2003**, *2*, 382–385.

[52] Nourbakhsh, S.; Liao, C. L.; Ng, Y. G. *J. Chem. Phys.* **1990**, *92*, 6587–6593.

[53] McMillen, D. F.; Golden, D. M. *Ann. Rev. Phys. Chem.* **1982**, *33*, 493–532.

[54] Luo, Y. R. *Comprehensive Handbook of Chemical Bond Energies*, CRC Press, Boca Raton, FL, 2007.

[55] Benson, S. W. *Chem. Rev.* **1978**, *78*, 23–35.

56 Płaza, S.; Gruziński, R. *Wear* **1996**, *194*, 212–218.

57 Mortimer, C. T.; Waterhouse, J. *J. Chem. Thermodynamics* **1980**, *12*, 961–965.

58 Arshadi, M. R.; Shabrang, M. *J. Chem. Soc. Perkin Trans. 2* **1973**, *2*, 1732–1734.

59 Benassi, R.; Taddei, F. *J. Comput. Chem.* **2000**, *21*, 1405–1418.

60 Zou, L.-F.; Fu, Y.; Shen, K.; Guo, Q.-X. *THEOCHEM* **2007**, *807*, 87–92.

61 Zou, L.-F.; Shen, K.; Fu, Y.; Guo, Q.-X. *J. Phys. Org. Chem.* **2007**, *20*, 754–763.

62 Heverly-Coulson, G. S.; Boyd, R. J. *J. Phys. Chem. A* **2011**, *115*, 4827–4831.

63 Gámez, J. A.; Yáñez, M. *J. Chem. Theory Comp.* **2010**, *6*, 3102–3112.

64 Yoffe, A. D. *Adv. Phys.* **2002**, *51*, 799–890.

65 Wang, Y.; Herron, N. *J. Phys. Chem.* **1991**, *95*, 525–532.

66 Fonoberov, V. A.; Pokatilov, E. P.; Mateevici, A. *Phys. Rev. B* **2002**, *66*, 085310.

67 Smith, A. M.; Nie, S. *Acc. Chem. Res.* **2010**, *43*, 190−200.

68 Doll, J. D.; Hu, B.; Papadimitrakopoulos, F. *Chem. Mater.* **2012**, *24*, 4043−4050.

69 Yu, W. W.; Qu, L.; Guo, W.; Peng, X. *Chem. Mater.* **2003**, *15*, 2854–2860; **2004**, *16*, 560.

70 Jasieniak, J.; Smith, L.; van Embden, J.; Mulvaney, P.; Califano, M. *J. Phys. Chem. C* **2009**, *113*, 19468–19474.

71 Capek, R. K.; Moreels, I.; Lambert, K.; De Muynck, D.; Zhao, Q.; Van Tomme, A.; Vanhaecke, F.; Hens, Z. *J. Phys. Chem. C* **2010**, *114*, 6371–6376.

72 Leatherdale, C. A.; Woo, W.-K.; Mikulec, F. V.; Bawendi, M. G. *J. Phys. Chem. B* **2002**, *106*, 7619–7622.

73 Guo, Y.; Marchuk, K.; Sampat, S.; Abraham, R.; Fang, N.; Malko, A.; Vela, J. *J. Phys. Chem. C* **2012**, *116*, 2791–2800.

Appendix of supporting information

Table S1. Results of DFT calculations on dialkyl dichalcogenide bond energies and structural parameters.

Precursor(s) R-E-E-R	C-E BDE (kcal/mol)	E-E BDE (kcal/mol)	(C-E)-(E-E) (kcal/mol)	C-E bond length (Å)	E-E bond length (Å)	C-E-E angle (deg)	C-E-E-C dihedral angle (deg)
Disulfides (R-S-S-R)							
Allyl-S-S-Allyl	45.71	61.33	-15.62	1.8721	2.0926	102.75	89.28
Bn-S-S-Bn	48.50	62.45	-13.94	1.8732	2.0925	102.28	87.65
tBu-S-S-tBu	52.81	59.39	-6.59	1.8900	2.0961	105.68	110.88
iPr-S-S-iPr	55.45	59.69	-4.24	1.8744	2.0968	104.43	111.51
Et-S-S-Et	58.13	59.48	-1.35	1.8606	2.0912	102.75	86.37
Me-S-S-Me	59.03	58.04	0.99	1.8494	2.0930	102.43	84.93
Ph-S-S-Ph	69.75	45.65	24.11	1.8085	2.1144	103.44	83.15
Diselenides (R-Se-Se-R)							
Allyl-Se-Se-Allyl	40.37	52.82	-12.45	1.9897	2.3359	101.31	91.24
Bn-Se-Se-Bn	43.26	54.43	-11.16	1.9878	2.3346	100.15	84.67
tBu-Se-Se-tBu	48.14	53.96	-5.83	1.9891	2.3380	103.75	107.52
iPr-Se-Se-iPr	49.57	53.49	-3.92	2.0073	2.3364	102.44	107.02
Et-Se-Se-Et	52.01	56.41	-4.40	1.9762	2.3341	100.10	88.49
Me-Se-Se-Me	53.76	51.94	1.82	1.9641	2.3351	100.26	86.82
Ph-Se-Se-Ph	64.44	43.63	20.80	1.9238	2.3582	100.97	82.74

Additional computational details

These computations consider the homolytic dissociation of disulfides and diselenides to give radical species, as shown in scheme S1. This method is consistent with the definition of bond dissociation energy, as well as previously reported calculations.[1] That said, in some cases it is preferable to consider isodesmic[2] (similar bond types broken and formed) or isogyric[3] (products and reactants have the same spin multiplicity) reactions in order to correct for errors

arising due to the change in spin multiplicity from reactants to products. In this case, the spin multiplicity changes from singlet for the reactants to doublet for the product radicals.

a. $\overset{R}{\underset{R}{E-E}} \longrightarrow 2\,R-E\cdot$

b. $\overset{R}{\underset{R}{E-E}} \longrightarrow \overset{R}{E-E}\cdot + \cdot R$
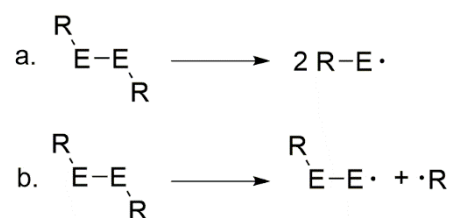
Scheme S1. Bond homolysis reactions for (a) E-E homolysis and (b) R-E homolysis.

The accuracy of the calculations is also dependent on the basis sets employed. The highest precision possible is considered to be the complete basis set (CBS) limit, where the basis set for each atom is composed of an infinite set of functions. This approach works well for simple disulfides[4] but requires vast computational resources for larger molecules and atoms with increasing numbers of electrons. This study uses the largest basis set that completed computations in a reasonable timeframe – 6-311G(d,p).

Computational methods other than DFT also provide higher precision at added computational cost. Most notable is Gaussian-3, a composite method for thermodynamic calculations. In the case of disulfide bond energies, certain DFT functionals such as BMK can provide similar accuracy with lower computational cost,[1] which is why this method was used in this study.

The computations described here consider gas phase molecules in vacuum. Solvent effects are known to influence bond dissociation energies.[5] As a first approximation, solvation effects could be modeled using PCM, the polarizable continuum model.[6] More accurate modeling of solvation effects would require either explicit modeling of radical-solvent molecule interaction or considering a statistical mechanics model.

References

[1] Denk, M. K. *Eur. J. Inorg. Chem.* **2009**, 1358–1368.

[2] Ibdah, A.; Espenson, J. A.; Jenks, W. S. *Inorg. Chem.* **2005**, *44*, 8426–8432.

[3] McDonough, J. E.; Mendiratta, A.; Curley, J. J.; Fortman, G. C.; Fantasia, S.; Cummins, C. C.; Rybak-Akimova, E. V.; Nolan, S. P.; Hoff, C. D. *Inorg. Chem.* **2008**, *47*, 2133–2141.

[4] Benassi, R.; Taddei, F. *J. Comput. Chem.* **2000**, *21*, 1405–1418.

[5] Borges dos Santos, R. M.; Costa Cabral, B. J.; Martinho Simões, J. A. *Pure Appl. Chem.* **2007**, *79*, 1369–1382.

[6] Miertuš, S.; Scrocco, E.; Tomasi, J. *Chem. Phys.* **1981**, *55*, 117–129.

CHAPTER 4

ASSESSING PHOSPHINE-CHALCOGEN BOND STRENGTHS FROM CALCULATIONS

Samuel R. Alvarado, Ian Shortt, Hua-Jun Fan, Javier Vela

Abstract

Phosphine chalcogenides are useful reagents for chalcogen atom transfer reactions and nanocrystal syntheses. Understanding the strength and electronic structure of these bonds is key to optimizing their reactivity, but a limited number of experimental and computational studies probe these issues. Using density functional theory (DFT), we computationally screen multiple series of phosphine chalcogenide molecules with a variety of moieties attached to the phosphorus to control the strength of the phosphorus-chalcogen bond. DFT provides valuable data on these compounds including homolytic bond dissociation energies, bond order, Löwdin charge on phosphorus and chalcogen atoms, and molecular geometries. Experimentally monitoring the ^{31}P and ^{77}Se NMR chemical shifts and published Hammet constants provide the estimation of the relative magnitude of electronic shielding around these nuclei and confirms the computational results.

Introduction

Tertiary (trisubstituted) phosphine chalcogenides (R$_3$PE, where R = alkyl, aryl, amid, alkoxyl, and E = S, Se, Te) are molecular compounds useful in a variety of chemical transformations including chalcogen atom transfer reactions and chalcogenide nanocrystal synthesis. In comparison to the unsupported elemental chalcogens, the substituents (R) on the

phosphine chalcogenide can be used to fine-tune the solubility and reactivity of the phosphorus-chalcogen (PE) moiety in these compounds.[1]

In atom transfer reactions, phosphine chalcogenides donate sulfur, selenium or tellurium in a bimolecular fashion.[2,3] Current evidence indicates that the rate of atom transfer is dependent on the relative basicity of the pnictogen center (P, As or Sb). This transfer can occur between a phosphine chalcogenide and another P, As or Sb atom.[4] Computations suggest that the transfer of S and Se atom among phosphines proceeds through chalcogen-philic attack by the pnictide nucleophile.[5] Phosphine sulfide-supported palladium complexes[6] as well as Cu(I) and Zn(II) catalysts[7] mediate this transformation. A synthetic application of this strategy is Se atom transfer from triphenylphosphine selenide to H-phosphonate diesters.[8] Similarly, tricyclohexylphosphine selenide and telluride donate a chalcogen atom to *N*-heterocyclic carbenes.[9]

Because of their desirable reactivity and solubility in low volatility (high boiling point) solvents, trialkyl phosphine chalcogenides have been popular chalcogen sources in nanocrystal preparations since the early 1990's.[10] Cleavage of the P—E bond is thought to occur by either redox chalcogen (E^0) atom transfer or acid-base chalcogenide (E^{2-}) transfer mechanisms.[11] The latter mechanism proceeds through a phosphine chalcogenide-metal activated complex, which decomposes into metal chalcogenide nuclei.[12] The mechanism of R_3PE decomposition has been studied for the synthesis of CdSe,[13–15] PbSe[16, 17] and ZnSe[18] nanocrystals. The electron donating and withdrawing effects of different phosphorous substituents have an effect on the mechanism of InP formation from triarylsilylphosphines.[19]

Studies on the electronic structure of R_3PE compounds and the reactive P—E bond are key to guiding their use as both atom transfer reagents and nanocrystal synthesis precursors. It is well established that heavier chalcogens form significantly weaker and longer bonds with

phosphorous. Calorimetric methods and atom transfer reactions have been used to measure the strength of P—E bonds experimentally.[20] Bond dissociation energies of phosphine sulfides spanned a range of 88-98 kcal/mol, while those of phosphine selenides ranged 67-75 kcal/mol.[21] Bonding in trialkyl phoosphine chalcogenides[22, 23] has also been studied computationally using Density Functional Theory (DFT)[24] and Atoms in Molecules (AIM).[25] Our group recently used DFT to estimate the P—E bond strengths of a selection of phosphine sulfide and selenide derivatives that are particularly useful in the preparation of colloidal semiconductor nanocrystals (quantum dots and rods).[26]

Here we greatly expand our investigation of P—S and P—Se bond dissociation energies (BDEs) using DFT methods. To understand how changing the electron density around the PE moiety influences the electronic structure and strength of the P—E bond, we closely examine different families of triarylphosphine chalcogenides containing substituents of varying inductive effects. We also investigate trialkyl-, and tris-perfluoroalkyl-, and Verkade type, caged-phosphine chalcogenides.[27] We anticipate that the results of this large computational screening will be generally applicable to a variety of problems and applications that make use of phosphine chalcogenides, including chalcogen atom transfer and nanomaterial synthesis reactions.

Computational and experimental details

Computations. All calculations were carried out using GAMESS[28, 29] (May 2013 version, revision 1) with density functional theory (DFT) and the Tao-Perdew-Staroverov-Scuseria (TPSS)[30, 31] functional. The accuracy of the new generation functional TPSS is known to match or exceed almost all prior functionals, including the popular hybrid functional B3LYP.[32] TPSS reproduces geometric properties at least as precisely as B3LYP, and can recognize relatively

weak interactions (such as agostic interactions) while B3LYP significantly underestimates them.[33] Since hydrogen atoms in the systems we modelled did not play significant roles, we used 6-311G* basis set[34] for all elements. By not applying polarization functions on H atoms far from the phosphorous center, the calculations are accelerated considerably without significantly degrading computational precision or accuracy.[35] All structures were fully optimized and Hessian calculations (frequency analyses) were performed to ensure a minimum was achieved with zero imaginary vibrational frequencies. Thermodynamic functions, including enthalpies, entropies and free energies, were calculated at 298.15 K and 1 atm. Results were visualized with MacMolPlt.[36]

Materials. Unless otherwise noted, all chemicals were used as received without further purification. Triphenylphosphine (99%) was purchased from Acros; sulfur (99.999%), selenium (99.999%), and tris(4-fluorophenyl)phosphine (98%) were purchased from Alfa Aesar; tris(pentafluorophenyl)phosphine (98%), tris(4-methoxyphenyl)phosphine (98%), and tris(2,4,6-trimethoxyphenyl)phosphine (98%) from Strem; toluene (99.9%), xylenes (99.9%) and chloroform (99.9%) from Fisher.

Characterization. ^{31}P NMR chemical shifts were referenced to 85% phosphoric acid, H_3PO_4 (δ 0 ppm). ^{77}Se NMR spectra were referenced to $Ph_3PSe/CDCl_3$ (δ 266.20 ppm *vs.* Me_2Se δ 0 ppm).

Synthesis. Triphenylphosphine selenide,[15] tris(4-fluorophenyl)phosphine sulfide, tris(4-fluorophenyl)phosphine selenide, tris(2,4,6-trimethoxyphenyl)phosphine sulfide, and tris(2,4,6-trimethoxyphenyl)phosphine selenide[37] were prepared as described previously. Tris(pentafluorophenyl)phosphine sulfide was prepared with a modified procedure;[38–40] briefly, tris(pentafluorophenyl)phosphine (50.3 mg, 0.0945 mmol and sulfur (2.8 mg, 0.0873 mmol)

were heated to reflux in xylenes for 4 days. Solvent was removed under vacuum. The crude was recrystallized from ethanol to give white needles (29.5 mg, 60.1%). ^{31}P NMR: -8.28 ppm; ^{19}F NMR: 131.54 ppm (*d*, 22.20 Hz), 143.53 ppm (*t*, 21.07 Hz), 157.84 ppm (*t*, 20.89 Hz).

Results and discussion

We have previously shown that bond dissociation energies (BDEs) can be good predictors of molecular precursor reactivity and selectivity. Specifically, we have been able to use computed BDEs of tertiary phosphine chalcogenides[26] and disubstituted dichalcogenides[41] to predictably fine-tune the composition, aspect ratio (of rods) and morphology (from dots to rods to tetrapods) of CdS-CdSe nanocrystals. In the case of tertiary phosphine chalcogenides, ten computed BDEs (five sulfides and five selenides) were correlated to experimental ^{31}P (and ^{77}Se NMR) data. Experiments showed that the relative rate of (homogeneous) CdE nucleation increased more dramatically than the rate of CdE growth (heterogeneous nucleation) with a decrease in precursor P—E bond energy (E = S or Se).[26]

In order to generalize this approach, we have used DFT (see Methods) to expand the range of computed tertiary phosphine chalcogenide BDEs (Chart 1). For simplicity, we categorize the specific chalcogenide compounds in our study into five families based on the type of tertiary phosphine that they are derived from: (a) Triaryl phosphines monosubstituted with electron donating or withdrawing groups (amino, -NH$_2$; methoxy, -OMe; fluoro, -F; carboxyl, -CO$_2$H; nitro, -NO$_2$); (b) triaryl phosphines substituted with one, two or three methoxy groups; (c) triaryl phosphines substituted with one, two or three fluorines; (d) trialkyl and triperfluoroalkyl phosphines; and, (e) caged (Verkade-type) tertiary phosphines (Chart 1).[27] In all cases, we optimized each compound's geometry, and modelled a homolytic dissociation of the P—E bond

by calculating the change in electronic energy after correcting for zero point energy (ΔE_{ZPE}), the change in enthalpy (ΔH) and the change in Gibbs free energy (ΔG) values corrected to 298.15 K for the release of sulfur or selenium atom from the corresponding phosphine chalcogenide (a full list of all of our results is available in the Appendix).
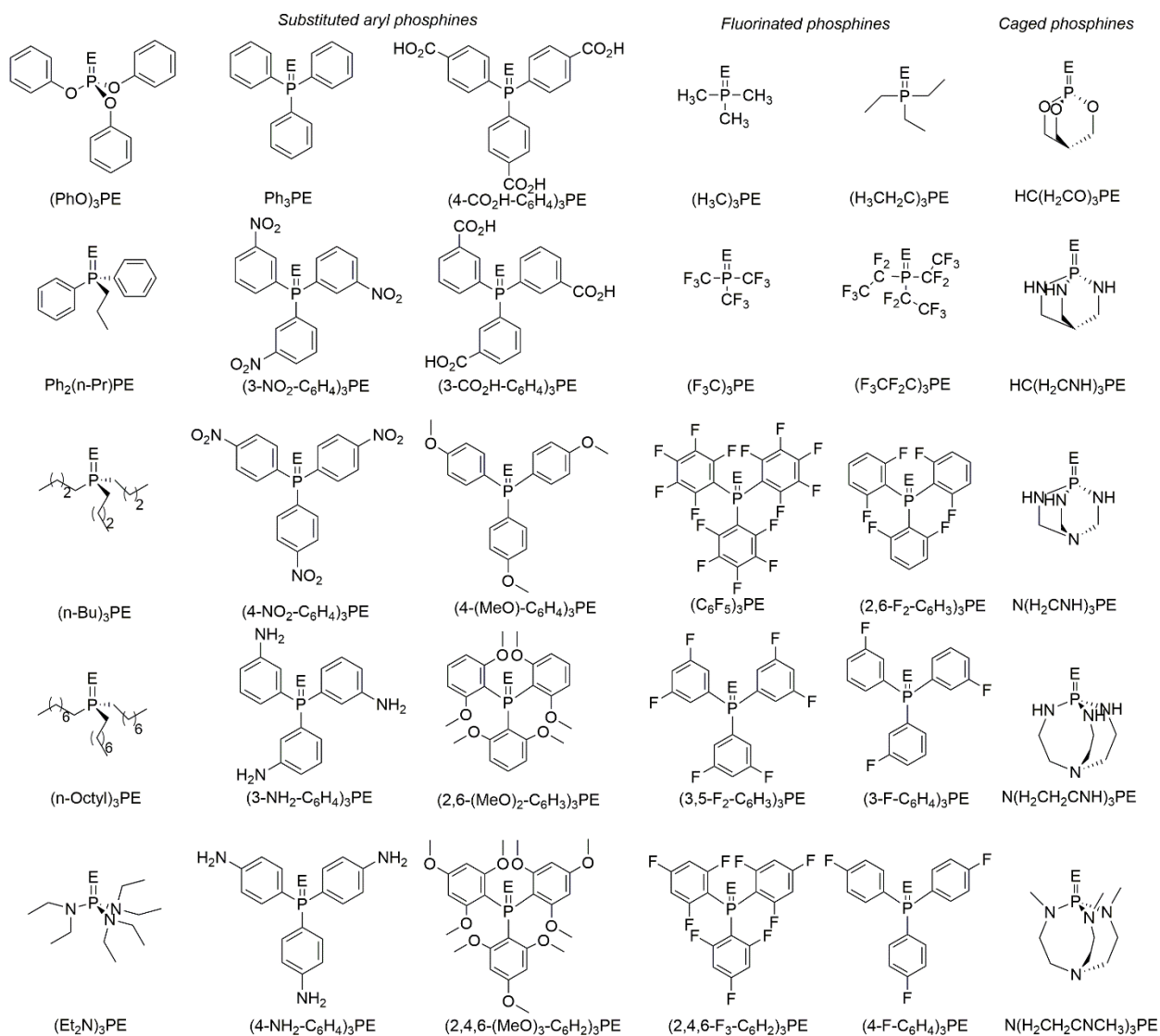
Chart 1. Tertiary (trisubstituted) phosphine chalcogenide (R₃PE, E = S or Se) compounds studied in this work. The compounds in the first column were calculated previously.[26]

General observations. Figure 1 shows the calculated BDE (ΔH) values for all the compounds studied. The heavier phosphine selenides exhibit significantly longer and weaker

bonds than the corresponding phosphine sulfides, due to the larger radius of selenium compared to sulfur. Comparing all the compounds we investigated, the P—S bond distance for all phosphine sulfides are shorter than the P—Se bond distances. BDEs in the P—S compounds are also stronger than those of P—Se compounds.
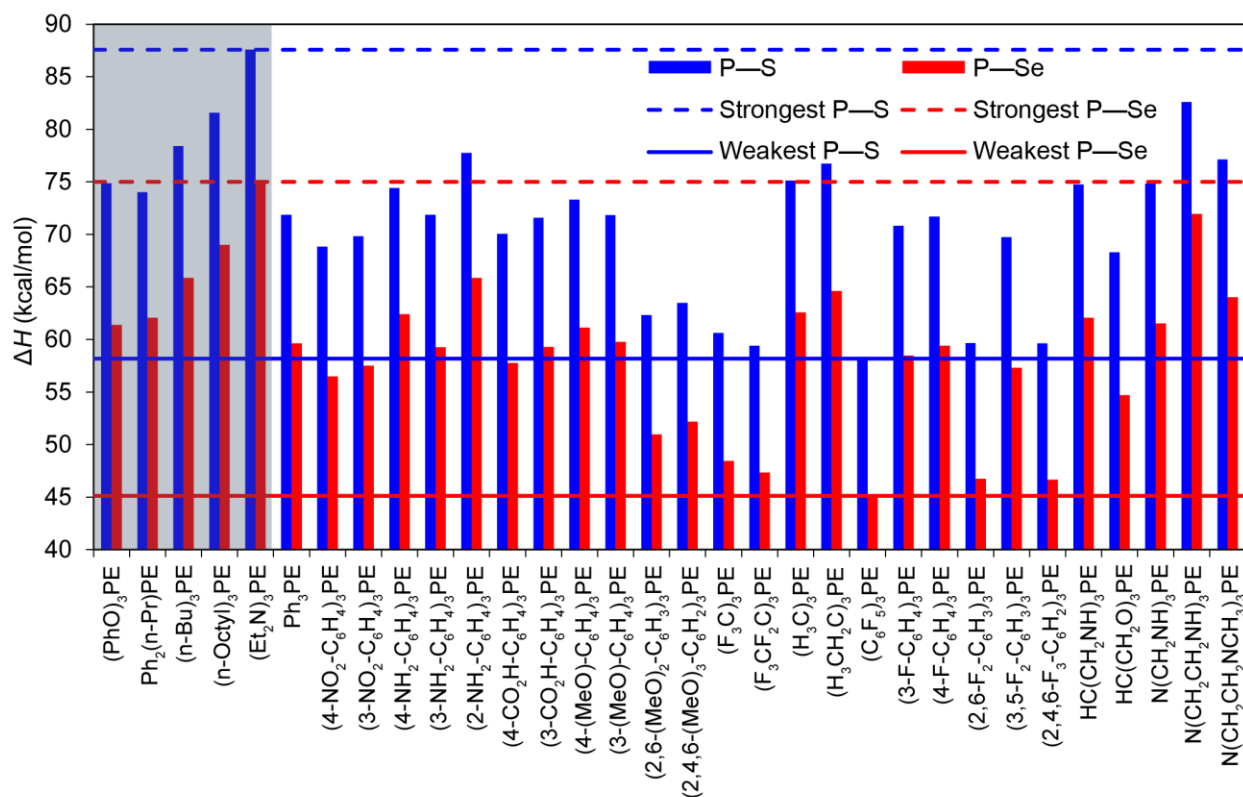
Figure 1. Calculated P—E bond dissociation enthalpies (ΔH) in tertiary phosphine sulfides (R$_3$PS) and selenides (R$_3$PSe).

Bond strength and bond distance. We then examined the correlation between bond strength and bond distance in each group of compounds (see above) to more closely investigate their relationship. In general, it appears that BDE actually increases with increasing P—E distance within a series of P—S or P—Se molecules. BDE increases with P—E distance in each family (figures 2a-2e), with some exceptions. In the case of the monosubstituted triphenylphosphine chalcogenides (figure 2a), we see a nearly linear increase in BDE across the

P—S and P—Se series individually. This trend can also be seen with methoxy substation on the phenyl rings (figure 2b), and fluorine substitution on the phenyl rings (figure 2c). Figures 2d and 2e examine linear alkyl and caged phosphine chalcogenides, respectively. In both cases, bond distance increases with bond strength, although not as linearly as in the aromatic phosphine chalcogenides.
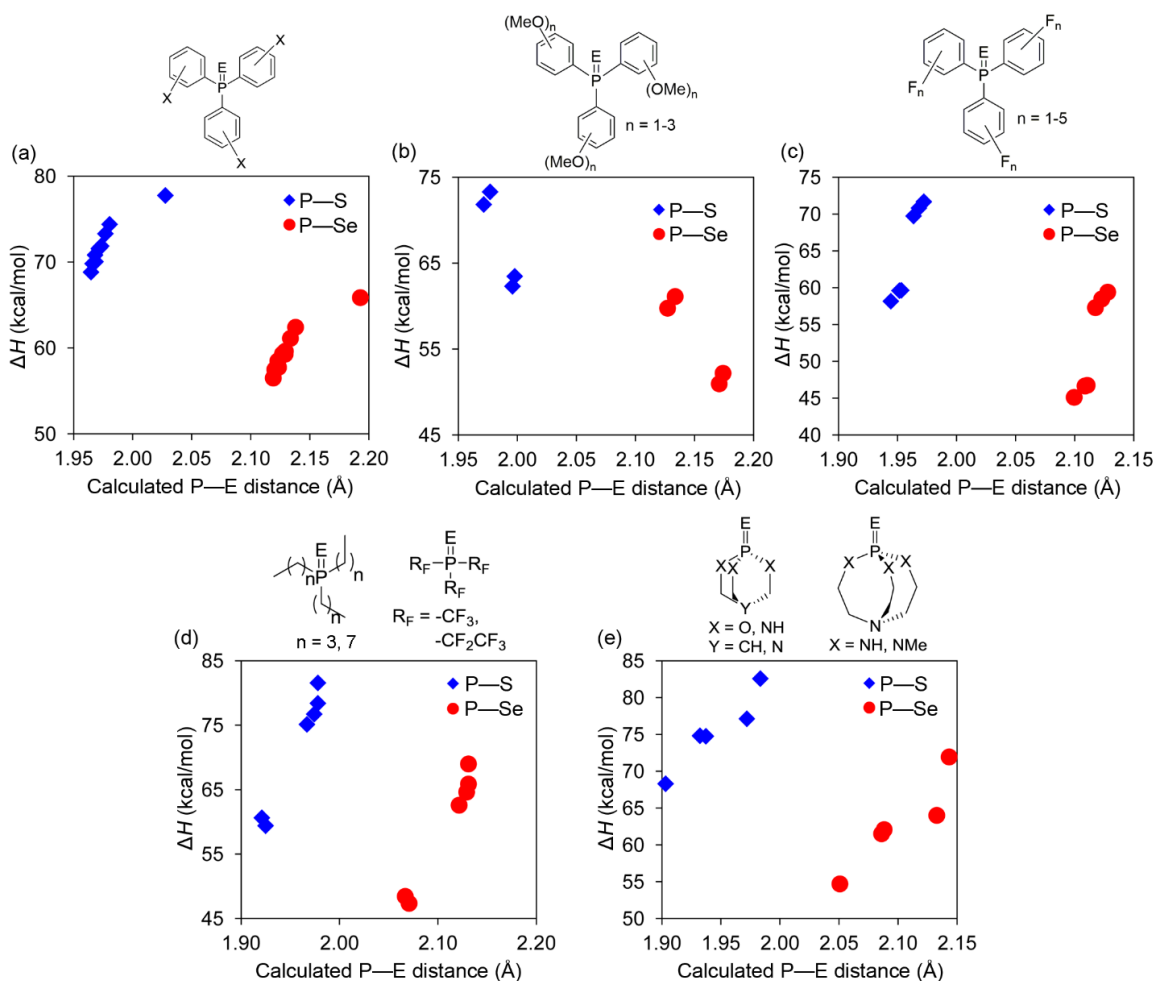
Figure 2. Plots of calculated ΔH of P—E bond dissociation and calculated P—E distance for (a) monosubstituted triarylphosphine chalcogenides, (b) fluorinated triarylphosphine chalcogenides, (c) methoxy-substitued triarylphosphine chalcogenides, (d) alkyl and perfluorinated phosphine chalcogenides and (e) cage-structured phosphine chalcogenides.

A general trend across each series, within a series of P—S or P—Se compounds, is that longer bonds are slightly stronger than shorter ones. While this is unexpected and counter-

intuitive to the notion that longer bonds are weaker, exceptions to this rule are well-documented in both computational and crystallographic studies, especially in compounds of main group elements. Examples include covalent compounds of tin[42] and its lighter analogues[43] as well as S-F bonds in SF_2 dimers.[44] A crystallographic study of phosphine adducts of open titanocenes also shows an inverse correlation with bond length and strength.[45]

We notice discontinuities in the bond length and bond strength trends in both the methoxy- and fluorine-substituted triarylphosphine chalcogenides (figure 2b and 2c). These outlying cases are compounds that feature substitution at the 2 position, adjacent to the P—E bond. Examples of molecules that feature this substitution are $(2\text{-}NH_2\text{-}C_6H_4)_3PE$ and $(2,6\text{-}MeO_2\text{-}C_6H_3)_3PE$. A possible explanation is that p orbitals from the adjacent functional groups may be interacting with the P—E bond itself. This interaction could potentially increase the P—E distance and weaken the bond disproportionately.

In order to further investigate this interaction, we visualized the highest occupied molecular orbitals (HOMO) of three moleules at a contour value of 0.01: Ph_3PS, $(2,6\text{-}MeO_2\text{-}Ph)_3PS$ and $(C_6F_5)_3PS$ (figures 3a-3c). In the latter two compounds, electron density from the neighboring substituents may be interacting with the P—E bond. Thus, while the methoxy groups should increase P—E electron density *via* inductive effects – the reported pK_a of $(2,4,6\text{-}MeO_3\text{-}Ph)_3P$ is 11.2[46] – their steric bulk may cause significant weakening of the P—E bond. The calculated average distances of these interactions in $(2,6\text{-}MeO_2\text{-}Ph)_3PS$, $(2,4,6\text{-}MeO_3\text{-}Ph)_3PS$, $(2,6\text{-}MeO_2\text{-}Ph)_3PSe$, and $(2,4,6\text{-}MeO_3\text{-}Ph)_3PSe$ are 3.15 Å, 3.16 Å, 3.23 Å and 3.24 Å. For reference, the van der Waals radii of S, Se and P are 1.80 Å, 1.90 Å and 1.80 Å, respectively.[47] Interestingly, in $(C_6F_5)_3PE$, one of the three aryl rings in these compounds is rotated nearly coplanar with the P—E bond. The distance of the nearest F-E interaction is 3.09 Å in $(C_6F_5)_3PS$

and 3.17 Å in $(C_6F_5)_3PSe$. The van der Waals radii of F, S and Se are 1.47 Å, 1.80 Å, and 1.90 Å, respectively. Interactions between S and F have been observed in crystal structures previously.[48, 49]
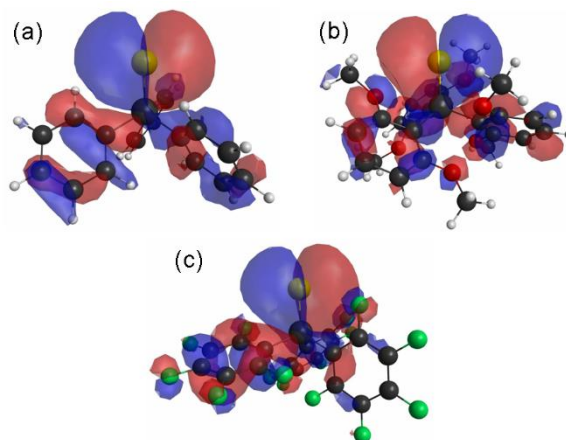

Figure 3. Highest occupied molecular orbitals (HOMO) for (a) Ph_3PS, (b) $(2,6-MeO_2-Ph)_3PS$ and (c) $(C_6F_5)_3PS$. All MOs are visualized at a contour value of 0.01.

Bond strength and Löwdin charges. To understand why longer bonds are slightly stronger within a given family of P—S or P—Se molecules, we examined the partial charge on the phosphorous and chalcogen atoms in each compound generated from a Mulliken population analysis[50–53] based on symmetrically orthogonalized orbitals.[54] Mulliken population analysis assigns a partial charge charge to each atom in the molecule. The Löwdin analysis improves on this method by preventing some physical impossibilities that Mulliken analysis can allow, such as calculating excessive charge on an atom, which in some cases could lead to more than two electrons sharing a single orbital.

Based on Löwdin analysis of the phosphorus atom in the compounds we studied, in general, it appears that the phosphorous in P—Se compounds is more positively charged than the phosphorous in analogous P—S compounds (figure 4a-4e). Looking at specific groups of compounds, in the monosubstituted (figure 4a), methoxy-substituted (figure 4b) and fluorine-substituted (figure 4c) triphenylphosphine chalogenides, building up positive charge on P

correlates approximately linearly with increasing BDE. The linear alkyl and fluoro alkyl (figure 4d), and cage-structured (figure 4e) phosphine chalcogenides also show that increased charge on phosphorous correlates to a greater BDE.
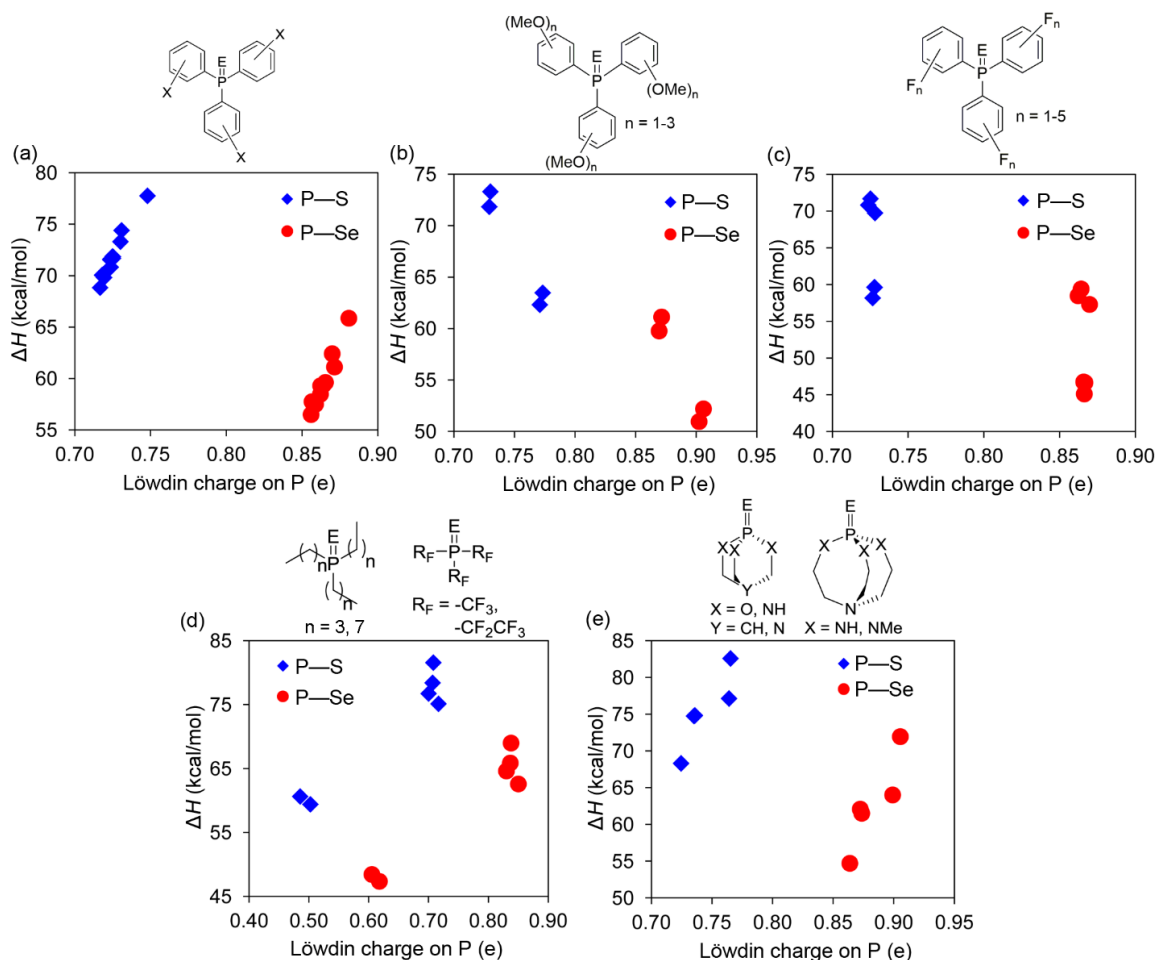
Figure 4. Plots of the Löwdin charge on phosphorus in (a) monosubstituted arylphosphine chalcogenides, (b) fluorinated arylphosphine chalocgenides, (c) methoxy-substituted arylphosphinechalcogenides, (d) alkyl and perfluoroalkyl phosphine chalcogenides, and (e) cage-structured phosphine chalcogenides.

Examining the charge on the chalcogen atom we generally see that P—Se compounds have more negative charge on the Se atom than the P—S compounds have on the S atom. In the monosubstituted triphenyl (figure 5a), methoxy-substituted triphenyl (figure 5b), and fluorine-substituted (figure 5c) phosphine chalcogenides, increasing negative charge on the S or Se atoms leads to an increase in the BDE. We see a similar trend in the trialkyl (figure 5d) and cage-

structured (figure 5e) phosphine sulfides and selenides. In cases of partial charge on both P and E atoms, the large discontinuity in the methoxy- and fluorine-substituted cases is due to substitution ortho to the P—E bond, which may be increasing the electron density on the chalcogen atom (see possible explanation above and figure 3). Additionally, in the alkyl phosphine chalcogenide family (figure 4d and 5d), perfluorinated alkyl compounds exhibit lower amounts of charge on both P and E, possibly due to the electronegative fluorines removing electron density from these atoms.
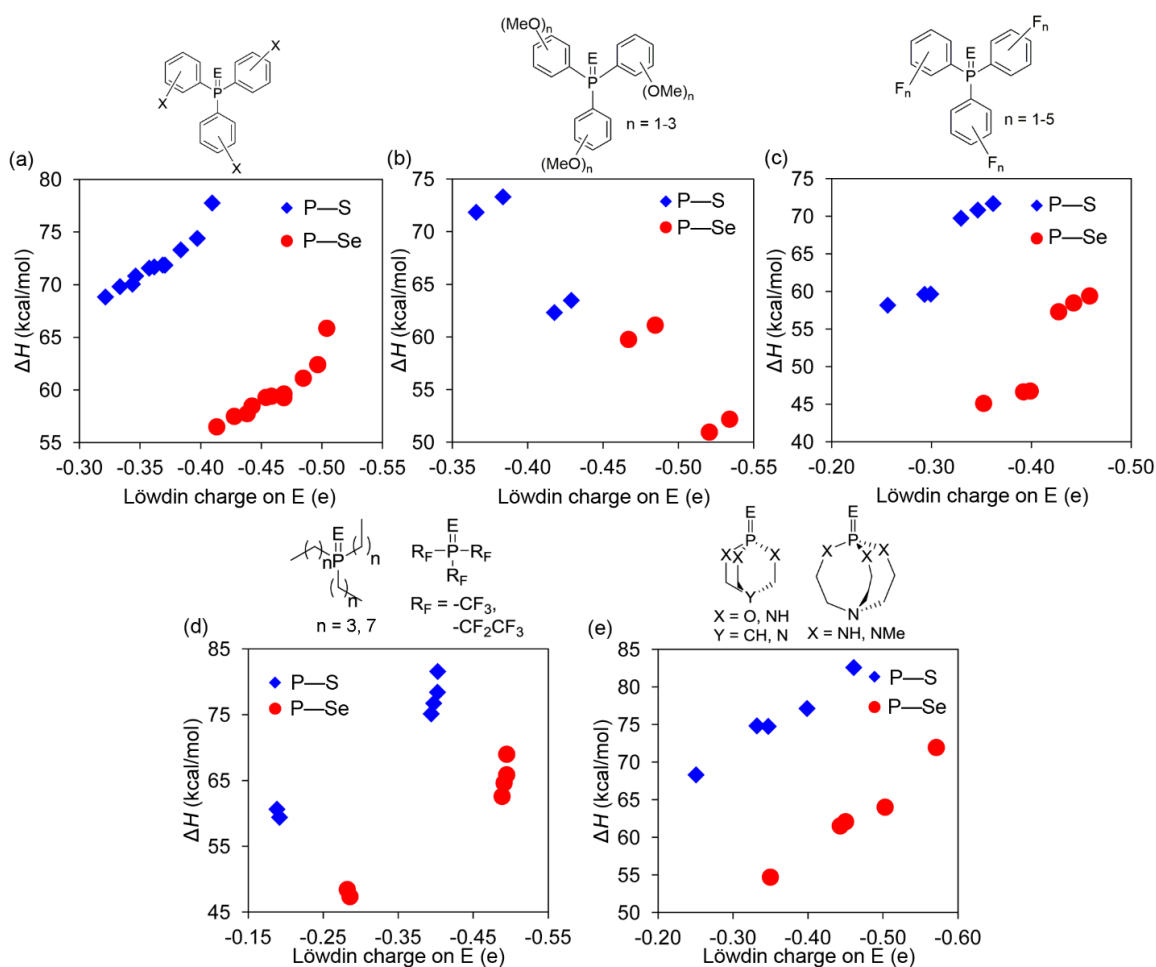
Figure 5. Plots of the Löwdin charge on phosphorus in (a) monosubstituted arylphosphine chalcogenides, (b) fluorinated arylphosphine chalocgenides, (c) methoxy-substituted arylphosphinechalcogenides, (d) alkyl and perfluoroalkyl phosphine chalcogenides, and (e) cage-structured phosphine chalcogenides.

In each series it appears that bonds with more negatively charged E atoms and more positively charged P atoms are stronger, which implies that bond strength increases with ionic character. Thus, we examined possible resonance structures of the P—E bond, which could be affected by accumulating charge on the phosphorus or chalcogen atoms (scheme 1). Structure I features a double bond between formally neutral atoms and structure II shows a single bond with a negatively charged chalcogen and a positively charged phosphorous. Structure III is a mixture of the two that contains some partial charge on both the phosphorus and the chalcogen which causes it to have a bond order between 1 and 2. Our results suggest that the P—E bond is composed of a mixture of covalent and ionic character, with more ionic bonds (greater positive partial charge on P and greater negative partial charge on S or Se) are slightly stronger than bonds with more covalent character (lower magnitude of partial charge on P, S and Se atoms).
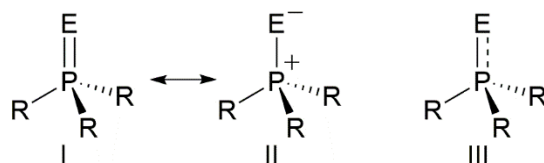
Scheme 1. Three resonance structures of the P—E bond: (I) a formal double bond, (II) a formal single bond with a phosphorous cation and a chalcogenide anion, and (III) a mixed structure of approximately 1.5 bonds.

Substituent effects. Hammett constants (σ_m and σ_p) are a useful parameter for quantifying the electron donating or withdrawing character of a substituent on an aromatic ring.[55] To see inductive effects influenced the strength of the P—E bond in substituted triphenylphosphine chalcogenides, we compared ΔH of bond dissociation against published Hammett constants of a variety functional groups: $-NH_2$, $-OMe$, $-H$, $-F$, $-CO_2H$, and $-F$. We considered the effect of only one functional group at the ortho or para position on each phenyl ring. In both P—S and P—Se compounds, Hammett constants show a linear correlation with BDE. As discussed previously, BDEs in the P—Se compounds are lower than those of the P—S compounds.

The 4-substituted triphenylphosphine chalcogenides (figure 6a) show a linear decrease in BDE with increasing Hammett constant; 3-substituted compounds (figure 6b) show a similar trend, although with a flatter slope. The smaller correlation here implies that substitution at the 3-position may have less effect on the strength of the P—E bond. Generally, substituents with more positive Hammett constants including $-NO_2$, $-CO_2H$ and $-F$ correspond to weaker BDEs while negative Hammett constants $-NH_2$ and $-OMe$ appear to give stronger BDEs.
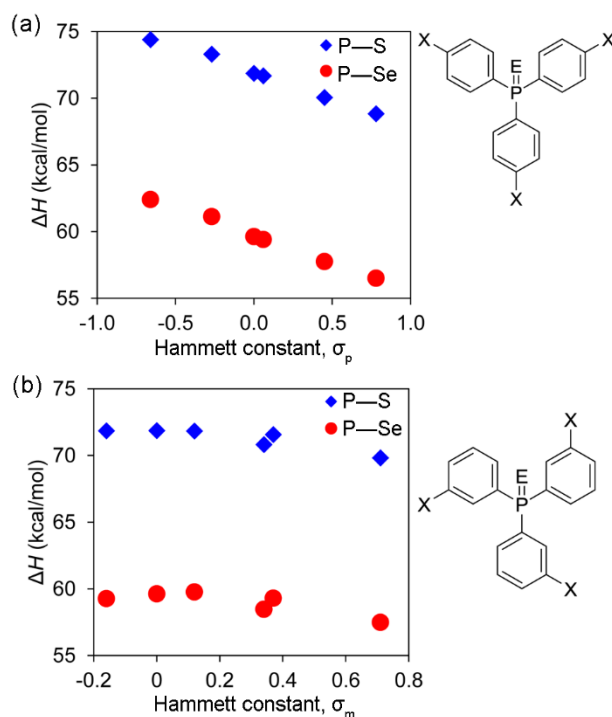
Figure 6. Calculated ΔH of P—E BDE against Hammett constant in (a) 4- and (b) 3-substituted triarylphosphine chalcogenides.

Based on the simplicity and usefulness of the Hammett constant in describing BDE in these compounds, we also investigated whether it is a useful tool in describing the partial charge (Löwdin charge) on phosphorus and chalcogen atoms (figures 7a-7d). As described previously, positive Löwdin charge on the P atom is greater for phosphine selenides than phosphine sulfides, while negative Löwdin charge is greater on the Se atom than the S atom. Substitution at the 4-

position (figures 7a and 7b) appears to have a greater effect on the partial charge of both the P and E atoms than substitution at the 3-position (figures 7c and 7d). This trend is visible in both P—S and P—Se bonds. We see that the Löwdin charge on P slightly decreases with increasing Hammett constant across a P—S or P—Se series in both 4-sbustituted (figure 7a) and 3-substituted (figure 7c) compounds. On the other hand, we notice that negative Löwdin charge decreases with increasing Hammett constant across a P—S or P—Se series in the 4-substituted (figure 7b) and 3-substituted (figure 7d) compounds.
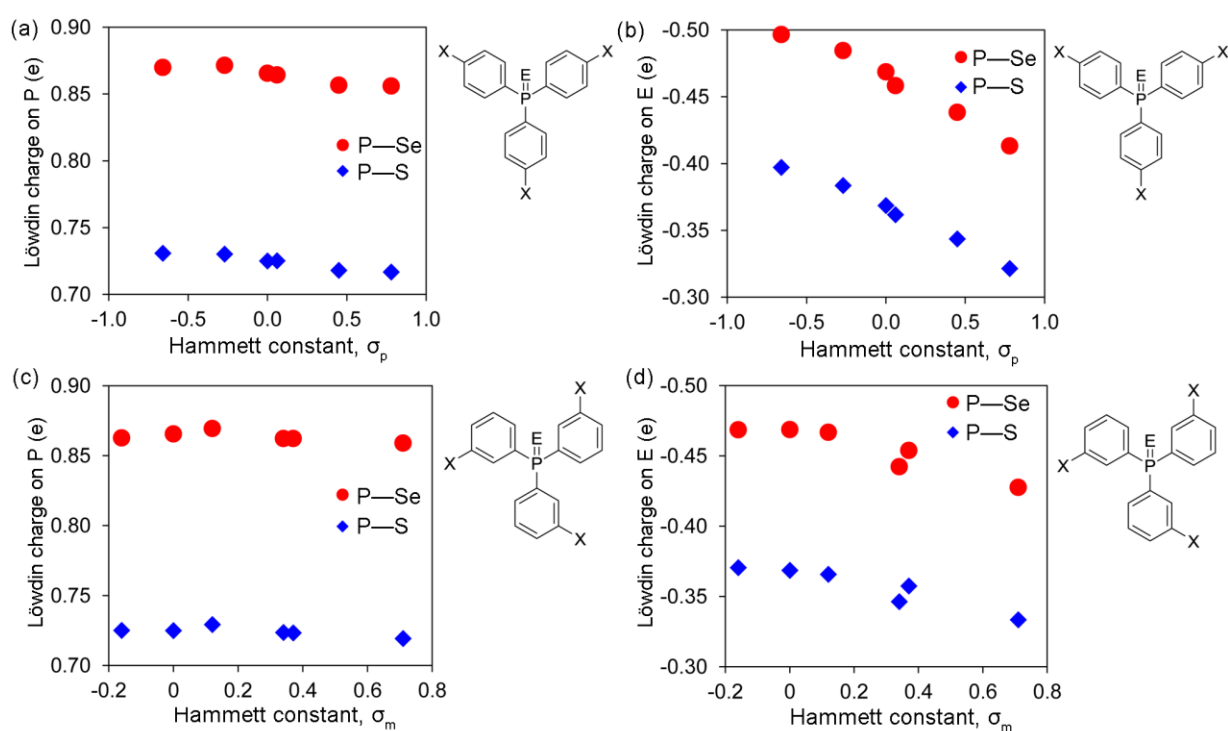

Figure 7. Löwdin charge on (a) phosphorus and (b) chalcogen in 4-substituted phosphine chalcogenides as well as (c) phosphorus and (d) chalcogen in 3-substituted phosphine chalcogenides against Hammett constants.

Bond order and substituent constants. As seen above, bonding in the phosphine chalcogenides appears to have an ionic character to it. Traditionally, the Lewis diagrams of these compounds formally show a phosphorus-chalcogen double bond (see scheme 1) but computational[24] and experimental studies have shown that this is not necessarily the case. We further examined the bond order of the ortho- and para-monosubstituted triphenylphosphine

chalcogenides computed from the Löwdin charges to see how partial charge influences the resulting covalent portion of the P—E bond. Bond orders were determined in GAMESS from the sum of the density matrices of the atoms in question, as described previously.[56–58]

As may be expected, generally the bond order of the P—Se bond is lower than that of the P—S bond, due to the significantly larger radius of the Se atom compared to S. Correlating the Hammett constant of the monosubstituted triarylphosphine chalcogenides to the calculated bond order (figure 8) shows that substituents with more electron withdrawing character increase the bond order relative to Ph₃PE while electron donating substituents decrease the bond order. In fact, this correlation applies to both substitution at the 4-position (figure 8a) and at the 3-position (figure 8b). This agrees with the earlier observation that electron donating groups increase the positive charge on P and increase the negative charge on S and Se.
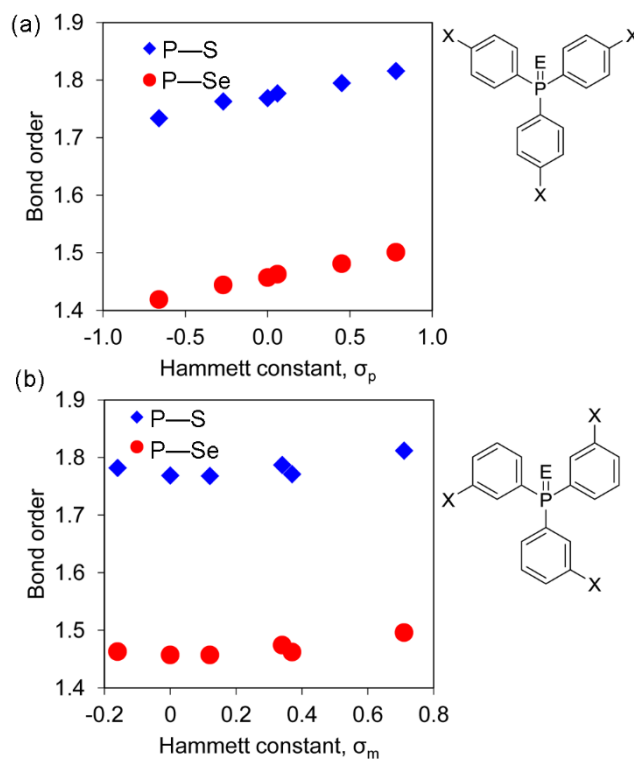

Figure 8. Correlation of Hammett constant and bond order in (a) 4-substituted triarylphosphine chalcogenides and (b) 3-substituted triarylphosphine chalcogenides.

The data from all the Hammett constant correlations suggest that monosubstituted triphenylphosphine chalcogenides with electron-donating substituents have stronger P—E bonds with greater positive charge on P and greater negative charge on E. Based on our earlier evidence that longer bonds are slightly stronger in these compounds, it may be that these longer bonds also have more ionic character. Many of these compounds exhibit bond orders between 1 and 2, and could be described using structure III in scheme 1.

Correlating experimental and computational results. We also investigated selected triarylphosphine compounds experimentally with ^{31}P and ^{77}Se spectroscopy to estimate the relative amount of shielding around each nucleus (see Appendix for complete table of NMR chemical shifts). The compounds we monitored by NMR include (2,4,6-MeO$_3$-C$_6$H$_2$)$_3$PE, (4-MeO-C$_6$H$_4$)$_3$PE, (4-F-C$_6$H$_4$)$_3$PE, and Ph$_3$PE; additionally we add data from compounds we studied previously[26]: (PhO)$_3$PE, (Et$_2$N)$_3$PE, (n-Pr)Ph$_2$PE, (n-Bu)$_3$PE and (n-Octyl)$_3$PE. The effect of substituents on P—E bonds has also been investigated in related arylphosphorothionates[59] and triarylselenophosphates.[60] The ^{31}P-^{77}Se coupling constant has been shown to be influenced by adjacent substituents.[61]

The scattered values in ^{31}P chemical shift show no clear correlation with BDE in the studied phosphine sulfides or phosphine selenides (figure 9). We also checked to see if the ^{31}P-^{77}Se ^{1}J coupling constant shows any correlation to calculated BDE, but again the scattering of these values show little positive or negative correlation in the studied compounds. However, in light of our computational results, we have seen that the phosphorus-chalcogen bond strength is also subject to the partial charge about the chalcogen (see above). When ^{77}Se chemical shifts are plotted against calculated ΔH of bond dissociation (figure 10), a correlation of generally downfield-shifted NMR signal with increasing ΔH appears. This implies that as the selenium

nucleus becomes more shielded by electron density, the bond strength increases, as inferred from our calculations.
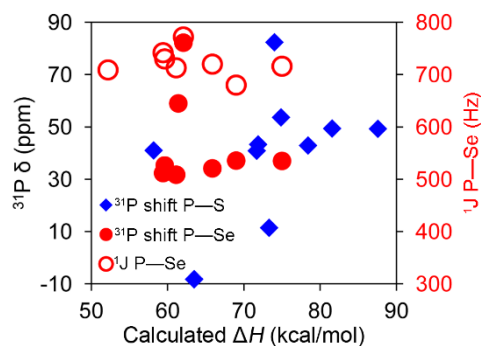
Figure 9. ^{31}P NMR chemical shifts and [1]J P—Se coupling constants plotted against calculated ΔH of bond dissociation.
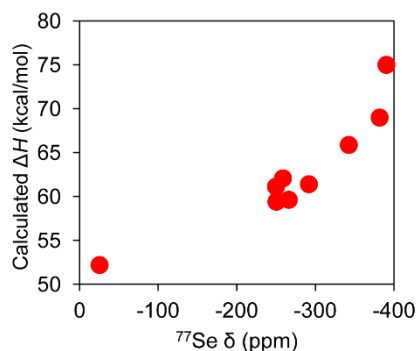
Figure 10. Correlation between [77]Se chemical shift and calculated ΔH of bond dissociation.

Conclusions

We investigated the bond strength and nature of bonding in multiple families of phosphine chalcogenide compounds. Generally, within a family, DFT computations show that as the P—E bond distance increases, the BDE also increases. This may be due to increasing the partial negative charge on the chalcogen atom and increasing the partial positive charge on the phosphorus atom. The result is a stronger, slightly longer bond with greater ionic character. Monosubstituted triarylphosphine chalcogenides with electron-donating groups and negative Hammett constants exhibit stronger bonds while the same class of compound with electron-withdrawing groups and positive Hammett constants exhibit weaker bonds. This implies that

electron-donating groups add electron density to the P—E unit; the more electronegative chalcogen atom accepts this electron density and forms a bond of more ionic character compared to compounds with electron-withdrawing groups. The result of this is that formal bond orders are between 1 and 2. We also show that these computational results can be verified by ^{77}Se NMR spectroscopy, which shows that more shielded nuclei with more negative chemical shifts correspond to greater BDEs. This suggests that more electron density around the chalcogen atom creates a stronger bond with more ionic character. We anticipate that these results will allow for the design of new atom transfer and quantum dot synthesis reagents with enhanced reactivity.

Acknowledgments

References

[1] Davies, R. Chalcogen-Phosphorus (and Heavier Cogeners) Chemistry. In *Handbook of Chalcogen Chemistry: New Perspectives in Sulfur, Selenium and Tellurium*; Devillanova, F. A., ed.; Royal Society of Chemistry: Cambridge, 2007; pp. 286–343.

[2] Donahue, J. P. Thermodynamic Scales for Sulfur Atom Transfer and Oxo-for-Sulfido Exchange Reactions. *Chem. Rev.* **2006**, *106*, 4747–4783.

[3] Brown, D. H.; Cross, R. J.; Keat, R. Rapid Transfer of Selenium from Tertiary Phosphine Selenides to Tertiary Phosphines. *J. Chem. Soc., Dalton Trans.* **1980**, 871–874.

[4] Baechler, R. D.; Stack, M.; Stevenson, K.; Vanvalkenburgh, V. *Phosphorus, Sulfur, Silicon and Rel. Elem.* **1990**, *48*, 49–52.

[5] Kullberg, M.; Stawinski, J. Theoretical Investigations on the Mechanism of Chalcogen Exchange Reaction Between P(V) and P(III) Compounds. *J. Organomet. Chem.* **2005**, *690*, 2571–2576.

[6] Aizawa, S.; Majumder, A.; Maeda, D.; Kitamura, A. Mechanism of Catalytic Chalcogen Atom Replacement of Phosphine Chalcogenides and Separation of the Intermediate Phosphine. *Chem. Lett.* **2009**, *38*, 18–19.

[7] Tsukuda, T.; Miyoshi, R.; Esumi, A.; Yamagiwa, A.; Dairiki, A.; Matsumoto, K..; Tsubomura, T. Sulfur Transfer Reaction from Phosphine Sulfides to Phosphines Assisted by Metal Ions. *Inorg. Chim. Acta* **2012**, *384*, 149–153.

[8] Bollmark, M.; Stawinski, J. A New Selenium-transferring Reagent – Triphenylphosphine Selenide. *Chem. Commun.* **2001**, 771–772.

[9] McDonough, J. E.; Mendiratta, A.; Curley, J. J.; Fortman, G. C.; Fantasia, S.; Cummins, C. C.; Rybak-Akimova, E. V.; Nolan, S. P.; Hoff, C. D. Thermodynamic, Kinetic and Computational Study of Heavier Chalcogen (S, Se, and Te) Terminal Multiple Bonds to Molybdenum, Carbon and Phosphorus. *Inorg. Chem.* **2008**, *47*, 2133–2141.

[10] Murray, C. B.; Norris, D. J.; Bawendi, M. G. Synthesis and Characterization of Nearly Monodisperse CdE (E = S, Se, Te) Semiconductor Nanocrystallites. *J. Am. Chem. Soc.* **1993**, *115*, 8706–8715.

[11] García-Rodríguez, R.; Hendricks, M. P.; Cossairt, B. M.; Liu, H.; Owen, J. S. Conversion Reactions of Cadmium Chalcogenide Nanocrystal Precursors. *Chem. Mater.* **2013**, *25*, 1233–1249.

[12] Sowers, K. L.; Swartz, B.; Krauss, T. D. Chemical Mechanisms of Semiconductor Nanocrystal Synthesis *Chem. Mater.* **2013**, *25*, 1351–1362.

[13] Bullen, C. R.; Mulvaney, P. Nucleation and Growth Kinetics of CdSe Nanocrystals in Octadecene. *Nano Letters* **2004**, *4*, 2303–2307.

[14] Yang, P.; Tretiak, S.; Ivanov, S. Influence of Surfactants and Charges on CdSe Quantum Dots. *J. Cluster Sci.* **2011**, 2*2,* 405–431.

[15] Evans, C. M.; Evans, M. E.; Krauss, T. D. Mysteries of TOPSe Revealed: Insights into Quantum Dot Nucleation. *J. Am. Chem. Soc.* **2010**, *132*, 10973–10975.

[16] Steckel, J. S.; Yen, B. K. H.; Oertel, D. C.; Bawendi, M. G. On the Mechanism of Lead Chalcogenide Nanocrystal Formation. *J. Am. Chem. Soc.* **2006**, *128*, 13032–13033.

[17] Koh, W.-k.; Yoon, Y.; Murray, C. B. Investigating the Phosphine Chemistry of Se Precursors for the Synthesis of PbSe Nanorods. *Chem. Mater.* **2011**, *23*, 1825–1829.

[18] Liu, H.; Owen, J. S.; Alivisatos, A. P. Mechanistic Study of Precursor Evolution in Colloidal Group II-VI Semiconductor Nanocrystal Synthesis. *J. Am. Chem. Soc.* **2007**, *129*, 305–312.

[19] Gary, D. C.; Glassy, B. A.; Cossairt, B. M. Investigation of Indium Phosphide Quantum Dot Nucleation and Growth Utilizing Triarylsilylphosphine Precursors. *Chem. Mater.* **2014**, *26*, 1734–1744.

[20] Chernick, C. L.; Pedley, J. B.; Skinner, H. A. Thermochemistry of Organophosphorus Compounds. Part III. The Heat of Addition of Sulphur to Triethyl Phosphite, and to Tri-*n*-propyl- and Tri-*n*-butyl-phosphine. *J. Chem. Soc.* **1957**, 1851–1854.

[21] Capps, K. B.; Wixmerten, B.; Bauer, A.; Hoff, C. D. Thermochemistry of Sulfur Atom Transfer. Enthalpies of Reaction of Phosphines with Sulfur, Selenium, and Tellurium, and of Desulfurization of Triphenylarsenic Sulfide, Triphenylantimony Sulfide, and Benzyl Trisulfide. *Inorg. Chem.* **1998**, *37*, 2861–2864.

[22] Gilheany, D. G. No *d* Orbitals but Walsh Diagrams and Maybe Banana Bonds: Chemical Bonding in Phosphines, Phosphine Oxides and Phosphonium Ylides. *Chem. Rev.* **1994**, *94*, 1339–1374.

[23] Ibdah, A.; Espenson, J. A.; Jenks, W. S. Computational Study of Sulfur Atom-Transfer Reactions from Thiiranes to ER_3 (E = As, P; R = CH_3, Ph). *Inorg. Chem.* **2005**, *44*, 8426–8432.

[24] Sandblom, N.; Ziegler, T.; Chivers, T. A density functional study of the bonding in tertiary phosphine chalcogenides and related molecules. *Can. J. Chem.* **1996**, *74*, 2363–2371.

[25] Dobado, J. A.; Martínez-García, H.; Molina, J.; Sundberg, M. R. Chemical Bonding in Hypervalent Molecules Revised. Application of the Atoms in Molecules Theory to Y_3X and Y_3XZ (Y = H or CH_3; X = N, P or As; Z = O or S) Compounds. *J. Am. Chem. Soc.* **1998**, *120*, 8461–8471.

[26] Ruberu, T. P. A.; Albright, H. R.; Callis, B.; Ward, B.; Cisneros, J.; Fan, H.-J.; Vela, J. Molecular Control of the Nanoscale: Effect of Phosphine-Chalcogenide Reactivity on CdS-CdSe Nanocrystal Composition and Morphology. *ACS Nano* **2012**, *6*, 5348–5359.

[27] Verkade, J. G.; Kisanga, P. B. Proazaphosphatranes: A Synthesis Methodology Trip from Their Discovery to Vitamin A. *Tetrahedron* **2003**, *59*, 7819–7858.

[28] Schmidt, M. W.; Baldridge, K. K.; Boatz, J. A.; Elbert, S. T.; Gordon, M. S.; Jensen, J. S.; Koseki, S.; Matsunaga, N.; Nguyen, K. A.; Su, S.; Windus, T. L.; Dupuis, M.; Montgomery, J. A. General Atomic and Molecular Electronic-Structure System. *J. Comput. Chem.*, **1993**, *14*, 1347–1363.

[29] Gordon, M. S.; Schmidt, M. W. Advances in Electronic Structure Theory: GAMESS a Decade Later. In *Theory and Applications of Computational Chemistry: The First Forty Years*; Dykstra, C. E., Frenking, G., Kim, K. S., Scuseria, G. E., Eds.; Elsevier Science: Amsterdam, 2005; p 1167.

[30] Perdew, J. P.; Tao, J.; Staroverov, V. N.; Scuseria, G. E. Climbing the Density Functional Ladder: Nonempirical Meta-Generalized Gradient Approximation Designed for Molecules and Solids. *Phys. Rev. Lett.* **2003**, *91*, 146401.

[31] Perdew, J. P.; Tao, J.; Staroverov, V. N.; Scuseria, G. E. Meta-generalized Gradient Approximation: Explanation of a Realistic Nonempirical Density Functional. *J. Chem. Phys.* **2004**, *120*, 6898–6911.

[32] Staroverov, V. N.; Scuseria, G. E.; Tao, J. M.; Perdew, J. P. Comparative Assessment of a New Nonempirical Density Functional: Molecules and Hydrogen-bonded Complexes. *J. Chem. Phys.* **2003**, *119*, 12129–12137.

[33] Fan, Y.; Bacon, S.; Kolade, A.; Wasiu, A.; Fan, H.-J. ICCS: A DFT Study on the Mechanism of Wolff Rearrangement in a Five-member Iridacycle. *ICCS 2010 - International Conference on Computational Science, Proceedings* 2010, 1, 2653–2661.

[34] Krishnan, R.; Binkley, J. S.; Seeger, R.; Pople, J. A. Self-consistent Molecular Orbital Methods. XX. A Basis Set for Correlated Wave functions. *J. Chem. Phys.*, **1980**, *72*, 650–654.

[35] Fan, Y. B.; Hall, M. B. The Competition Between Allene and Butadiene in the Carbon-hydrogen Bond Activation Initiated by a Tungsten Allyl Complex: A DFT Study. *Organometallics* **2005**, *24*, 3827–3835.

[36] Bode, B. M.; Gordon, M. S. MacMolPlt: A Graphical User Interface for GAMESS. *J. Mol. Graphics Modell.* **1998**, *16*, 133–138.

[37] Wada, M.; Kanzaki, M.; Fujiwara, M.; Kajihara, K.; Erabi, T. Some Unusual Properties of Tris(2,6-dimethoxyphenyl)phosphine Sulfide and the Related Compounds. *Bull. Chem. Soc. Jpn.* **1991**, *64*, 1782–1786.

[38] Burdon, J.; Rozhkov, I. N.; Perry, G. M. Aromatic Polyfluoro-compounds. Part XLVI. Nucleophilic Replacement Reactions of Pentafluorodiphenylphosphine and its Oxide and Sulphide. *J. Chem. Soc. C* **1969**, 2615–2617.

[39] Emeléus, H. J.; Miller, J. M. Pentafluorophenyl Phosphorus Chemistry. I. Tris(pentafluorophenyl)phosphine sulphide and tris(pentafluorophenyl)dichlorophosphorane. *J. Inorg. Nucl. Chem.* **1966**, *28*, 662–665.

[40] Miller, J. M. Mass Spectral Studies of Some Perhalogenoaromatic Derivatives. *J. Chem. Soc. A* **1967**, 828–834.

[41] Guo, Y.; Alvarado, S. R.; Barclay, J. D.; Vela, J. Shape-Programmed Nanofabrication: Understanding the Reactivity of Dichalcogenide Precursors. *ACS Nano* **2013**, *7*, 3616–3626.

[42] Kaupp, M.; Metz, B.; Stoll, H. Breakdown of Bond Length-Strength Correlation: A Case Study. *Angew. Chem. Int. Ed.* **2000**, *39*, 4607–4609.

[43] Kaupp, M.; Riedel, S. On the Lack of Correlation Between Bond Lengths, Dissociation Energies, and Force Constants: The Fluorine-substituted Ethane Homologues. *Inorg. Chim. Acta* **2004**, *357*, 1865–1872.

[44] Lindquist, B. A.; Dunning, T. H. Bonding in $FSSF_3$: Breakdown in Bond Length-Strength Correlations and Implications for SF_2 Dimerization. *J. Phys. Chem. Lett.* **2013**, *4*, 3139–3143.

[45] Ernst, R. D.; Freeman, J. W.; Stahl, L.; Wilson, D. R.; Arif, A. M.; Nuber, B.; Ziegler, M. L. Longer but Stronger Bonds: Structures of PF_3, $P(OEt)_3$, and PMe_3 Adducts of an Open Titanocene. *J. Am. Chem. Soc.* **1995**, *117*, 5075–5081.

[46] Wada, M.; Higashizaki, S. A Highly Basic Triphenylphosphine, $[2,4,6-(MeO)_3C_6H_2]_3P$. *J. Chem. Soc., Chem. Commun.* **1984**, 482–483.

[47] CRC Handbook of Chemistry and Physics, 95th Ed.; CRC Press, Boca Raton, FL 2014–2015.

[48] Bautista, J. L.; Flores-Alamo, M.; Tiburcio, J.; Vieto, R.; Torrens, H. Synthesis and Structural Characterization of Fluorinated Thiosemicarbazones. *Molecules* **2013**, *18*, 13111–13123.

[49] Wang, Y.; Parkin, S. R.; Gierschner, J.; Watson, M. D. Highly Fluorinated Benzobisbenzothiophenes. *Org. Lett.* **2008**, *10*, 3307–3310.

[50] Mulliken, R. S. Electronic Population Analysis on LCAO-MO Molecular Wavefunctions. I. *J. Chem. Phys.* **1955**, *23*, 1833–1840.

[51] Mulliken, R. S. Electronic Population Analysis on LCAO-MO Molecular Wavefunctions. II. Overlap Populations, Bond Orders, and Covalent Bond Energies. *J. Chem. Phys.* **1955**, *23*, 1841–1846.

[52] Mulliken, R. S. Population Analysis on LCAO-MO Molecular Wavefunctions. III. Effects of Hybridization on Overlap and Gross AO Populations. *J. Chem. Phys.* **1955**, *23*, 2338–2342.

[53] Mulliken, R. S. Analysis on LCAO-MO Molecular Wavefunctions. IV. Bonding and Antibonding in LCAO and Valence-Bond Theories. *J. Chem. Phys.* **1955**, *23*, 2343–2346.

[54] Löwdin, P.-O. *Adv. Chem. Phys.* **1970**, *5*, 185–199.

[55] Hansch, C.; Leo, A.; Taft, R. W. A Survey of Hammett Substituent Constants and Resonance and Field Parameters. *Chem. Rev.* **1991**, *91*, 165–195.

[56] Giambiagi, M.; Giambiagi, M.; Grempel, D. R.; Heymann, C. D. Definition of the Ave. Bond Index with Non-orthogonal Basis – Properties and Calculation. *J. Chim. Phys. Phys.-Chim. Biol.* **1975**, *72*, 15–22.

[57] Mayer, I. Charge, Bond Order and Valence in the Ab Initio SCF Theory. *Chem. Phys. Lett.* **1983**, *97*, 270–274.

[58] Mayer, I. Charge, Bond Order and Valence in the Ab Initio SCF Theory. *Chem. Phys. Lett.* **1985**, *117*, 396.

[59] Hernández, J.; Goycoolea, F. M.; Zepeda-Rivera, D.; Juárez-Onofre, J.; Martínez, Lizardi, J.; Salas-Reyes, M.; Gordillo, B.; Velázquez-Contreras, C.; García-Barradas, O.; Cruz-Sánchez, S.; Domínquez, Z. Substituent Effects on the ^{31}P NMR Chemical Shifts of Arylphosphorothionates. *Tetrahedron* **2006**, *62*, 2520–2528.

[60] Domínquez, Z.; Hernández, J.; Silva-Gutiérrez, L.; Salas-Reyes, M.; Sánchez, M.; Merino, G. *Phosphorus, Sulfur, Silicon and Rel. Elem.* **2010**, *185*, 772–784.

[61] Pinnell, R. P.; Megerle, C. A.; Manatt, S. L.; Kroon, P. A. Nuclear Magnetic Resonance of Phosphorus Compounds. VII. Evidence for Steric Effects on the ^{31}P-^{77}Se Coupling and ^{31}P Chemical Shifts. *J. Am. Chem. Soc.* **1973**, *95*, 977–978.
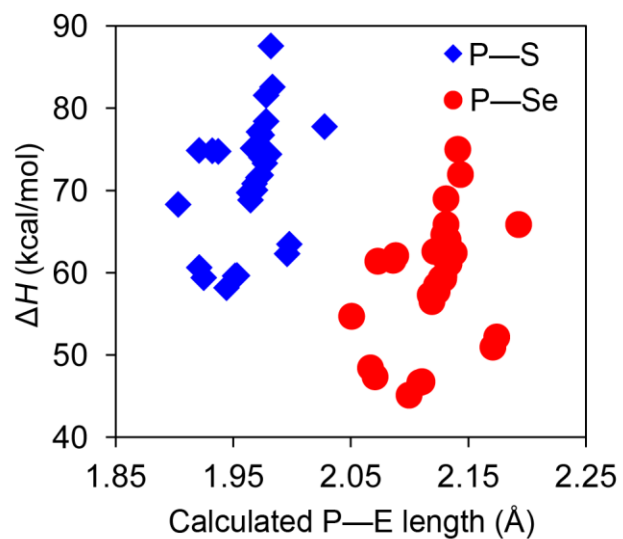
Appendix of supporting information

Figure S1. Computed ΔH of P=E bond dissociation for all phosphine chalcogenides in this work.

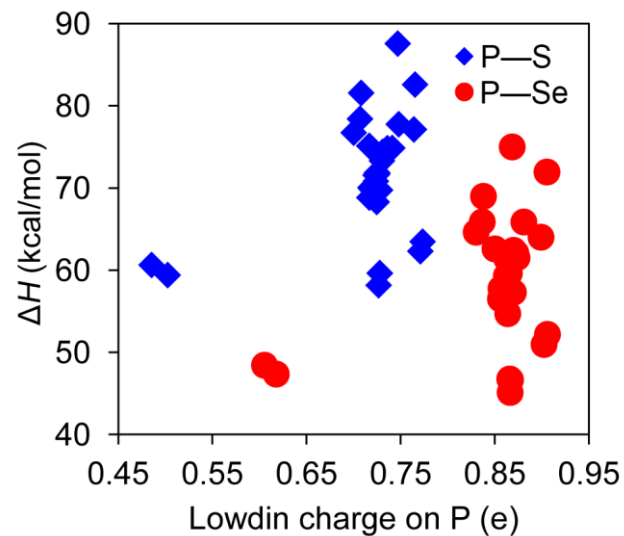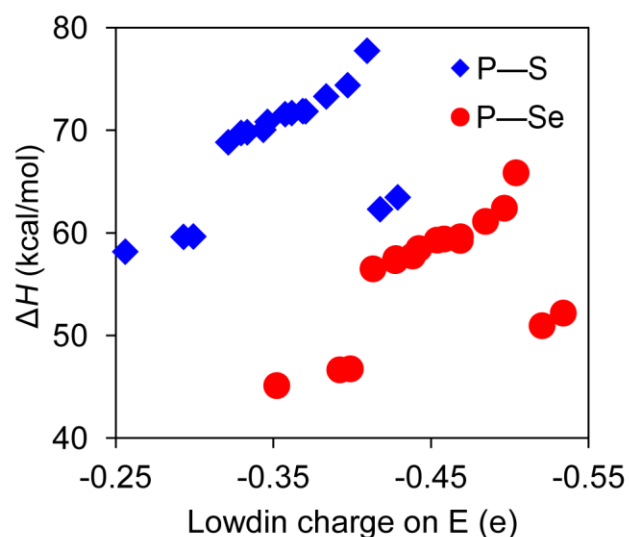Figure S2. Lowdin charge on P in all phosphine chalcogenides in this work.

Figure S3. Lowdin charge on E in all phosphine chalcogenides in this work.

Table S1. Monosubstituted triarylphosphines								
Compound	P=E distance (Å)	R-P=E angle (°)	Mulliken charges (P, E) (e)	Bond order	ΔH (kcal/mol)	ΔG (kcal/mol)	ΔE (kcal/mol)	ΔE$_{ZPE}$ (kcal/mol)
Ph$_3$PS	1.973	113.683 (113.676, 113.678, 113.694)	0.7250, -0.3686	1.769	71.8707	62.4748	74.8487	73.0578
(4-NO$_2$-C$_6$H$_4$)$_3$PS	1.965	113.769 (113.76439,113.77877,113.76453)	0.7167, -0.3214	1.816	68.8309	59.9389	71.2160	69.7589
(3-NO$_2$-C$_6$H$_4$)$_3$PS	1.966	113.807 (113.83814,113.79892,113.78364)	0.7193, -0.3334	1.812	69.8182	60.4142	72.4955	70.8702
(4-NH$_2$-C$_6$H$_4$)$_3$PS	1.980	113.360 (113.35076,113.35287,113.37497)	0.7309, -0.3971	1.734	74.3988	65.1728	77.4419	79.0114
(3-NH$_2$-C$_6$H$_4$)$_3$PS	1.973	113.789 (113.70691,113.91286,113.7477)	0.7251, -0.3705	1.782	71.8516	62.4686	74.7051	75.5838
(2-NH$_2$-C$_6$H$_4$)$_3$PS	2.028	112.108 (112.11932,112.05105,112.1544)	0.7480, -0.4095	1.619	77.7584	66.4784	81.2654	72.9976
(4-CO$_2$H-C$_6$H$_4$)$_3$PS	1.969	113.858 (113.84442,113.85	0.7180, -0.3436	1.795	70.0502	60.8502	72.7154	71.1002

		445,113.87524)					
(3-CO$_2$H-C$_6$H$_4$)$_3$PS	1.971	113.605 (113.46271,113.6296,113.72281)	0.7233, -0.3575	1.771	71.5703	61.9003	74.3478	72.6623
(4-MeO-C$_6$H$_4$)$_3$PS	1.977	113.518 (113.51142,113.53325,113.51064)	0.7301, -0.3835	1.763	73.3056	64.0256	76.2638	74.4986
(3-MeO-C$_6$H$_4$)$_3$PS	1.972	113.866 (113.85873,113.86483,113.87372)	0.7292, -0.3658	1.768	71.8391	62.0511	74.7920	73.0011
(4-F-C$_6$H$_4$)$_3$PS	1.972	113.575 (113.57953,113.56953,113.57548)	0.7251, -0.3617	1.777	71.6830	62.1060	74.6623	72.8670
(3-F-C$_6$H$_4$)$_3$PS	1.968	113.763 (113.76777,113.75524,113.76656)	0.7236, -0.3463	1.787	70.8257	61.1857	73.6762	71.9437
Ph$_3$PSe	2.129	113.669 (113.66519,113.64069,113.70113)	0.8655, -0.4687	1.457	59.6226	50.1886	61.9164	60.5716
(4-NO$_2$-C$_6$H$_4$)$_3$=Se	2.119	113.777 (113.78023,113.80853,113.74126)	0.8560, -0.4132	1.501	56.5005	47.5225	58.1317	57.1615
(3-NO$_2$-C$_6$H$_4$)$_3$PSe	2.120	113.807 (113.80037,113.78882,113.83073)	0.8589, -0.4277	1.496	57.4948	48.0208	59.4307	58.2848
(4-NH$_2$-C$_6$H$_4$)$_3$PSe	2.138	113.322 (113.33765,113.32968,113.29916)	0.8699, -0.4965	1.419	62.4113	53.2053	64.6545	66.7967
(3-NH$_2$-C$_6$H$_4$)$_3$PSe	2.129	113.731 (113.65285,113.84047,113.69935)	0.8626, -0.4686	1.463	59.2717	49.7277	61.1795	63.3493
(2-NH$_2$-C$_6$H$_4$)$_3$PSe	2.193	111.903 (111.92917,111.90585,111.87424)	0.8809, -0.5040	1.339	65.8627	54.6208	68.4936	60.0807
(4-CO$_2$H-	2.133	113.871	0.8566,	1.481	57.7497	48.5087	59.7126	58.55

Compound	P=E distance (Å)	R-P=E angle (°)	Mulliken charges (P, E) (e)	Bond order	ΔH (kcal/mol)	ΔG (kcal/mol)	ΔE (kcal/mol)	ΔE$_{ZPE}$ (kcal/mol)
C$_6$H$_4$)$_3$PSe		(113.856 01,113.87 415,113.8 837)	-0.4383					67
(3-CO$_2$H-C$_6$H$_4$)$_3$PSe	2.127	113.640 (113.498 5,113.648 61,113.77 359)	0.8623, -0.4539	1.462	59.2978	49.9008	61.3244	60.13 28
(4-MeO-C$_6$H$_4$)$_3$PSe	2.170	113.470 (113.465 81,113.45 721,113.4 8567)	0.8714, -0.4846	1.444	61.1216	51.8396	63.3971	62.08 06
(3-MeO-C$_6$H$_4$)$_3$PSe	2.174	113.894 (113.897 34,113.87 133,113.9 1429)	0.8694, -0.4669	1.457	59.7621	50.3611	61.7954	60.47 51
(4-F-C$_6$H$_4$)$_3$PSe	2.128	113.577 (113.582 41,113.55 936,113.5 8834)	0.8642, -0.4583	1.463	59.4074	49.9674	61.6314	60.32 74
(3-F-C$_6$H$_4$)$_3$PSe	2.123	113.804 (113.803 19,113.79 713,113.8 1144)	0.8622, -0.4423	1.474	58.4772	49.0012	60.5886	59.33 92

Table S2. Fluorinated triaryl phosphines								
Compound	P=E distance (Å)	R-P=E angle (°)	Mulliken charges (P, E) (e)	Bond order	ΔH (kcal/mol)	ΔG (kcal/mol)	ΔE (kcal/mol)	ΔE$_{ZPE}$ (kcal/ mol)
(4-F-C$_6$H$_4$)$_3$PS	1.972	113.575 (113.579 53,113.5 6953,113 .57548)	0.7251, -0.3617	1.777	71.6830	61.1857	74.6623	72.86 70
(3-F-C$_6$H$_4$)$_3$PS	1.968	113.763 (113.767 77,113.7 5524,113 .76656)	0.7251, -0.3463	1.787	70.8257	62.1060	73.6762	71.94 37
(2,6-F$_2$-C$_6$H$_3$)$_3$PS	1.953	114.058 (114.434 87,109.4 8545,118 .2532)	0.7278, -0.2993	1.938	59.6551	49.4501	62.4175	60.69 31
(3,5-F$_2$-C$_6$H$_3$)$_3$PS	1.964	113.962 (113.957 88,113.9 6278,113 .96596)	0.7281, -0.3295	1.809	69.7446	60.2736	72.4954	70.82 06

Compound	P=E distance (Å)	R-P=E angle (°)	Mulliken charges (P, E) (e)	Bond order	ΔH (kcal/mol)	ΔG (kcal/mol)	ΔE (kcal/mol)	ΔE_ZPE (kcal/mol)
(2,4,6-F₃-C₆H₂)₃PS	1.952	114.104 (114.363 12,109.8 586,118. 09081)	0.7280, -0.2930	1.951	59.6167	49.3597	62.3465	60.63 77
(C₆F₅)₃PS	1.944	114.335 (114.539 76,110.2 295,118. 23713)	0.7266, -0.2561	1.987	58.1728	48.0048	60.7350	59.12 48
(4-F-C₆H₄)₃PSe	2.128	113.577 (113.582 41,113.5 5936,113 .58834)	0.8642, -0.4583	1.463	59.4074	49.0012	61.6314	60.32 74
(3-F-C₆H₄)₃PSe	2.123	113.804 (113.803 19,113.7 9713,113 .81144)	0.8622, -0.4423	1.474	58.4772	49.9674	60.5886	59.33 92
(2,6-F₂-C₆H₃)₃PSe	2.111	114.039 (114.392 07,108.6 8231,119 .04381)	0.8659, -0.3988	1.602	46.7536	36.6446	48.7224	47.51 26
(3,5-F₂-C₆H₃)₃PSe	2.118	114.021 (114.016 78,113.9 8715,114 .05931)	0.8698, -0.4273	1.495	57.3009	47.8259	59.3143	58.11 89
(2,4,6-F₃-C₆H₂)₃PSe	2.109	114.107 (114.361 04,109.0 7528,118 .88376)	0.8667, -0.3922	1.614	46.6571	36.4801	48.5740	47.39 11
(C₆F₅)₃PSe	2.100	114.410 (114.665 97,109.4 737,119. 09155)	0.8663, -0.3522	1.654	45.1173	35.0413	46.8468	45.77 63

Table S3. Methoxytriaryl phosphines								
Compound	P=E distance (Å)	R-P=E angle (°)	Mulliken charges (P, E) (e)	Bond order	ΔH (kcal/mol)	ΔG (kcal/mol)	ΔE (kcal/mol)	ΔE_ZPE (kcal/ mol)
(4-MeO-C₆H₄)₃PS	1.977	113.518 (113.511 42,113.5 3325,11 3.51064)	0.7301, -0.3835	1.763	73.3056	64.0256	76.2638	74.49 86
(3-MeO-C₆H₄)₃PS	1.972	113.866 (113.858 73,113.8 6483,11	0.7292, -0.3658	1.768	71.8391	62.0511	74.7920	73.00 11

		3.87372)						
(2,6-MeO$_2$-C$_6$H$_3$)$_3$PS	1.996	110.443 (110.53679,110.41926,110.3718)	0.7710, -0.4177	1.713	62.3128	51.6858	64.9545	63.3888
(2,4,6-MeO$_3$-C$_6$H$_2$)$_3$PS	1.998	110.492 (110.51128,110.41019,110.55478)	0.7733, -0.4289	1.712	63.4724	52.3674	66.2958	64.6084
(4-MeO-C$_6$H$_4$)$_3$PSe	2.133	113.470 (113.46581,113.45721,113.48567)	0.8714, -0.4846	1.444	61.1216	51.8396	63.3971	62.0806
(3-MeO-C$_6$H$_4$)$_3$PSe	2.127	113.894 (113.89734,113.87133,113.91429)	0.8694, -0.4669	1.457	59.7621	50.3611	61.7954	60.4751
(2,6-MeO$_2$-C$_6$H$_3$)$_3$PSe	2.170	110.129 (110.33628,110.02702,110.02408)	0.9023, -0.5205	1.349	50.9578	40.1768	52.7919	51.7628
(2,4,6-MeO$_3$-C$_6$H$_2$)$_3$PSe	2.174	110.127 (110.27908,110.13288,109.97043)	0.9060, -0.5339	1.347	52.1891	41.1191	54.1637	53.0511

Table S4. Trialkyl and triperfluoroalkyl phosphines								
Compound	P=E distance (Å)	R-P=E angle (°)	Mulliken charges (P, E) (e)	Bond order	ΔH (kcal/mol)	ΔG (kcal/mol)	ΔE (kcal/mol)	ΔE$_{ZPE}$ (kcal/mol)
(H$_3$C)$_3$PS	1.921	114.563 (114.57114,114.55821,114.55822)	0.7166, -0.3940	1.870	75.1313	65.8493	78.2662	76.3403
(H$_3$CH$_2$C)$_3$PS	1.925	114.343 (114.3271,114.35514,114.34733)	0.7001, -0.3973	1.881	76.7322	67.1272	80.0124	78.0132
(n-Bu)$_3$PS	1.967	114.2 (114.1,114.2,114.3)	0.7068, -0.4023	1.921	78.41	68.38	79.88	77.71
(n-Octyl)$_3$PS	1.974	114.2 (114.2,114.2,114.2)	0.7080, -0.4026	1.915	81.57	71.60	82.86	80.99

Compound	P=E distance (Å)	R-P=E angle (°)	Mulliken charges (P, E) (e)	Bond order	ΔH (kcal/mol)	ΔG (kcal/mol)	ΔE (kcal/mol)	ΔE$_{ZPE}$ (kcal/mol)
(F$_3$C)$_3$PS	1.978	116.808 (116.83294,116.8225,116.76746)	0.4854, -0.1883	1.985	60.6333	51.4813	63.1363	61.6353
(F$_3$CF$_2$C)$_3$PS	1.978	117.498 (117.39752,117.51615, 117.58056)	0.5024, -0.1917	1.971	59.4030	49.2180	61.6728	60.2420
(H$_3$C)$_3$PSe	2.067	114.556 (114.57446,114.54726, 114.54725)	0.8502, -0.4885	1.651	62.5888	53.4778	65.1570	63.6008
(H$_3$CH$_2$C)$_3$PSe	2.071	114.387 (114.34602,114.39597, 114.41869)	0.8302, -0.4911	1.643	64.6183	55.1153	67.2605	65.6703
(n-Bu)$_3$PSe	2.121	114.3 (114.3,114.3,114.3)	0.8367, -0.4946	1.674	65.87	56.23	67.04	65.43
(n-Octyl)$_3$PSe	2.129	114.267 (114.2,114.3,114.3)	0.8380, -0.4947	1.668	68.99	59.10	70.07	68.60
(F$_3$C)$_3$PSe	2.131	117.079 (117.15299,117.08954, 116.99342)	0.6053, -0.2821	1.651	48.4328	39.3428	50.1785	49.1538
(F$_3$CF$_2$C)$_3$PSe	2.131	117.810 (117.80418,117.78936, 117.83635)	0.6178, -0.2856	1.643	47.3534	37.4304	48.7443	47.8784

Table S5. Caged phosphines								
Compound	P=E distance (Å)	R-P=E angle (°)	Mulliken charges (P, E) (e)	Bond order	ΔH (kcal/mol)	ΔG (kcal/mol)	ΔE (kcal/mol)	ΔE$_{ZPE}$ (kcal/ mol)
HC(CH$_2$NH)$_3$PS	1.937	116.920 (116.92928,116.91862,116.91146)	0.7351, -0.3469	1.827	74.7555	65.3965	77.9806	76.0365

HC(CH₂O)₃PS	1.903	116.583 (116.5882,116.5667,116.59476)	0.7245, -0.2507	1.878	68.3068	58.3918	71.6156	69.5648
N(CH₂NH)₃PS	1.932	117.522 (117.50618,117.54328,117.51679)	0.7360, -0.2507	1.868	74.8250	65.5160	78.1970	76.1990
N(CH₂CH₂NH)₃PS	1.983	107.879 (106.14115,108.04167,109.4529)	0.7653, -0.4609	1.654	82.5854	72.7444	86.4894	84.1074
N(CH₂CH₂NCH₃)₃PS	1.972	112.924 (112.3374,113.3758,113.06004)	0.7641, -0.3987	1.725	77.1321	67.3241	81.7015	79.0621
HC(CH₂NH)₃PSe	2.088	117.007 (117.02211,117.00917,116.98964)	0.8723, -0.4501	1.593	62.0797	52.8427	64.5470	63.0767
HC(CH₂O)₃PSe	2.051	116.68467 (116.69051,116.66414,116.69936)	0.8638, -0.3498	1.670	54.7059	45.5389	57.2218	55.6599
N(CH₂NH)₃PSe	2.086	117.0995533 (117.10722,117.10297,117.08847)	0.8736, -0.4430	1.600	61.5171	52.3761	63.9203	62.4921
N(CH₂CH₂NH)₃PSe	2.143	107.3443133 (105.70087,107.46123,108.87084)	0.9054, -0.5711	1.395	71.9459	60.9670	73.9151	71.9459
N(CH₂CH₂NCH₃)₃PSe	2.133	112.9270633	0.8991, -0.5028	1.470	64.0119	54.1829	67.8840	65.6889

		(112.60 472,11 2.8973 6,113.2 7911)						

Table S6. ^{31}P and ^{77}Se chemical shifts		
Compound	^{31}P δ (ppm)	^{77}Se δ (ppm)
(PhO)$_3$P	128.43	
(Et$_2$N)$_3$P	122.58	
(n-Pr)Ph$_2$P	-16.04	
(n-Bu)$_3$P	-30.02	
(n-Octyl)$_3$P	-30.07	
Ph$_3$P	-5.51	
(4-MeO-C$_6$H$_4$)$_3$P	-10.10	
(2,4,6-MeO$_3$-C$_6$H$_2$)$_3$P	-69.97	
(4-F-C$_6$H$_4$)$_3$P	-9.17	
(C$_6$F$_5$)$_3$P	-74.32	
(PhO)$_3$PS	53.65	
(Et$_2$N)$_3$PS	82.37	
(n-Pr)Ph$_2$PS	42.89	
(n-Bu)$_3$PS	49.39	
(n-Octyl)$_3$PS	49.28	
Ph$_3$PS	43.31	
(4-MeO-C$_6$H$_4$)$_3$PS	41.02	
(2,4,6-MeO$_3$-Ar)$_3$PS	11.44	
(4-F-Ar)$_3$PS	40.88	
(C$_6$F$_5$)$_3$PS	-8.277	
(PhO)$_3$PSe	58.99	-291.70
(Et$_2$N)$_3$PSe	82.21	-258.70
(n-Pr)Ph$_2$PSe	34.15	-342.53
(n-Bu)$_3$PSe	37.12	-381.70
(n-Octyl)$_3$PSe	36.99	-390.30
Ph$_3$PSe	35.27	-266.20
(4-MeO-C$_6$H$_4$)$_3$PSe	31.72	-249.91
(2,4,6-MeO$_3$-C$_6$H$_2$)$_3$PSe	-17.48	-25.50
(4-F-C$_6$H$_4$)$_3$PSe	32.34	-250.43

Figure S4. 77Se NMR spectra for substituted triphenylphosphine selenides reported in this work. Other compounds reported previously.[1]

[1] Ruberu, T. P. A.; Albright, H. R.; Callis, B.; Ward, B.; Cisneros, J.; Fan, H.-J.; Vela, J. Molecular Control of the Nanoscale: Effect of Phosphine-Chalcogenide Reactivity on CdS-CdSe Nanocrystal Composition and Morphology. *ACS Nano* **2012**, *6*, 5348–5359.
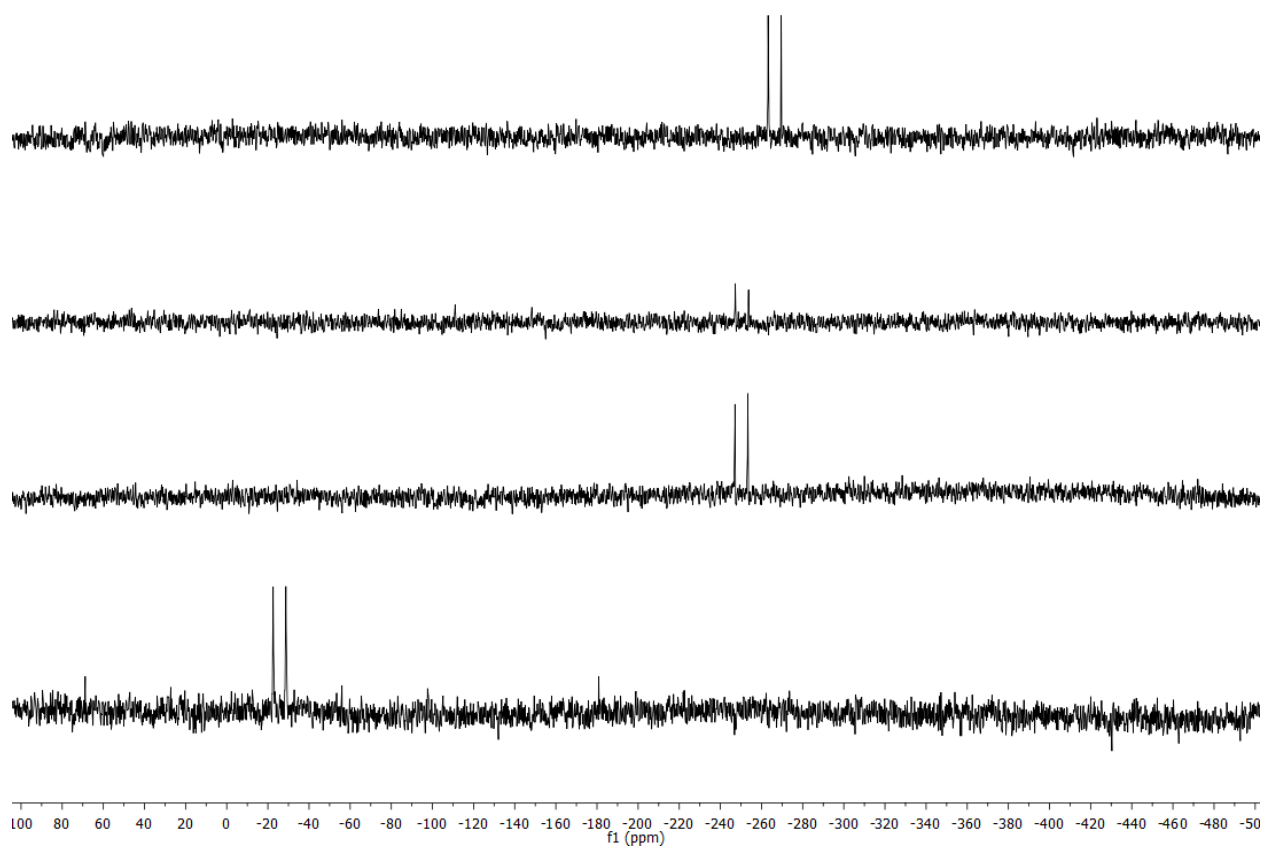
Table S6. Phosphine cone angles and computed ΔH of bond dissociation					
Compound	Tolman cone angle (°)[2]	Solid cone angle (°)[3]	DFT angle (Ni complex) (°)[4]	ΔH (P—S) (kcal/mol)	ΔH (P—Se) (kcal/mol)
Me$_3$P	118	124	125.8	75.13	62.59
Et$_3$P	132	143	142.6	76.73	64.62
(n-Bu)$_3$P	132	148	142.8	78.41	65.87
Ph$_3$P	145	145	177.6	71.87	59.62
(4-MeO-Ph)$_3$P	145	139	177.9	73.31	61.12
(4-F-Ph)$_3$P	145	129	178.0	75.13	62.59
Ph$_2$(n-Bu)P	140	140	156.5	74.01	62.07

[2] Tolman, C. A. Steric Effects of Phosphorus Ligands in Organometallic Chemistry and Homogeneous Catalysis. *Chem. Rev.* **1977**, *77*, 313–348.

[3] Brown, T. J.; Lee, K. J. Ligand Steric Properties. *Coord. Chem. Rev.* **1993**, *128*, 89–116.

[4] Bilbrey, J. A.; Kazez, A. H.; Locklin, J.; Allen, W. D. Exact Ligand Cone Angles. *J. Comput. Chem.* **2013**, *34*, 1189–1197.

Figure S5. Plot of Tolman cone angle against calculated BDE for select compounds
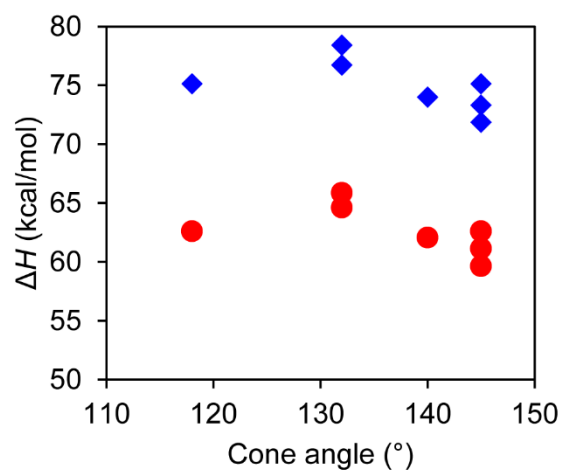

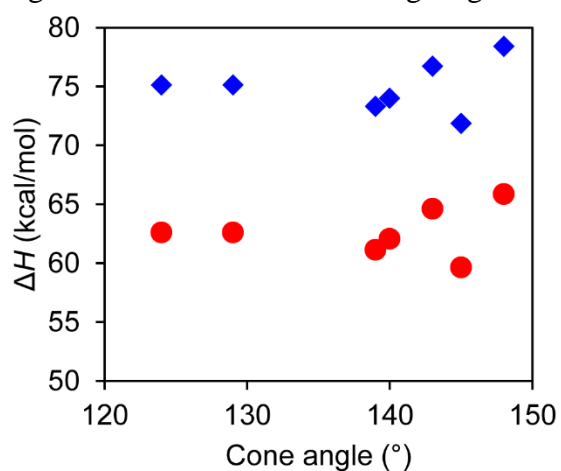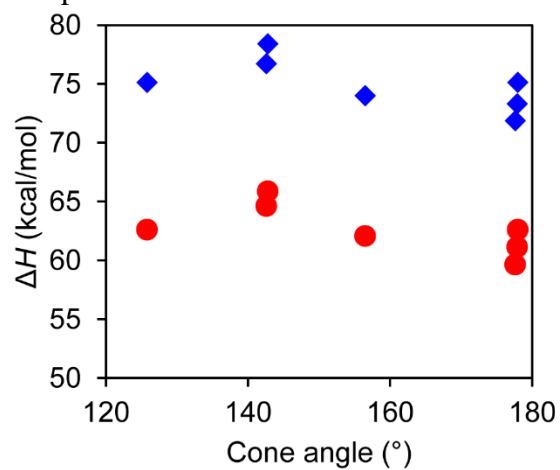Figure S6. Plot of solid cone angle against calculated BDE for select compounds

Figure S5. Plot of cone angle computed using DFT method against calculated BDE for select compounds

CHAPTER 5

CONCLUSIONS AND OUTLOOK

This thesis demonstrates some of the ways that molecular chemistry can provide new insight into nanocrystal synthesis. In chapter 2, the photolysis of aqueous $[Co(NH_3)_5Cl]^{2+}$ produced Co(O)OH nanocrystals of reliably small size. These spherical nanocrystals could be transformed into Co_3O_4 nanocrystals of similar size and shape by heating to 206 °C, roughly 40 °C lower than the same transformation in larger sized crystals. Chapter 3 discusses the correlation of computed BDE to the outcome of cadmium chalcogenide nanocrystal synthesis. Organodichalcogenide precursors containing weak E-E bonds and stronger C-E bonds afforded tetrapod shaped crystals, while precursors with strong E-E bonds and weaker C-E bonds yielded spherical morphology. The hypothesis in this case is that PhE monomers bind to certain nanocrystal facets, thus encouraging the growth of wurtzite arms only in certain crystallographic directions. Chapter 4 applies the same computational method to a series of organophosphine chalcogenide molecules to further probe their bond strengths and electronic structures. An interesting correlation between bond length and bond strength occurs in these molecules: Longer bonds are slightly stronger than shorter ones. This may be due to the increased difference in partial charge between the phosphorous and chalcogen atoms with increasing bond strength. These results may have ramifications on both selecting precursors for nanocrystal synthesis and chalcogen atom transfer reactions.

As a result of these successes, a variety of new questions surrounding the physical chemistry of nanocrystal synthesis arise. Perhaps the most conceptually straightforward is whether the computational methods disclosed in this thesis apply to other systems: Can they more generally understand and possibly predict the shapes or compositions of other II-VI

colloidal semiconductors, e.g. ZnS, ZnSe, CdTe, etc? Moreover, is the synthesis of III-V semiconductors such as InP or GaP understood in the same way? Recent work in the area of InP synthesis suggests a molecular influence in a proposed reaction mechanism.[1]

Validation of the computational results with experimental data from atom transfer reactions would further show the generality and the predictive power of computed BDEs. The energetics of chalcogen atom transfer from phosphine chalcogenides onto either free phosphines[2] or carbenes[3] would provide valuable data as well as demonstrate the use of new compounds in this reaction. This strategy may also help to identify any similarities between atom transfer reactions and the early stages of nanocrystal formation. Some mechanistic evidence suggests nucleophilic attack from a phosphine chalcogenide to the cadmium precursor to produce a Cd-Se bond.[4] However, problems such as the formation of phosphine oxide byproducts and the incorporation of water into precursors[5] make the proposal of a complete nanocrystal formation mechanism a formidable challenge.

One further challenge that a combined experimental/computational approach could handle is proposing a mechanism for the photochemical synthesis of nanocrystals. Chapter 2 of this thesis explored select mechanistic aspects, including the involvement of O_2, free radicals, and the probed the influence of using different wavelengths of light. Time-dependent DFT, employing proper functionals, could prove an invaluable tool for assigning electronic transitions that give rise to photochemical transformations. This approach simulates excitation energies and spectra for a variety of molecules,[6] although it is not always accurate when assessing excitations that have considerable charge transfer character.[7] Without a doubt, the field will continue to improve the accuracy of TD-DFT at this particular task.[8]

References

[1] Gary, D. C.; Glassy, B. A.; Cossairt, B. M. *Chem. Mater.* **2014**, *26*, 1734–1744.

[2] Capps, K. B.; Wixmerten, B.; Bauer, A.; Hoff, C. D. *Inorg. Chem.* **1998**, *37*, 2861–2864.

[3] McDonough, J. E.; Mendiratta, A.; Curley, J. J.; Fortman, G. C.; Fantasia, S.; Cummins, C. C.; Rybak-Akimova, E. V.; Nolan, S. P.; Hoff, C. D. *Inorg. Chem.* **2008**, *47*, 2133–2141.

[4] Sowers, K. L.; Swartz, B.; Krauss, T. D. *Chem. Mater.* **2013**, *25*, 1351–1362.

[5] Zherebetskyy, D.; Scheele, M.; Zhang, Y.; Bronstein, N.; Thompson, C.; Britt, D.; Salmeron, M.; Alivisatos, P.; Wang, L.-W. *Science* **2014**, *344*, 1380–1384.

[6] Laurent, A. D.; Jacquemin, D. *Int. J. Quant. Chem.* **2013**, *113*, 2019–2039.

[7] Dreuw, A.; Head-Gordon, M. *J. Am. Chem. Soc.* **2004**, *126*, 4007–4016.

[8] Autschbach, J. *Chem. Phys. Chem.* **2009**, *10*, 1757–1760.